STRUCTURE-PROPERTY RELATIONSHIPS OF MULTIFEORRIC MATERIALS –A NANO PERSPECTIVE

by

Feiming Bai

Dissertation submitted to the faculty of the
Virginia Polytechnic Institute and State University
in partial fulfillment of the requirement for the degree of
Doctor of Philosophy
in
Materials Science and Engineering

Dr. Dwight D. Viehland, Chair
Dr. Jie-Fang Li
Dr. William T. Reynolds, Jr.
Dr. David Clark
Dr. Robert Hendricks

April 2006
Blacksburg, Virginia

Keywords: multiferroic, functional materials, ferroelectricity, magnetostriciton, domain-engineering, piezoresponse force microscopy, magnetic force microcopy

STRUCTURE-PROPERTY RELATIONSHIPS OF MULTIFEORRIC MATERIALS –A NANO PERSPECTIVE

Feiming Bai

ABSTRACT

The integration of sensors, actuators, and control systems is an ongoing process in a wide range of applications covering automotive, medical, military, and consumer electronic markets. Four major families of ceramic and metallic actuators are under development: piezoelectrics, electrostrictors, magnetostrictors, and shape-memory alloys. All of these materials undergo at least two phase transformations with coupled thermodynamic order parameters. These transformations lead to complex domain wall behaviors, which are driven by electric fields (ferroelectrics), magnetic fields (ferromagnetics), or mechanical stress (ferroelastics) as they transform from nonferroic to ferroic states, contributing to the sensing and actuating capabilities.

This research focuses on two multiferroic crystals, $Pb(Mg_{1/3}Nb_{2/3})O_3$-$PbTiO_3$ and Fe-Ga, which are characterized by the co-existence and coupling of ferroelectric polarization and ferroelastic strain, or ferro-magnetization and ferroelastic strain. These materials break the conventional boundary between piezoelectric and electrostrictors, or magnetostrictors and shape-memory alloys. Upon applying field or in a poled condition, they yield not only a large strain but also a large strain over field ratio, which is desired and much benefits for advanced actuator and sensor applications. In this thesis, particular attention has been given to understand the structure-property relationships of these two types of materials from atomic to the nano/macro scale. X-ray and neutron diffraction were used to obtain the lattice structure and phase transformation characteristics. Piezoresponse and magnetic force microscopy were performed to establish the dependence of domain configurations on composition, thermal history and applied fields.

It has been found that polar nano regions (PNRs) make significant contributions to the enhanced electromechanical properties of PMN-x%PT crystals via assisting intermediate phase transformation. With increasing PT concentration, an evolution of PNR→PND (polar nano domains)→ micron-domains→macro-domains was found. In addition, a domain hierarchy was observed for the compositions near a morphotropic phase boundary (MPB) on various length scales ranging from nanometer to millimeter. The existence of a domain hierarchy down to the nm scale fulfills the requirement of low domain wall energy, which is necessary for polarization rotation. Thus, upon applying an E-field along <001> direction(s) in a composition near the MPB, low symmetry phase transitions (monoclinic or orthorhombic) can easily be induced. For PMN-30%PT, a complete *E-T* (electric field vs temperature) diagram has been established.

As for Fe-x at.% Ga alloys, short-range Ga-pairs serve as both magnetic and magnetoelastic defects, coupling magnetic domains with bulk elastic strain, and contributing to enhanced magnetostriction. Such short-range ordering was evidenced by a clear 2θ peak broadening on neutron scattering profiles near A2-DO_3 phase boundary. In addition, a strong degree of preferred [100] orientation was found in the magnetic domains of Fe-12 at.%Ga and Fe-20 at.%Ga alloys with the A2 or A_2+DO_3 structures, which clearly indicates a deviation from cubic symmetry; however, no domain alignment was found in Fe-25 at.%Ga with the DO_3 structure. Furthermore, an increasing degree of domain fluctuations was found during magnetization rotation, which may be related to short-range Ga-pairs cluster with a large local anisotropy constant, due to a lower-symmetry structure.

To my parents and wife,

ACKNOWLEDGMENTS

I would like to express my sincere gratitude to my advisors, Prof. Dwight Viehland and Prof. Jiefang Li, for their faith, guidance and support throughout the course of my Ph.D research.

I have tremendous respect to Prof. Dwight Viehland for his knowledge, wisdom and passion for research. I benefited from his guidance in every aspect and step during my Ph.D study, including his class of "Advanced Functional Materials", the discussions we held and all those sparking suggestions he made regarding my research, his patience when correcting my papers, proposals and thesis, and his assistance on my preparation for seminar and conference talks. I deeply appreciate all these invaluable help. In addition, he has been always excited about every small step forward I have made. He always makes me and other group members feel that we could do anything. This is the exact feeling I have been dreaming to be a materials scientist.

Also, Prof. Jiefang has given me great helps in almost all equipment and facilities set-up. She generously shared all her knowledge and experience in experimental techniques. Without her help, my research would not be so successful.

I would like to thank Prof. William Reynolds for all the valuable discussion we held on magnetostrictive materials and shape memory alloys as related to this project.

I would like to thank Prof. David Clark and Prof. Robert Hendricks for serving in my committee and taking time out of their busy schedules to evaluate my work.

I would like to give my special acknowledgements to Dr. Peter Gehring at Neutron Center of National Institute of Standards and Technologies, Dr. Guangyong Xu and Dr.

Gen Shirane at Brookhaven National Laboratory, who greatly helped me to develop expertise in X-ray diffraction and neutron scattering and revised my first important science publication.

I would like to thank Dr. Tom Lograsso at Ames Laboratory for supplying Fe-Ga crystals and giving valuable suggestions on the interpretation of XRD and MFM results.

I would like to thank Hu Cao and Naigang Wang. We have had very close cooperation on the structure studies of PMN-PT and Fe-Ga crystals.

I would like to thank Dr. Shuxiang Dong for all the discussion we held in the view of real application of current project.

I would like to thank Dr. Carlos Suchicital and David Berry for all the technical support.

I thank John Bai and all other group members, Yan Li, Junyi Zai and Zengping Xing. It will be always a good memory to work with these guys.

The most important acknowledgment was saved for last. I would like to express my gratitude to my parents and my wife, Carol Li. They have been constantly providing faith, encourage and enjoyment during my Ph.D study.

TABLE OF CONTENTS

ACRONYMS

AC	Alternative Current
AFM	Atomic Force Microscopy
DC	Direct Current
FFT	Fast Fourier Transformation
FC	Field cooling
M	Monoclinic
MFM	Magnetic force microscopy
MPB	Morphotropic phase boundary
MT	Martensitic transition
O	Orthorhombic
R	Rhombohedral
PA	Post Annealing
PFM	Piezo-response force microscopy
SFM	Scanning Force Microscopy
SPM	Scanning Probe Microscopy
T	Tetragonal
XRD	X-ray Diffraction
ZFC	Zero Field Cooling

LIST OF TABLES

LIST OF FIGURES

I. INTRODUCTION

1.1 Ferroics and multiferroics

A 'primary ferroics' is a general term that includes ferromagnetic, ferroelectric, and ferroelastic materials.[1-2] Generally, ferroic crystals have three characteristics: (i) a spontaneous order parameter (magnetization, electric polarization or elastic deformation); (ii) the occurrence of multiple domain states over whose length scale the order parameter is essentially uniform, and whose boundaries move under an external field; and (iii) hysteresis caused by field-induced domain motion during order parameter reversal. A hyteresis loop of three **primary ferroics** and their important parameters are illustrated in Fig1-1. The properties of ferroic materials are often superior to conventional materials because of their spontaneous order parameters and large nonlinear coefficients. Due to inherent structural nonlinearity, such ferroic properties render sensors more sensitivity and actuators more powerful.

"**Multiferroics**" are characterized by the co-existence of more than one spontaneous order parameter.[3] Accordingly, these materials have at least (i) two types of hysteresis loops; (ii) two types of domain structures and (iii) exchange between primary order parameters. The relation between multiferroic and primary ferroics are shown in Figure 2, where **A** represents the coexistence of magnetization and electric polarization; **B** the coexistence of electric polarization and ferroelastic strain; **C** the coexistence of magnetization and ferroelastic strain; and **D** the coexistence of all these spontaneous order parameters. For primary ferric materials, an order parameter only appears below a certain critical symmetry transformation temperature and domain states can only be

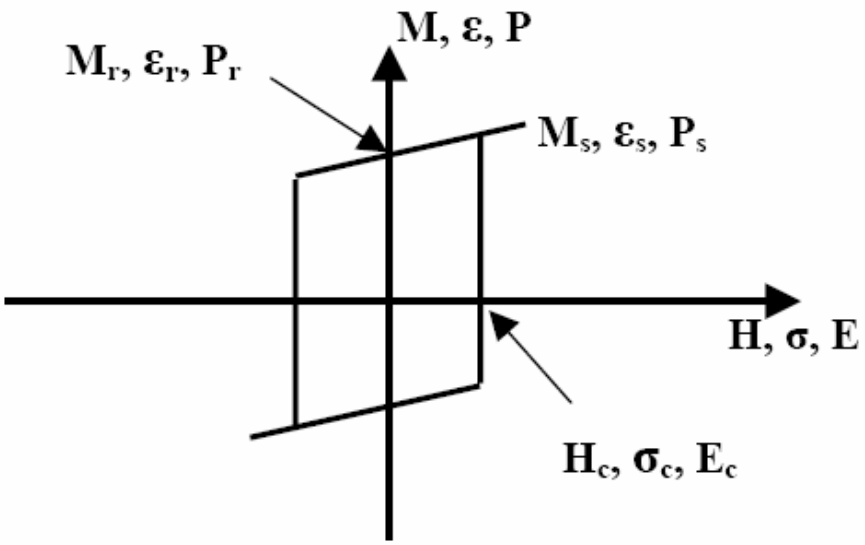

Fig.1-1. Schematic illustrate of a hysteresis loop showing the coercive field, remnant and saturation strain, polarization and magnetization.

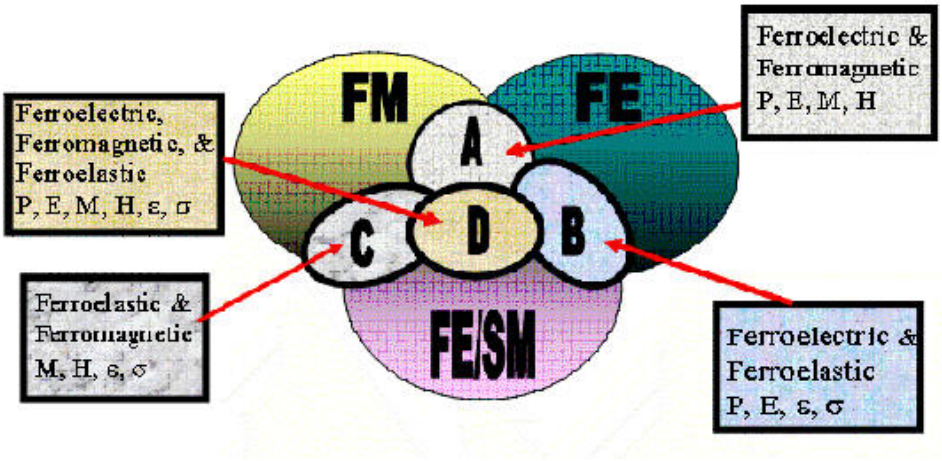

Fig.1-2. Schematic illustration of functional ferroic and multi-ferroic materials.

switched by a field that is conjoint to the order parameter. In the contrast, the Curie temperature of a multiferroic material is dependent on multiple ordering fields (magnetic field, electric field or stress). Accordingly, their domain states can be switched by more than one field type. For example, magnetoelectric (ME) materials are characterized by the switching of an electric polarization upon applying a magnetic or electric field, and vice verse.[4] Clearly, multiferroic materials can offer the potential for revolutionary device designs, as they are at the heart of multifunctionality.

1.2 Ferroelectric and ferroelastic biferroics

To possess a spontaneous polarization, a crystal must lack a center of symmetry. In addition, the spontaneous polarization must be switchable by an applied electric field, i.e. at least two equivalent crystallography orientations for different polarization vectors.[5] Amongst the 32 crystal point groups, twenty-one crystal classes do not have a center of symmetry and thus (i) have one or more polar orientations, and (ii) possess odd-rank tensor properties. The only exception is the group 432, which lacks a center of symmetry, but has other symmetry operations that destroy polarity. All non-centrosymmetric point groups exhibit a piezoelectric effect that is defined by a change in electric polarity under applied stress, and vice versa. Out of the twenty piezoelectric classes, ten possess a unique polar axis, the spontaneous polarization of which depends on temperature. This is called the pyroelectric effect. Ferroelectric crystals belong to the pyroelectric family, which in addition has a spontaneous polarization that can be reversed by external electric field, i.e. more than one equivalent direction for P_s.[6] It is clear that a ferroelectric material must be simultaneously piezo- and pyro-electrics.

1.2.1 Origin of ferroelectricity and piezoelectricity

The most extensively studied and widely used ferroelectric materials have the perovskite structure. A perfect perovskite structure has a general formula of ABO_3, where A represents a divalent or trivalent cation and B is typically a tetravalent or trivalent cation. The A ions occupy the corners of the cube, while the B ions sit on the body center positions inside an oxygen octahedron, which are at the face center positions. The B-site ions can move relative freely inside the oxygen octahedron with relative small restoring force.

Barium titanate ($BaTiO_3$) is the most well-known ferroelectric material and can serve as an excellent example to illustrate the ferroelectricity and piezoelectricity in perovskite structures. The tetravalent Ti^{4+} ions occupy the B site of the $BaTiO_3$ perovskite structure and are surrounded by O^{2-} in the octahedral configuration. At high temperature ($T>T_c$), although the open octahedral structure allows the Ti^{4+} ions to move from one position to another, there is no spontaneous alignment of the dipoles due to random thermal vibration. In this cubic symmetric configuration, the material is paraelectric, (i.e. no net dipole moment). At a temperature below T_c, the structure changes from cubic to tetragonal (T) with the Ti^{4+} ions in an off-center position giving rise to a net dipole moment along the c-axis (spontaneous polarization direction), as illustrated in Fig.1-3. Accordingly, polarization formation rises a transformation to a tetragonal lattice structure. At lower temperatures, a sequence of phase transformations was reported in $BaTiO_3$: in T→R (rhombohedral) with a <111> spontaneous polarization, and a subsequent R→O (orthorhombic) with a <110> spontaneous polarization.[7] The spontaneous polarization

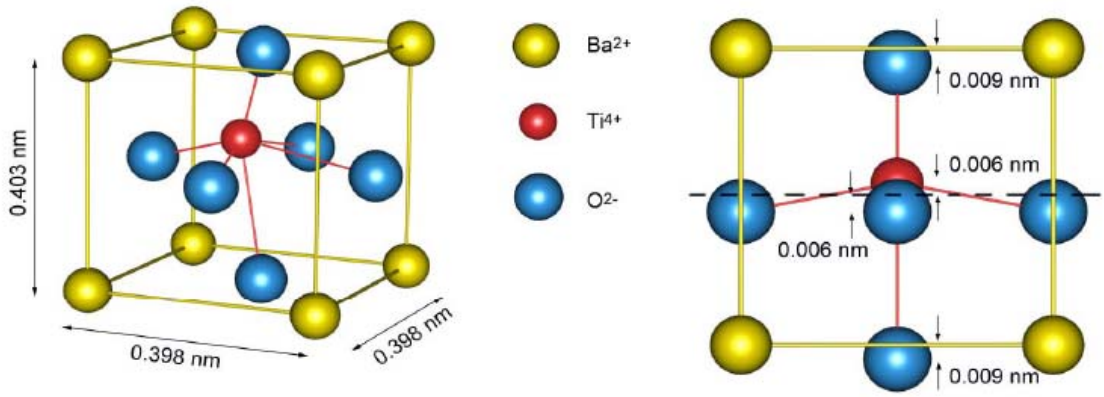

Fig.1-3. A $BaTiO_3$ unit cell in an isometric projection and viewed looking along one face, which shows the displacement of Ti^{4+} and O^{2-} ions from the center of the face.

direction is coupled to lattice structure via electrostriction, and the differential of the electrostrictive strain over applied electric field (E-field) gives rise to piezoelectricity.

1.2.2 Ferroelectric phase transformations

As stated in last section, ferroelectric phase transformations involve a change in symmetry of a crystal. Such structural phase transitions can be classified as **continuous** or **discontinuous**. If the spontaneous polarization varies continuously with temperature and tends towards zero at the transition temperature, as shown in Fig.1.4(a), it is said to be a **second order transition**. However, if the spontaneous polarization abruptly changes at the transition temperature, as shown in Fig.1.4(b), it is said to be a **first order transition**. In the case of continuous phase (2^{nd} order) transformation, the symmetry group of the ferroelectric phase is a *subgroup* of that of the paraelectric state. However, for a 1^{st} order transformation, there is no such simple relation between the symmetries of the two phases.

A popular and useful way to identify a ferroelectric phase transformation is the temperature dependence of the dielectric constant. Fig.1-5 shows the dielectric constant (κ) of $BaTiO_3$ single crystals as a function of temperature.[7] In this figure, a phase transformation sequence of C→T→O→R can be seen with decreasing temperature. The order of each transition can be determined by Curie-Weiss plots ($1/\kappa$ vs T). If $1/\kappa$ approaches zero at T_c, then the transition is 1^{st} order; whereas if $1/\kappa$ approaches a finite value at T_c, then it is a 2^{nd} order transition.

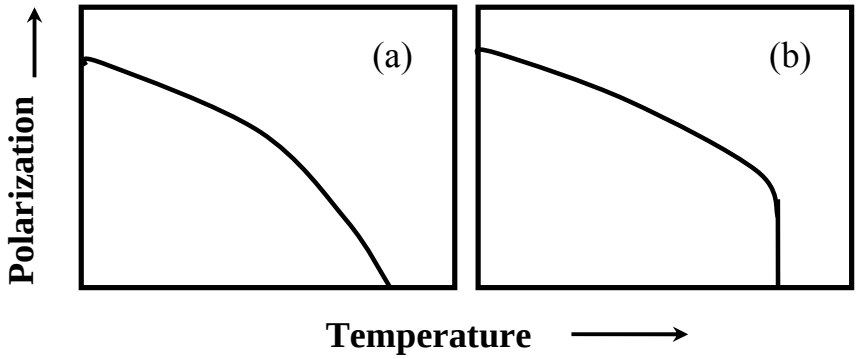

Fig.1-4. Polarization vs. temperature plot for: (a). 2nd order phase transition; (b). 1st order phase transition.

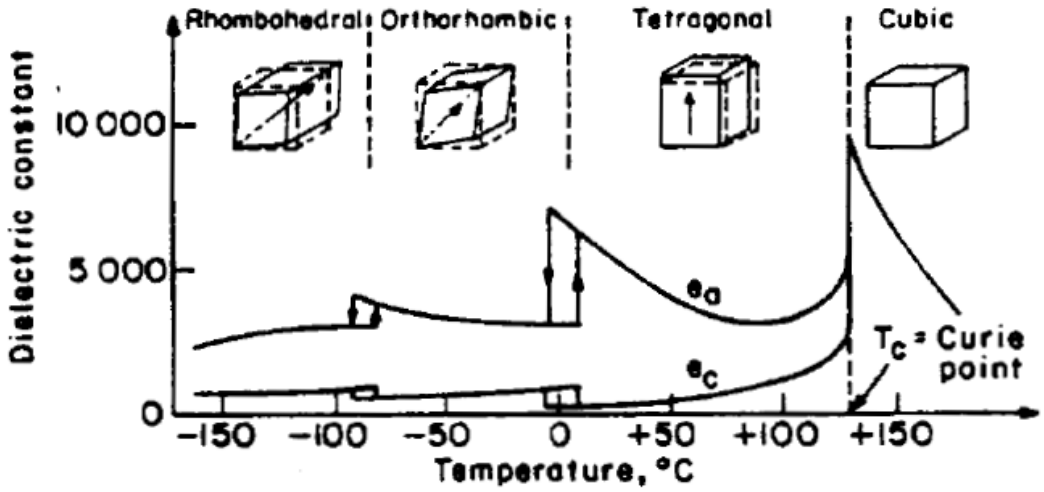

Fig.1-5. Dielectric permittivity of $BaTiO_3$ single crystals as a function of temperature under weak E-field. All phase transitions from high to low temperature are the first order. [Ref.7]

1.2.3 Prior investigations of relaxor ferroelectrics

Relaxor behavior

Relaxor behavior was first found in bismuth and strontium titanate (BST).[8] The complex permittivity is strongly frequency dependent, where the temperature of the dielectric maximum shifts to higher temperature with increasing measurement frequency. Smolenski et al. have reported similar relaxation behavior in the zero-field-cooled (ZFC) state of $Pb(Mg_{1/3}Nb_{2/3})O_3$ (PMN).[9] Bokov found slim polarization vs. electric field (P-E) loop near the dielectric maximum temperature; whereas fat hysteretic P-E response at lower temperature.[10] He also identified the presence of "normal" domains in the field-cooled (FC) state. Consequently, these materials became known as relaxor ferroelectrics to contrast their dual nature which had previously been believed to be mutually exclusive, i.e. having both the characteristics of a classic relaxational dielectric in the ZFC state and a normal ferroelectric in the FC state. In crystalline solutions, such as PMN-PT, the relative phase stability of normal and relaxor ferroelectric states can be tailored by changing the PT concentration, as will be discussed latter.

Cross has summarized the basic features of PMN relaxors, which are applicable to other relaxors,[11] including: (1) a broadening of the complex dielectric constant where the peak value of dielectric constant (ε'_{max}) decreases with increasing measurement frequency; (ii) a lack of macro symmetry changes that can be detected by X-ray or neutron diffraction near or below the dielectric anomaly; and (iii) slim hysteresis loop instead of normal square one near T_{max}. These basic relaxor characteristics are illustrated in Fig.1-6, where the temperature dependence of dielectric constant and polarization of PMN-10%PT is given.[12-13]

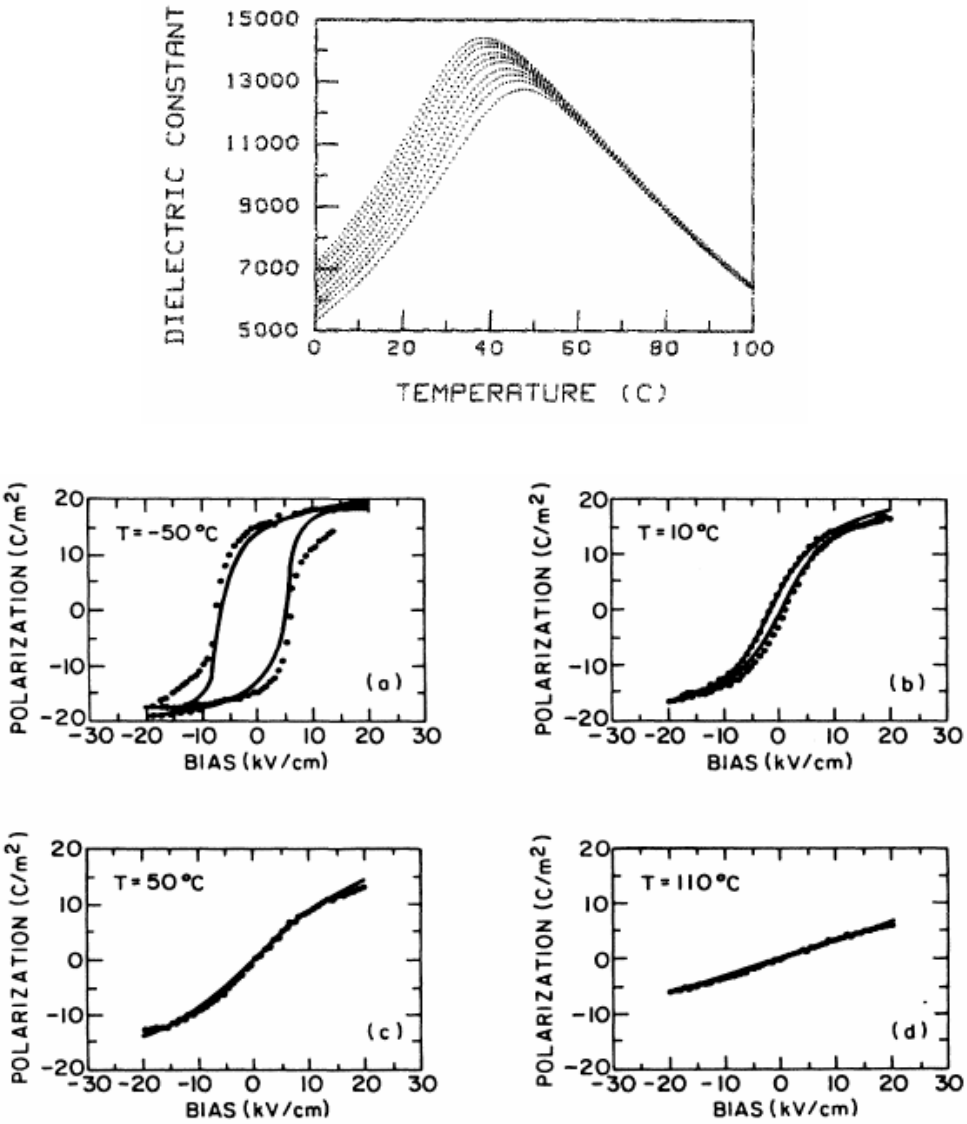

Fig.1-6. (a) Dielectric constant of PMN-10%PT as a function of temperature at measurement frequencies of 0.1, 0.2, 0.4, 1, 2, 4, 10, 20, 40 and 100 kHz. The highest dielectric response is the 0.1 kHz curve, the lowest is the 100 KHz curve, and the other curves between are in order of increasing frequency. (b)-(d): Polarization curves at various temperatures. The solid points are the experimental data measured at -50, 10, 50 and 110^{o}C, respectively. [Ref.12-13]

Presence of polar nano-regions (PNR)

Burns and Docal observed that the optical index of refraction for the $(Pb_{1-3x/2}La_x)(Zr_yTi_{1-y})O_3$ (PLZT) relaxor deviated from a linear temperature dependence until temperatures significantly higher than T_{max}.[14] These results were interpreted in terms of the occurrence of local polarizations at an onset temperature (denoted as T_{Burns} or T_d) far above T_{max}. For PMN relaxors, T_d was determined to be ~620 K. The nonlinearity in the index of refraction was attributed to a coupling of the local polarization to the optical constants via the quadratic electro-optic coefficients. The degree of deviation from linearity was found to significantly increase with decreasing temperature, indicating an increase in the volume fraction of the local polar moments.

Soft mode and nature of PNR

The concept of a "soft mode" is relevant to the fundamental understanding of the structural aspects of normal ferroelectric transformations. It is known in displacive transformations that the ferroelectric phase is realized by minute thermal displacements of atoms in the paraelectric state. It was the idea of Cochran and Anderson that when the frequency of transverse optic (TO) phonon approaches zero, a structural transformation to a ferroelectric phase occurs.[15-16] In ferroelectric phases, the soft modes are infrared active and of long wavelength. Such mode softening develops due to the cancellation of short- and long-range forces. By use of lattice dynamics, the ferroelectric transformation can be associated with the condensation of a soft mode in the Brillourin-zone center (i.e. q=0, where q is the wave vector). The existence of a soft transverse optic phonon mode has been documented in numerous perovskite including $PbTiO_3$, $BaTiO_3$, $SrTiO_3$ and

$KTaO_3$. In the case of $PbTiO_3$, the frequency of the lowest-lying TO mode drops when cooled from high temperature and condenses at a (first-order) transition temperature Tc=763 K.[17]

However, in the case of PMN and PZN relaxors, a soft transverse optic mode has only been seen at a temperature above T_d, which is hundreds of degrees higher than the ferroelectric transition temperature. In the temperature range between T_c and T_d, lattice dynamical studies by Naberezhnov et al. have shown the transverse optic and transverse acoustic (TA) mode dispersion.[18] In addition, neutron inelastic scattering by Gehring et al. has revealed an unusual feature where the TO branch appears to drop into the TA branch around a q of 0.15 reciprocal lattice unit (1 rlu=1.545 $Å^{-1}$), as shown in Fig.1-7.[19] This feature was latter designated as the "waterfall" and was believed due to an unusual damping mechanism that effectively freezes out the long-wavelength TO modes. The polar nano regions are the most plausible cause of this damping. If one assumes that the waterfall peak position in q gives a measure of the size of the PNR according to $2\pi/q$, one obtains a value of 30 Å, or about 7-8 unit cells, consistent with the conjecture of Burns and Dacol.[14]

Finally, polar nano-regions in PMN have been directly imaged by transmission electronic microscopy (TEM), as shown in Fig.1-8. They appeared to be fine-scale contrast in the bright field images.[20] Accordingly, relaxors like PMN and PZN are not homogeneous ordered crystals but rather a 0-3 *nanocomposite* of ferroelectric "displaced polar nanoregions" embedded in cubic matrix.

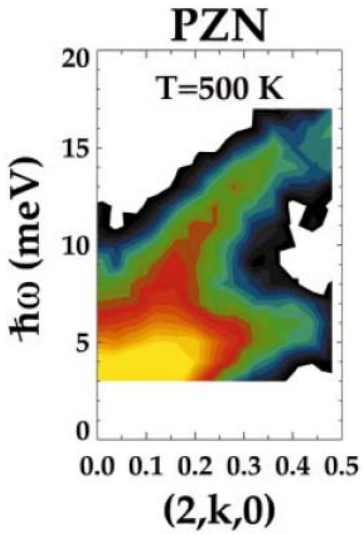

Fig.1-7. Logarithmic color contour plot of the neutron inelastic scattering intensity measured in PZN at 500 K in the (200) Brillouin zone. Yellow represents the highest intensity. The vertical red region around k = 0.14 r.l.u. corresponds to the waterfall anomaly in which the TO phonon branch appears to plummet into the TA branch. [Ref. 19]

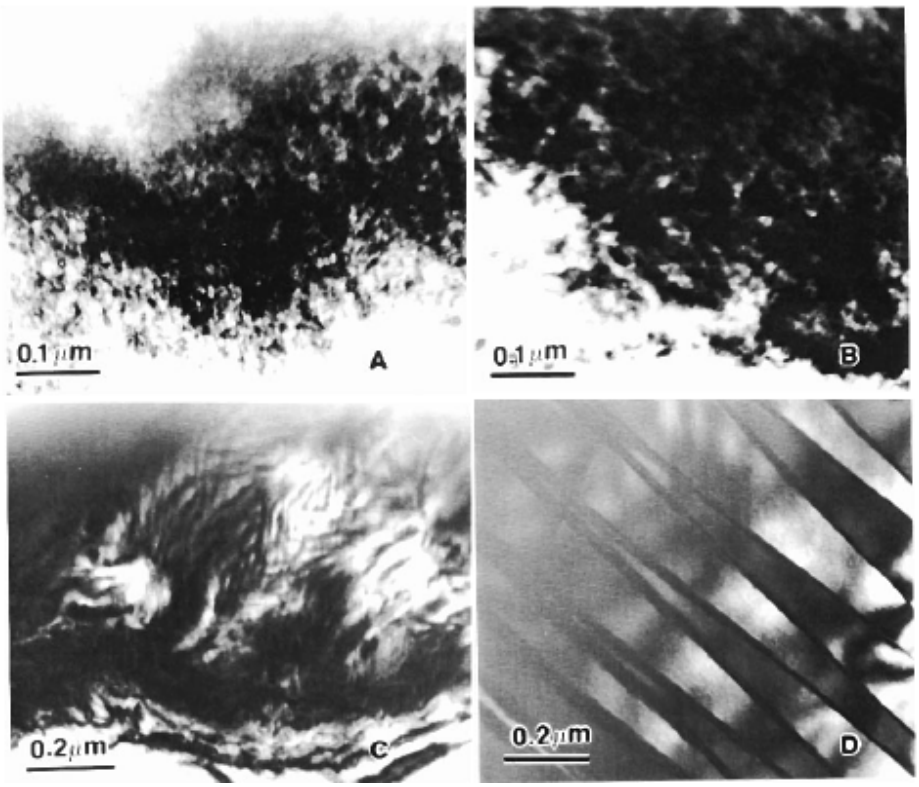

Fig.1-8. Bright-field images for various PMN-PT compositions: (a) 90/10, (b) 80/20, (c) 65/35, and (d) 40/60. For PMN-PT 90/10, polar nanodomains are clearly evident. The average size of these polar nanodomains was 50 Å. [Ref.20]

Relaxor-normal ferroelectric solid solution

Since the discovery of PLZT and PMN, the study of relaxor behavior has intensified due to strong nonlinearities in the dielectric, elastic and electromechanical properties that are suitable for applications from multilayer ceramic capacitors to actuators and electro-optical devices. However, most relaxors have rhombohedral structure and relatively low E-field induced strain along spontaneous polarization direction. Since the normal tetragonal ferroelectric phase yields a large strain due to E-field induced a- to c- domain rotation, a natural idea of tailoring material properties is to make relaxor-normal ferroelectric solid solution. The phase diagram of PZT ceramics is showed in Fig.1-9(a).[21] Compositions near the boundary region between tetragonal and rhombohedral phases exhibit anomalously high dielectric and piezoelectric properties (Fig.1-9(b)).[22-23] This composition region was later named as morphotropic phase boundary (MPB), where R and T phases were believed to coexist. Alternate MPB systems have been extensively searched in relaxor-$PbTiO_3$ or relaxor-$BaTiO_3$, in which relaxor materials are complex perovskites with the general formula $Pb(B_IB_{II})O_3$ (B_I=Mg^{2+}, Zn^{2+}, Ni^{2+}, Sc^{3+}…, B_{II}=Nb^{5+}, Ta^{5+}, W^{6+}…). All of these solid solutions are characterized by much improved properties compared to their components. It was believed that the high dielectric and piezoelectric properties resulted from the coupling between two equivalent energy states (T and R phases), allowing optimum domain reorientation during the poling process.

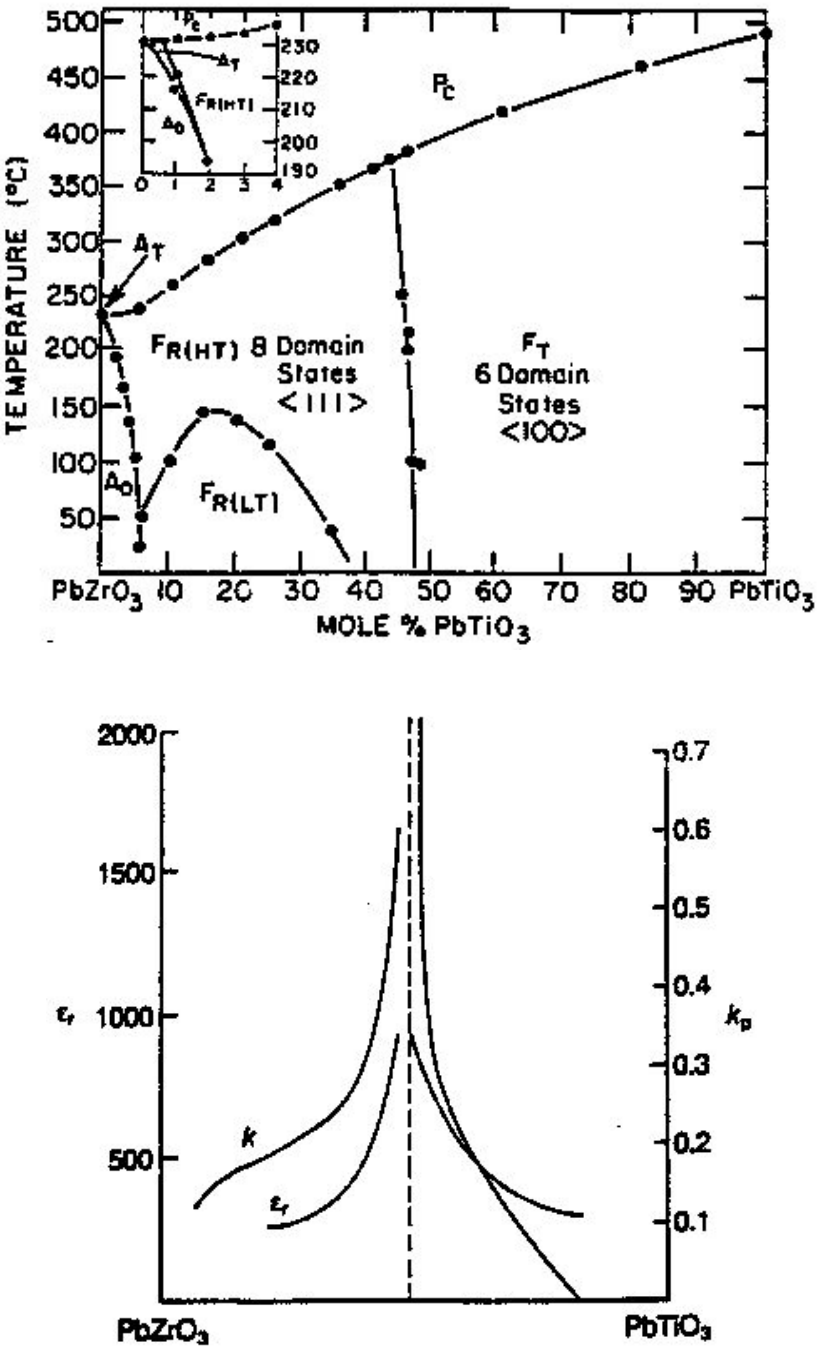

Fig.1-9. (a) The PZT phase diagram; and (b) the corresponding dielectric constant and electromechanical coupling factor k_p dependence on composition. [Ref.21-23]

1.2.4 Domain engineering in relaxor-normal ferroelectric solutions

The most important advancement in ferroelectric materials during the last decade was the discovery of $Pb(Mg_{1/3}Nb_{2/3})O_3$-x%$PbTiO_3$ (PMN-x%PT) and $Pb(Zn_{1/3}Nb_{2/3})O_3$-x%$PbTiO_3$ (PZN-x%PT) single crystals.[24] When poled along a non-spontaneous <001> direction, an ultra-high piezoelectric coefficient d_{33} of 2500 pC/N and electromechanical coupling coefficient k_{33} of 94% have been reported for compositions near the morphotropic phase boundary (MPB), as shown in Fig.1-10.[24-25] A domain-engineered state, due to an electric field induced rhomobohedral-to-tetragonal phase transition, was originally proposed by Park and Shrout to explain the ultrahigh electromechanical properties. Strain as high as 1.7% has been realized as a result of this induced transition, as shown in Fig.1-11. However, how the R phase transforms into T phase remained unclear.

Domain engineering—ferroelectric polarization interpretation

Investigation of the origin of the ultra-high electromechanical properties has been ongoing since then. Noheda first discovered a monoclinic phase, sandwiched between R and T phases near a MPB in $Pb(ZrTi)O_3$ (PZT) ceramics at low temperature.[26] This completely changed the well-accepted picture of the MPB, since this new phase acts as a structural bridge between the R and T phases. Subsequently, first principle calculations by Fu and Cohen suggested a polarization rotation during an E-field induced R to T phase transformation, which takes a path with small energy change, and thus allows the existence of intermediate low symmetry phase(s).[27] They predicted that the energy changes are probably very small in PMN-PT, so a very small field can cause the

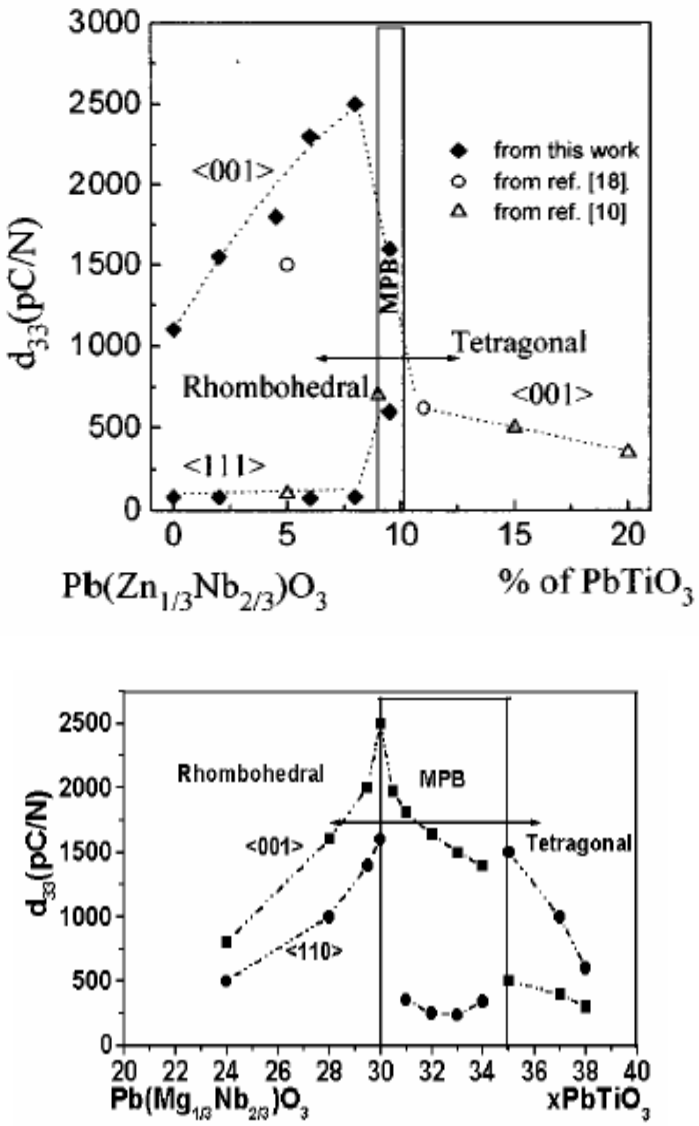

Fig.1-10. The piezoelectric coefficient d_{33} dependence on PT concentration, (a) PMN-x%PT and (b) PZN-x%PT. [Ref.24-25]

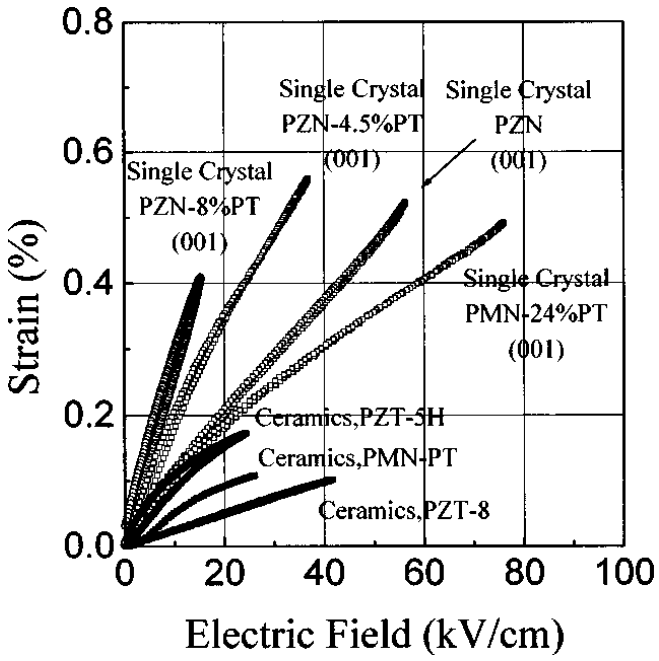

Fig.1-11. Strain vs. electric field of several piezoelectric ceramics and single crystals. [Ref.24]

polarization rotation. And using a Landau-Devonshire approach, Vanderbilt and Cohen then expanded the free energy to the eighth power in the polar order parameter, providing the thermodynamic basis for a monoclinic phase.[28-29] According to this theory, while the direction of the polarization vector in a conventional ferroelectric tetragonal (or rhombohedral) phase is fixed to the [001] (or [111]) direction, the monoclinic symmetry allows the polarization vector to continuously rotate in a plane and contributes to enhanced polarization and strain. They further suggested three monoclinic phases: M_A, M_B and M_C, according to their symmetry relations with the parent phase. Bellaiche et al. predicted that applying an E-field along [111] direction to the T phase results to a phase transformation sequence of $T \rightarrow M_A \rightarrow R$, while application of an E-field along [001] orientation to an R phase induces a phase transformation sequence of $R \rightarrow M_A \rightarrow Tri \rightarrow M_C \rightarrow T$.[30] Up to now, diffraction experiments of PZN-x%PT and PMN-x%PT have provided direct evidence of these monoclinic phases in both zero-field-cooled and field cooled samples for E//[001] direction.[31-37] Fig.1-12 shows the recent updated phase diagrams of the PMN-PT crystalline solution in the zero-field-cooled condition based on these experiment results, where the MPB composition has an M_C phase symmetry.[36] *However, the transformational sequence of these PMN-x%PT crystals under E-field has not yet been experimentally established, which is very important for the application such as actuators and transducers.*

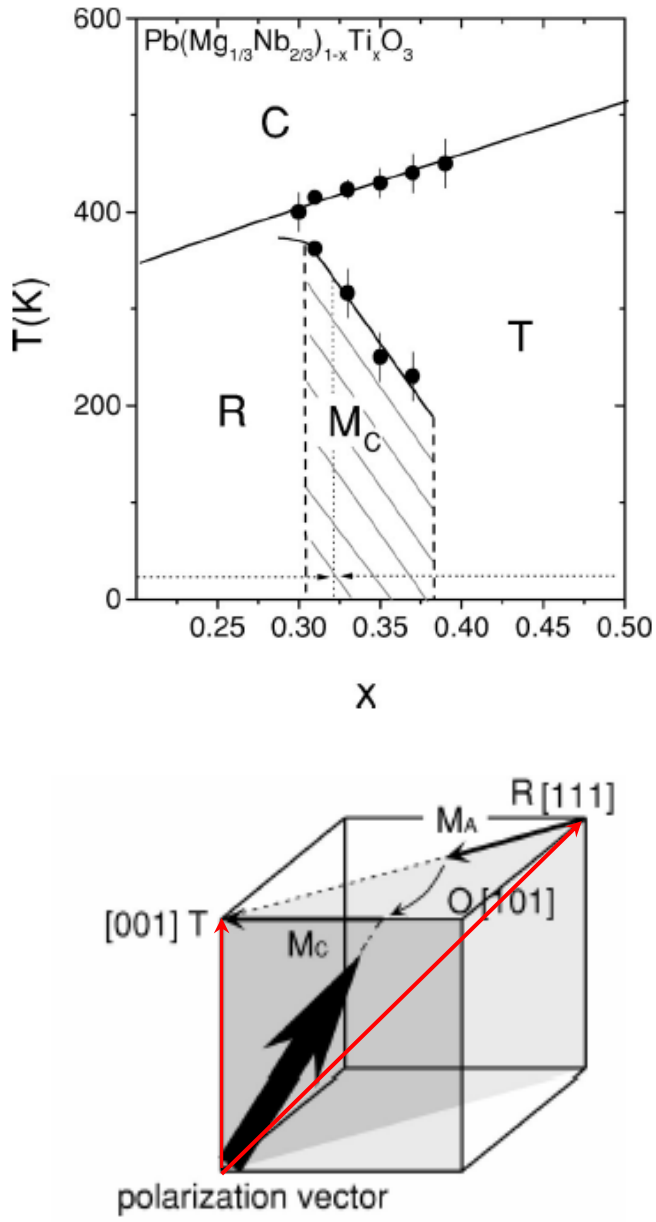

Fig.1-12. (a) Phase diagram of the PMN-PT solid solution system. The data points come from published results by Noheda *et al.*[36] (b) Polarization rotation path in the perovskite M_A and M_C unit cell. *C*, *R*, *T*, *O* and *M* refer to cubic, rhombohedral, tetragonal, orthorhombic and monoclinic regions, respectively.[Ref. 36]

Domain engineering—ferroelastic domain interpretation

Martensitic transformations (MT) are a common phenomenon, driven by thermodynamics in ferroelastic alloys. At a transition temperature (T_M), a sudden change of lattice parameters occurs between high temperature and low temperature phases, which correspond to austensite and martensite, respectively. Thus, the MT is a first-order diplacive transformation. The lack of smoothness during the transformation yields such characteristics as hysteresis loop, twinning, and a release of latent heat. Twinning is one of the most important structural features of martensite. Ferroelastic twin boundaries relax elastic energy by adjusting to particular crystallographic orientations in order to achieve stress accommodation and thus energy minimization. These twin conditions are documented in the Wechsler-Lieberman-Read theory of martensitic transformation.[38]

However, the presence of mesoscopic tweed-like striations observed by TEM at temperature significantly above "T_m" in shape memory alloys (such as FePd and NiAl) later challenged the conventional martensitic transformation theory, mentioned above.[39-40] Kartha et al. developed a dimensional "glassy" mesophase model for metastable tweed structure observed in premartensitic transformations.[41] They modeled precursor phenomena using nonlinear nonlocal elastic free energy coupled to quenched local composition inhomogeneities. Khachaturyan et al. proposed a more sophisticated thermodynamic theory which allows for adaptive symmetries.[42]

An adaptive phase was believed to be a metastable alternative to normal nucleation and growth. Rather, in this case, the transformation path is characterized by a sequence of mesoscale coherent structures formed by atomically thin martensitice plates consisting of quasiperiodic alternation lamellae with period λ, as show in Fig.1-13. The condition for

the minimization of the twin thickness is controlled by a balance of elastic and surface energy terms, as given below:

$$\lambda \sim (\gamma_{tw} D / \mu \varepsilon_{<001>}^2)^{1/2}$$

where γ_{tw} is the twin surface energy, μ is the shear modulus, and $\varepsilon_{<001>}$ is the elastic strain along the <001>. Twin thickness minimization to atomic levels will occur under simultaneous conditions of a low γ_{tw}, a soft elastic shear modulus and high transformation strain in the C→T transformation. The symmetry requirement upon the adaptive phase is that it must be a subgroup of the parent phase. Consequently, an adaptive phase is related to its parent phase through an invariant-plane strain (IPS), which is also parallel to the twinning plane of the produce phase. In a cubic-to-tetragonal MT, an adaptive phase has an averaged pseudocubic orthorhombic symmetry.[42] Accordingly, the T_m locates between C and O phase instead of C and T phases.

Recently, this adaptive phase theory has been applied to the relaxor-normal ferroelectric phase transformation near the MPB, assuming that (i) an R→T ferroelastic phase transformation with large strain during poling that requires domain rearrangement; (ii) R phase can be deemed as pseudocubic phase; and (iii) the domain wall energy is very small in the vicinity of the MPB. [43] It was shown that this theory can successfully explain the E-field induced intermediate orthorhombic and monoclinic ferroelectric phases of PZN-PT near the MPB.[43] Later, Jin et al. proposed a model of an adaptive ferroelectric phase, conjecturing that nanoscale stress-accommodated *tetragonal* microdomains near the MPB results in form an *averaged monoclinic* M_C phase.[44] The intrinsic relationships of lattice parameters between the C, T and M_C were shown to be experimentally fulfilled in PMN-x%PT for 31<x<37 and PZN-8%PT.

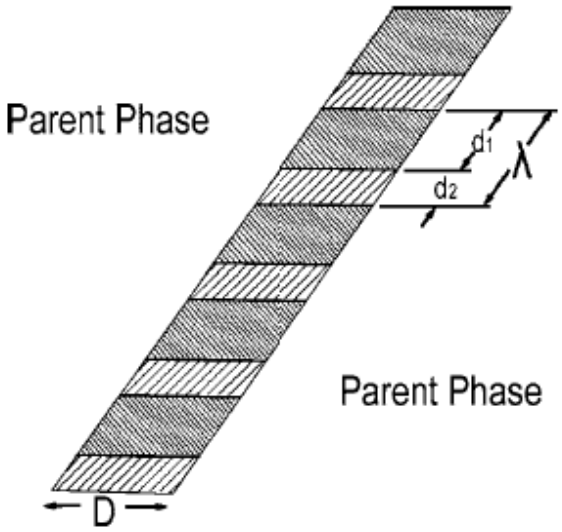

Fig.1-13. Schematic representation of the martensitic phase plate composed of twin-related lamellae of two orientation variants of the martensitic phase. The appropriate *d*1-to-*d*2 ratio completely accommodates the martensite-toparent phase macroscopic transformation strain mismatch along the habit plane. [Ref. 42].

Domain engineering and PNR

The current available experiment results are not sufficient to provide a conclusive answer to whether the intermediate phases are actually independent of their parent phases or not, i.e. true phase transformation in atomic scale. However, it is now widely accepted that the domain engineering in the relaxo-normal ferroelectric crystals can be interpreted in terms of polarization rotation and appearance of intermediate low symmetry M or O phases. In the view of tailoring materials properties, the most important issues are *why the induced intermediate phases exist near the MPB*. It is important to note two things: (i) dielectric constant measurements have shown that the relaxor characteristics remain in PMN-xPT up to x=0.35;[45] and (ii) diffusive scattering by both synchrotron x-ray and neutron have shown that PNRs present in PMN-xPT for PT concentration far above the MPB until x=0.6.[46] Accordingly, it is reasonable to suggest that PNRs must be related to intermediate phases. However, how PNRs assemble into a structural inhomogeneous state is still not clear.

1.3 Ferromagnetic and ferroelastic-like biferroics

Joule magnetostriction is the phenomenon in which the shape of a ferromagnetic material changes with magnetization. The inverse Joule magnetoelastic effect (Villari Effect) is characterized by the change of magnetization upon application of a stress. In this thesis, we will only consider Joule magnetostriciton.[47] A typical magnetostrictive elongation as a function of applied magnetic field is illustrated in Fig.1-14. The magnetostrictive ($\delta l/l$) changes with increasing magnetic field and saturates at a value of λ_s. If the magnetostrictive strain is positive, the effect is called positive magnetostriction; otherwise it is designated as negative magnetostriction. Ferromagnetic materials are always magnetostrictive matierials, however not all of them can be considered as ferroelastic. What we are interested is ferromagnetic materials with ferroelastic-like behavior, which gives rise of large magnetostriction in materials even though the magnetic anisotropy is weak.

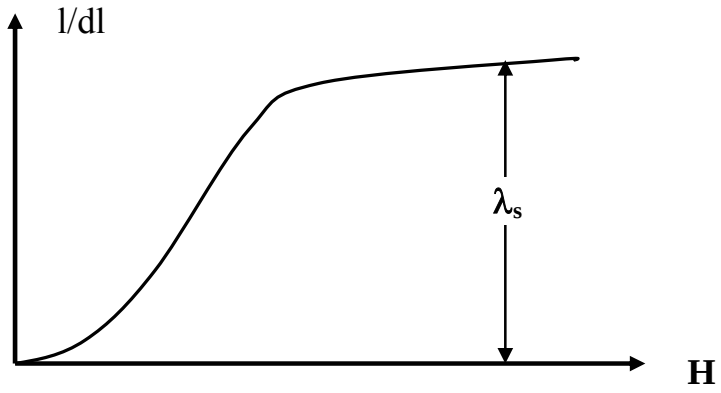

Fig.1-14. Magnetostrictive elongation as a function of applied magnetic field.

1.3.1 Origin of magnetostriction

Magnetostriction has its origin in a coupling between the direction of the spin moment of an atom and the orientation of its anisotropically shaped electron charged cloud, i.e. the "spin-orbit coupling".[47] When the atomic magnetic moment (the dipole-dipole exchange energy) changes under external magnetic field, the distance and angle of a dipole moment pair will spontaneously adjust to achieve minimum energy. Accordingly, the crystal will deform to some finite strain such that an equilibrium state will be reached. Analytically, the equilibrium state can be obtained by minimizing the total energy of magnetocrystalline energy (E_k), elastic energy (E_{elas}) and magnetoelastic energy (E_{ms}),

$$E = E_K + E_{elas} + E_{ms} \qquad [1.8]$$

Detailed discussion of elastic and magnetoelastic energies can be found in reference book by Etienne du Trémolet de Lacheisserie.[48] Table 1.2 lists the properties of some magnetostricitive materials.

In a cubic single crystal, the saturation magnetostriction along the [100] and [111] directions can be written as

$$\lambda_{[100]} = -\frac{2b_1}{3(C_{11} - C_{22})}, \qquad [1.9(a)]$$

$$\lambda_{[111]} = -\frac{b_2}{3C_{44}} \qquad [1.9(b)]$$

where C_{11}, C_{12} and C_{44} are the elastic coefficients of a cubic crystal, and b_1 and b_2 are the magnetoelastic coefficients. Thus, it is possible to enhance magnetostriciton by increasing b_1 and/or decreasing $\frac{1}{2}(C_{11}-C_{12})$.

Table 1-1. Magnetostriction of some materials at room temperature

Crystals	λ_{100} ($\times 10^{-6}$)	λ_{111} ($\times 10^{-6}$)	$\lambda_{[100]} = \frac{2\lambda_{100} + 3\lambda_{111}}{5}$ ($\times 10^{-6}$)
Fe	20.7	-21.2	-4.4
Ni	-45.9	-24.3	-33
85%Ni-Fe	-3	-3	-3
40%Co-Fe	146.8	8.7	64
19%Ga-Fe	265	28	123
19%Al-Fe	106	5	45.4
Fe_3O_4	-20	78	39
$Mn_{1.05}Fe_{1.95}O_4$	-28	4	-8.8
$Mn_{0.4}Zn_{0.1}Fe_{2.1}O_4$	-14	14	3
$Ni_{0.8}Fe_{2.2}O_4$	-36	-4	-17
$Ni_{0.3}Zn_{0.45}Fe_{2.25}O_4$	-15	11	0.6
$Co_{0.8}Fe_{2.2}O_4$	-590	120	164
$Co_{0.8}Zn_{0.2}Fe_{2.2}O_4$	-210	110	-18
$Tb_{0.3}Dy_{0.7}Fe_2$		1200	
$Ni_{49.8}Mn_{28.5}Ga_{21.7}$*	60,000		

* Ni_2MnGa is a magnetic shape memory alloys.

1.3.2 Large magnetostriction in binary alloys

The magnetostriction of body-centered cubic (bcc) Fe is known for its near compensating constant and anomalous temperature dependence: λ_{100} attains a minimum around 400 K and then again rises to a maximum just before the Curie temperature of Fe.[49] In search of a material that has superior magnetic properties relative to pure Fe, there have been significant efforts to alloy Fe with various non-magnetic species, both transition and non-transition metal elements. These elements include Ti, Co, Ge, Si, Cr, Mo, Al, V and etc.[50]

With regards to magnetostriction, Fe-x at.%Al alloys have attracted much interests, where the λ_{100} reaches about 80~100 ppm, 4x that of pure Fe crystal, for x=19 and then decreases with further increment of Al concentration.[50] Hall has shown that the magnetocrystalline anisotropy constant K1 for both order and disordered Fe-Al alloys decreases sharply with increasing Al content and goes through zero, meaning that a low magnetic field can reach saturation magnetostriction for cubic crystals.[50] Leamy et al. have shown for disordered alloys that additions of 20 at.%Al to Fe decreases $\frac{1}{2}(C_{11}-C_{12})$ by nearly half of that of the Fe value and slightly increases C_{44}.[51]

Ga and Al belong to the same chemical group in the periodic table, sharing similar electronic configuration. Accordingly, some similarities in phase stability and properties of both Fe-Al and Fe-Ga alloys were anticipated. Surprisingly, Clark et al. have recently demonstrated that a significantly enhanced manetostriction (over 250 ppm) can be obtained in Fe-Ga bcc single crystals.[52] Fig.1-15 compares the saturation magnetostricition of both Fe-x at.%Ga and Fe-x at.%Al at room temperature.[53-54] Clear similarities can be seen between these two alloys. In both cases, the saturation

magnetostriction λ_{100} increases with increasing alloy concentration until x=17~19, and then decreases for larger x. In addition, it has been found that the magnetostriction of Fe-x at.%Ga is also dependent on the thermal history of the alloy, analogous to what has been reported for Fe-Al alloys. In the furnace-cooled (FC) condition, a maximum in λ_{100} is reached at x=17; whereas in the rapidly quenched (RQ) condition, the value of λ_{100} continues to increase with increasing Ga content until x=19, as shown in Fig.1-15(b).[54] And the magnetostriction of Fe-x at.%Ga alloys for 19<x<21.4 is almost 25% higher for RQ samples than that of FC ones. Even higher magnetostriction of about -700 ppm has been reported in melt-spun $Fe_{81}Al_{19}$ (~5x that of corresponding bulk materials[55]), and about 1100 ppm for melt-spun stacked Fe-15 at.% Ga ribbons with much larger cooling rate[56]. Finally, magnetic anisotropy constant measurements in Fe-x at.%Ga have shown a sharp drop of both K1 and K2 with increasing Ga concentration in the range of 5<x<20 at.%.

Fig.1-16 shows the phase diagram of Fe-x at.%Ga and Fe-x at.%Al alloys.[57] The A2 phase has a disordered cubic structure up to 15 at.% Ga. For 15<x<22.5 at%Ga, the equilibrium state is a two-phase field of A2+DO_3 phases in the FC state; whereas in the RQ condition, it is believed that the same crystal maintains a single phase A2 cubic structure until x≈19at%. A single unstable DO_3 phase exists for 22.5<x<31 at.%Ga. Above this composite range, a stable B2 phase exists. The structures of A2, DO_3 and B2 phases are also shown in Fig.1-16.

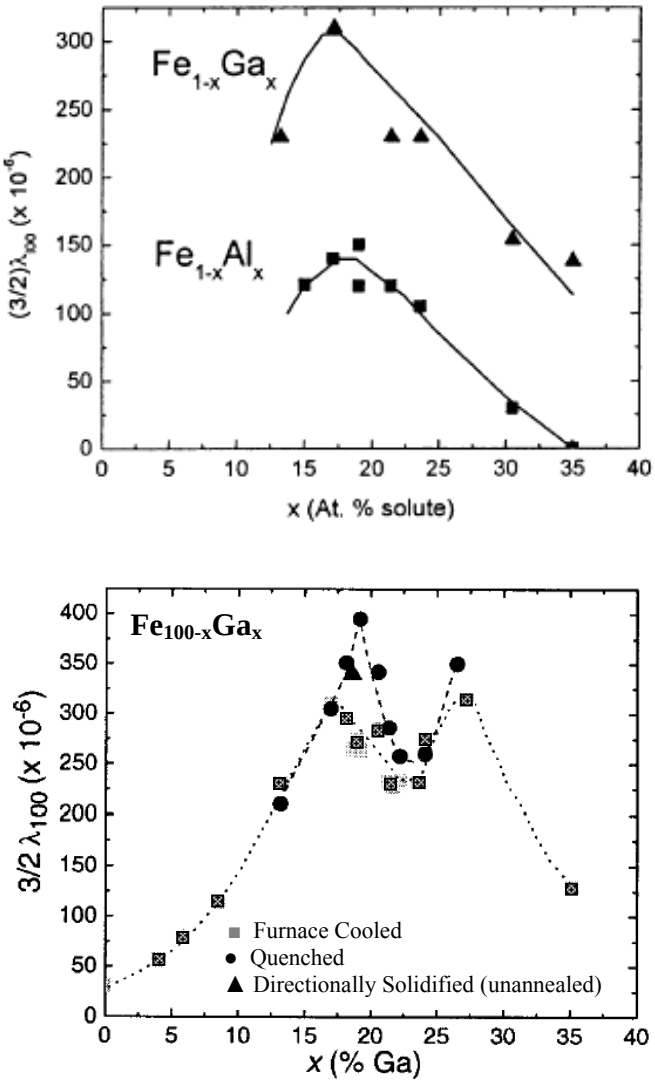

Fig.1-15. Saturation magnetostriction measured at room temperature for Fe_xGa_{1-x} and Fe_xAl_{1-x}. (b) Recent updated data by A. E. Clark et al. [Ref. 53-54]

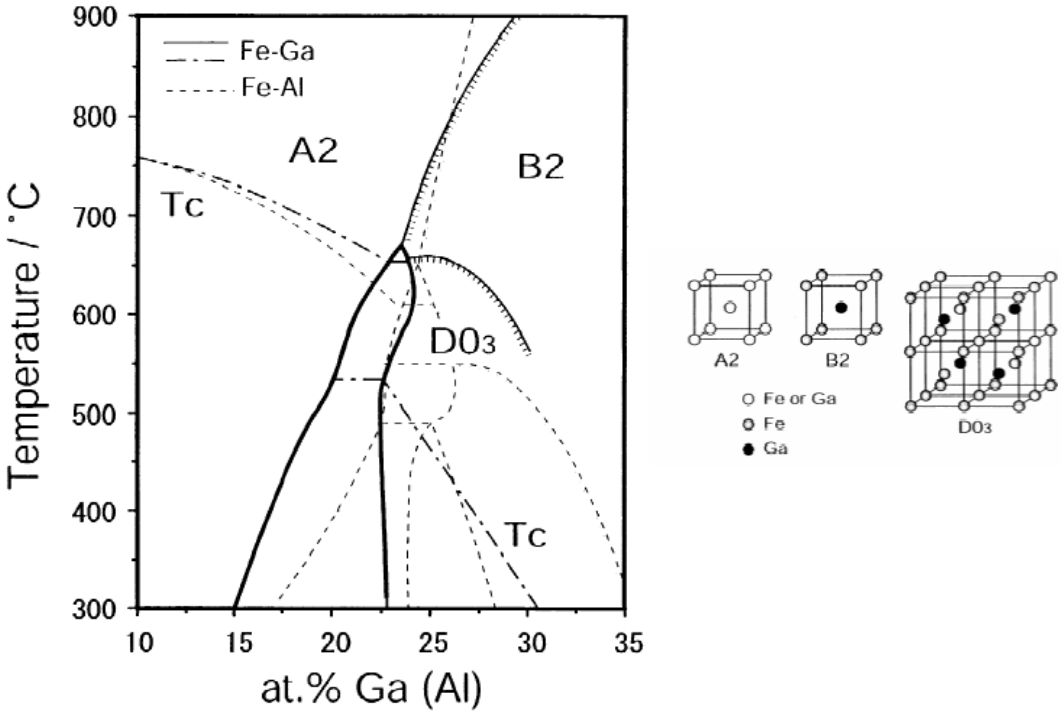

Fig.1-16. Phase equilibrium between the A2 and DO_3 or B2 phases in Fe-x at.%Ga in comparison of Fe-x at.%Al alloys. [Ref. 57]

1.3.3 Prior investigations of Fe-Ga (Al) alloys

During the investigations of the origin of large magnetostriciton in Fe-Al and Fe-Ga alloys, some clues were first noticed concerning the magnetostricion's dependence on composition and crystal orientation. In both alloys, λ_{100} increases approximately as x^2 until a maximum is reached.[58] This type of behavior suggests that the enhanced magnetostriciton is related to the presence of clusters of solute atoms (Al or Ga), which act as *magnetic and magneoelastic defects* in the alloys. A simple thermodynamic model has been developed by Wuttig et al., which predicted that the saturation magnetostriction should increase as the number of Al-Al or Ga-Ga pairs, i.e., as x^2 at small concentrations.[58] For larger concentrations, the isolated pairs are gradually replaced by larger clusters. Many of the pairs become part of these larger entities, so that the magnetostriction no longer increases as x^2. For even larger x, it is impossible to retain the disordered bcc structure, as the alloys are partially or fully DO_3 or B2 structured, thus there are very few clusters in the alloy to act as magnetoelastic centers.

The effect of these clusters was evidenced by the measurement of the magnetoelastic coefficient b_1 and the shear elastic constants $½(C_{11}-C_{12})$ and C_{44}, by Wuttig et al.[58] and Clark et al.[54], respectively. It was found that while the rhombohedral shear elastic constant C_{44} is independent of Ga concentration, the tetragonal shear elastic constant $½(C_{11}-C_{12})$ decreases linearly with increasing Ga content and extrapolates to zero near 27 at.%Ga,[58] as shown in Fig.1-17. Meanwhile, the magnetoelastic constant $|b_1|$ was found to increase from 2.9 to 15.6 MJ/m^3 at x=18.7 at.%, and then to decrease for higher Ga concentrations.

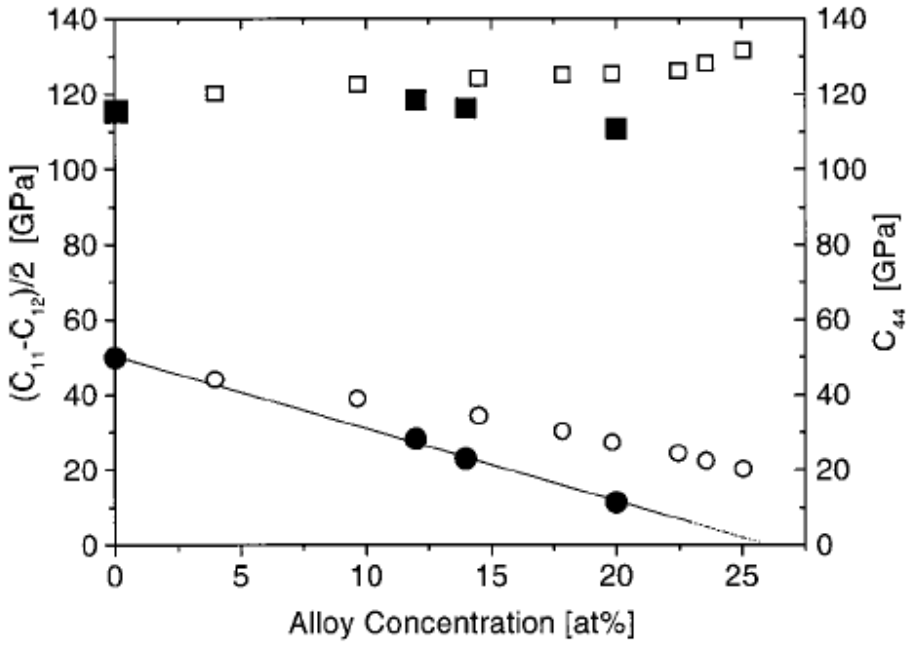

Fig.1-17. Shear elastic constants ½ (*C*11–*C*12), circles, and *C*44 , squares, of bcc Fe–Ga solid solutions, full symbols, determined in this study. The open symbols represent the elastic constants of bcc Fe–Al solid solutions. [Ref.58.]

Furthermore, it has been found that the increase of λ_{111} with increasing x is almost negligible compared to λ_{100} for both Fe-Al and Fe-Ga alloys, consistent with the measurements of C_{44}, as shown in Fig.1-18.[58] This supports the presumption that there are no nearest neighbor pairs along the <111> direction, because of the size difference between Ga (or Al) and Fe atoms. The next nearest neighbors are along the [100] direction and contribute to the enhancement of λ_{100}, thus relating the thermodynamic model to the pair model of magnetostriction. Lograsso et al. have suggested a modified DO_3 structure, as illustrated in Fig.1-18.[59] Wu has also conjectured a B2-like tetragonal structure, taking into account Ga pairs along the <100> directions, which was believed to play a key role in the strong positive magnetostriction in Fe-Ga alloys.[60] Wuttig et al suggested that these local tetragonal features are premartensitic embryos.[58] In this sense, the enhanced "magnetostriction" in Fe-Ga alloys can be considered as being ferroelastic-like strain instead of a simple magnetostriction. *However, up to now, no conclusive structure evidence has been presented that demonstrates either tetragonal distortions or magnetization inhomogeneities.*

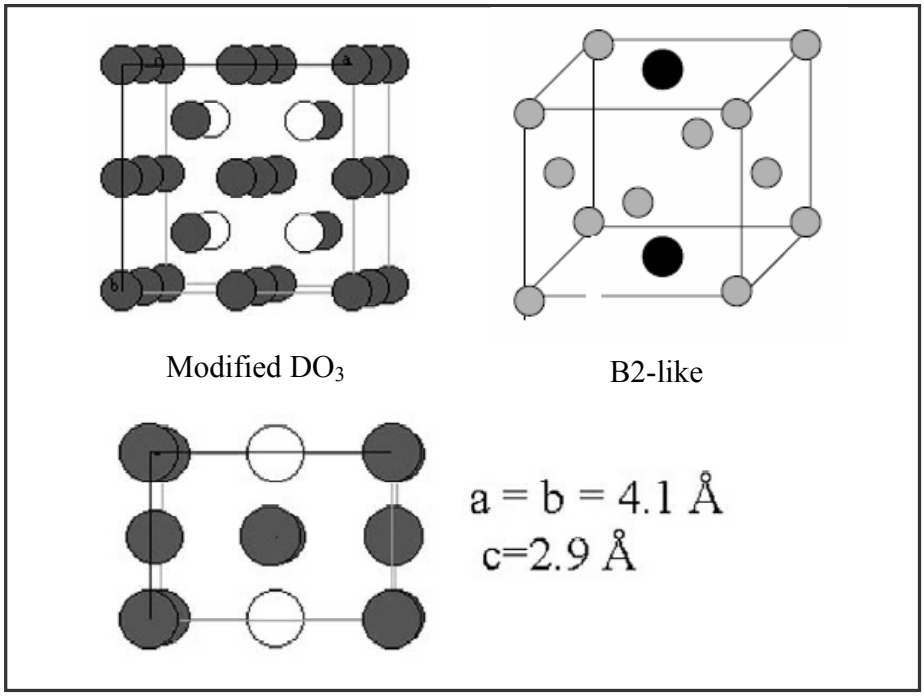

Fig.1-18. Schematic illustration of modified DO_3 and B2-like lattice structure.[Ref.59-60]

II. PURPOSE OF THIS THESIS

Two multiferroic materials will be investigated in my dissertation work: they are ferroelastic-ferroelectric $Pb(Mg_{1/3}Nb_{2/3})O_3$-$PbTiO_3$ (PMN-PT) and ferromagnetic-ferroelastic-like Fe-Ga alloys. Attention will be given to the nanoscale inhomogeneities in these materials and their roles in the enhancement of materials properties.

Domain-engineered states in PMN-PT or PZN-PT crystals have been interpreted as homogeneous intermediate low-symmetry phases. However, as discussed in the introduction, structural inhomogeneities entities (i.e. PNR) are known to exist over a wide composition range for relaxo-normal crystalline solution. Clearly, it is reasonable to suggest that intermediate phases could be related to PNR. But how? How does nature assemble a structural inhomogeneous state of PNR into various states with apparent M or O symmetry. To address this question, a combination investigation of phase transformation characteristics on the macro scale and domain structure in nano scale is needed. The results sections will attempt to provide some answers to the following,

1) What is the phase transformation sequence during poling and in the after-poled state? There are two poling schemes: field cooling from a temperature above T_c to room temperature, and increasing field at a constant temperature. The electric field vs. temperature (E-T) diagram needs to be established. [Please see Section 4.2]

2) How do domains evolve during the phase transformation sequence of $C \rightarrow R \rightarrow M_c \rightarrow T$ in the phase diagram, and what is the role of PNR on this sequence? Is there a domain hierarchy with different symmetries on different

length scales? Accordingly, a detailed investigation is needed to study the domain structures of PMN-x%PT over various length scales from nano- to milli-meter for different x near the MPB. [Please see Section 4.3]

3) Are the domain distributions of PMN-x%PT in the zero-field-cooled and field-cooled conditions different, possibly reflecting differences in the phase transformation sequence? How do such differences in domain distributions depend on composition about the MPB? [Please see section 4.4]

4) How do domain configurations evolve during poling and/or polarization reversal? [See Section 4.5]

Due to limited spatial resolution, polarized optical microscopy (POM) only provides an averaged macro domain structure in the micro and larger scales. So we will also use piezoresponse force microscopy (PFM) to study the evolution of the domain structure on a nano-meter-length scale for PMN-x%PT crystals with different x. The results will compare to those obtained by POM. Detailed experiment methods will be given in Chapter 3.

As discussed in Section 1.3 for the binary Fe-x at.% Ga(Al) alloys, both the increase of the magnetoelastic coupling coefficient (b1) and the decrease of tetragonal elastic constant $\frac{1}{2}(C_{11}-C_{12})$ with x are believed to be related to the changes in the number of Ga pairs. This is a conjecture built upon two hypothesis: (i) at least a small tetragonal splitting induced by Ga pairs; and (ii) composition segregation that results in magnetic spin reorientation. However, neither have yet been reported, although earlier neutron scattering work in Fe-25at.%Al has shown evidence of an anomalous *inhomogeous*

magnetism or "cluster glass".[61] So the primary tasks of my dissertation work is to address these unanswered questions, specifically

5) Is there low-symmetry lattice distortion in Fe-x at.% Ga with the increment of Ga-concentration? Both line scans and mesh scans in different reciprocal zones will be performed. [Please see section 5.2]

6) Are there magnetic domain inhomogeneities? How does change in the degree of magnetic domain alignment depend on composition and how might this dependence relate to the changes in magnetostriction? Why does the location of the maximum magnetostriction shift in the phase field with changes in thermal history? To answer these questions, the thermal history dependence of the magnetic domain distribution will be studied for Fe-x at.%Ga in the vicinity of A2-DO_3 boundary. [Please see section 5.3]

7) How does magnetic domain rotate during applying magnetic field along longitudinal and transverse direction? What is the effect of lattice distortion on magnetic spin reorientation? The magnetic domain structures of Fe-x at.% Ga will be compared during magnetization alignment/reversal. [Please see section 5.4]

Magnetic force microscopy (MFM) is an excellent tool to study magnetic domain inhomogeneities due to the high resolution and sensitivity. As for structure investigation, X-ray diffraction has only low penetration depth about 3~5 μm. It is necessary to perform neutron scattering to get the bulk information. Details of the MFM and neutron scattering methods will be discussed in the following chapter.

III. EXPERIMENT TECHNIQUES

3.1 Preparation of samples

3.1.1 $Pb(Mg_{1/3}Nb_{2/3})O_3$-$PbTiO_3$ single crystals

PMN-PT single crystal were grown by a vertical Bridgmen–Stockbarger method, using a sealed platinum crucible by self-seeding, and were obtained from HC Materials (Urbana, IL).[62-63] The starting materials were high purity PbO, MgO, Nb_2O_5, and TiO_2 (the purity is better than 99.99%). The starting powders were weighed to be the same chemical ratio as the formula PMN-*x*%PT (x=10, 20, 30, 35 and 40), as shown in Fig.3-1, and were mixed thoroughly in an agate mortar and pestle, and then loaded into a platinum crucible. The maximum temperature in the furnace was at 1395 °C and the crystal growth rate was controlled at 0.4 mm/h at a temperature gradient of 20 °C/cm, which yields optimum results for growing this type of relaxor ferroelectrics.

For optical and piezoresponse force microscopy (PFM) studies, all crystals were cut into plates with typical dimensions of 4x4x0.5 mm^3. The top faces of the crystals were polished to 0.25 μm finishes. For X-ray and neutron diffraction, a PMN-30%PT crystal was cut into a cube of dimension 4x4x3 mm^3. All faces of the crystal were again polished to a 0.25 μm finish. A gold electrode was then deposited on two 4 x4 mm^2 faces by sputtering (SPI-Module Sputter Coater). Before measurements were begun, all crystals were annealed at 550 K for 30 min to remove surface stresses.

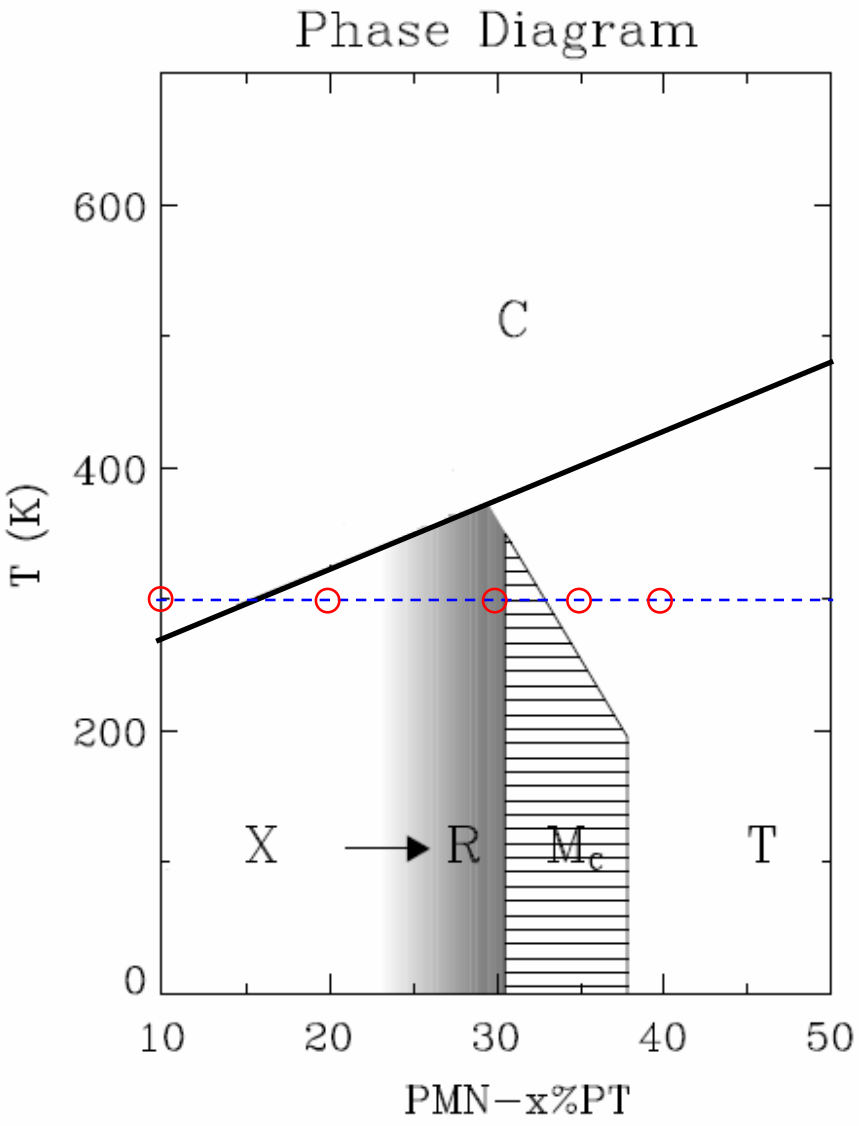

Fig.3-1. Phase diagram of PMN-x%PT crystalline solutions. Of particular interests are 10PT (Cubic), 20PT (Rhombohedral), 30PT (Rhombohedral), 35PT (Monoclinic+Tetragonal) and 40PT (Tetragonal), as labeled by red circle. [Ref. 64]

3.1.2 Fe-Ga single crystals

Crystals used in this investigation were grown at Ames Laboratory by a Bridgman method in a resistance furnace, as previously described.[52] Appropriate quantities of iron and gallium were cleaned and arc melted several times under an argon atmosphere. The buttons were then remelted and the alloy drop cast into a copper chill cast mold to ensure compositional homogeneity throughout the ingot. The nominal compositions of the ingot are $Fe_{87.7}Ga_{12.3}$, $Fe_{80}Ga_{20}$ and $Fe_{74.4}Ga_{24.8}$, whose locations in the phase diagram is shown in Fig.3-2.[54] The as-cast ingot was placed in an alumina crucible and heated under a vacuum to 900^{o}C. After reaching 900^{o}C, the growth chamber was backfilled with ultra high purity argon to a pressure of 1.03×10^{5} Pa. This over-pressurization is necessary in order to maintain stoichiometry. Following pressurization, heating was continued until the ingot reached a temperature of 1600^{o}C and held for 1 hour before being withdrawn from the furnace at a rate of 4mm/hr. The ingot was annealed at 1000^{o}C for 168 hours, using heating and cooling rates of 10 degrees per minute, after which the crystals are considered to be in the "furnace-cooled" (or FC) state.

Samples were then oriented and sectioned from the ingot. All crystals were of dimensions 10x10x2 mm^3. The (001)-oriented 10x10 mm^2 faces were polished using standard metallographic techniques down to 0.3 μm finish. Careful investigations were performed using MFM, by starting from the FC state, and then again after being post-annealed (PA) at 750^{o}C or higher temperature (above Curie temperature) in an ambient of argon for one hour.

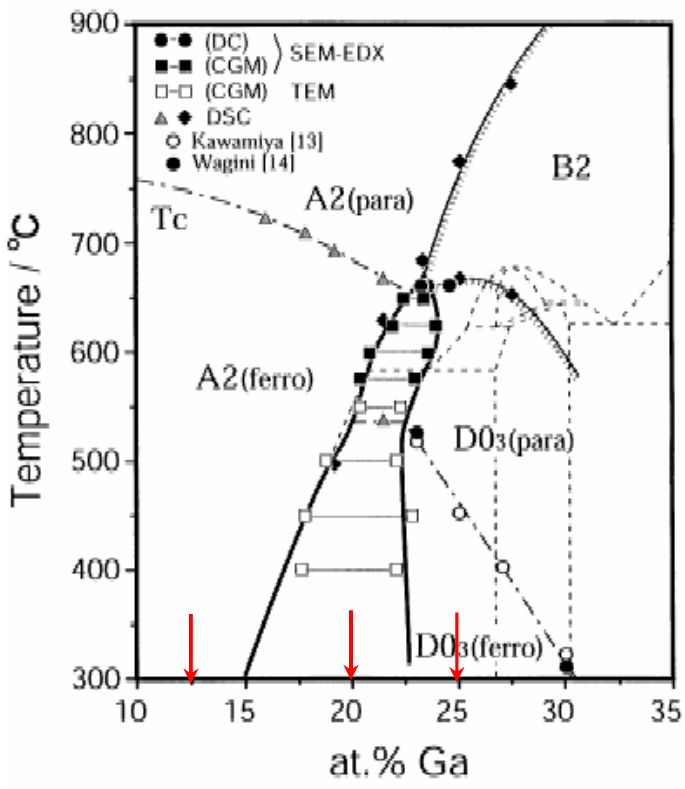

Fig.3-2. Phase equilibrium between the A2 and DO_3 or B2 phases in Fe-x at.%Ga alloys. Of particular interests are 12Ga, 20Ga and 25Ga locating in A2, A2+DO_3 and DO3 phase regions, as marked by red arrows. [Ref. 57]

3.2 Characterization methods

3.2.1 X-ray diffraction

The XRD system used during my studies was a Philips MPD high resolution x-ray diffractometer equipped with a two bounce hybrid monochromator, an open 3-circle Eulerian cradle, and a domed hot-stage. A Ge (220) cut crystal was used as analyzer, which had a 2theta-resolution of ~0.0068^{o} (or 0.43 arcseconds). The x-ray wavelength was that of $Cu_{K\alpha}$ (λ=1.5406 Å) and the x-ray generator was operated at 45 kV and 40 mA. XRD was used to perform (i) high-resolution 2θ line scan (single scan) to measure lattice parameters, both at room temperature and as a function of temperature up to 650 K; (ii) rocking curve (ω scan) to determine the maximum peak intensity (ω is then fixed during 2θ line scan in the field cooling or heating condition); and (iii) ω-2θ mesh scan (area scan) as functions of temperature and electric field to determine the crystal symmetry and domain distributions. All the angles are illustrated in Fig.3-3(a).

The ω-2θ mesh scan shows the area of reciprocal space covered when ω-2θ line scans with a range of, for example one degree, are made over a range of one degree in ω. The (200) and (002) mesh scans in reciprocal space and real space are schematically illustrated in Fig.3.3(b). Mesh scans can reflect multi-domain patterns caused either by different lattice parameters (2θ) or by various angles between the crystallographic plane and incident beam (ω). Thus, it is very useful method to determine the symmetry of a sample, by analyzing domains distributions in different reciprocal zones.

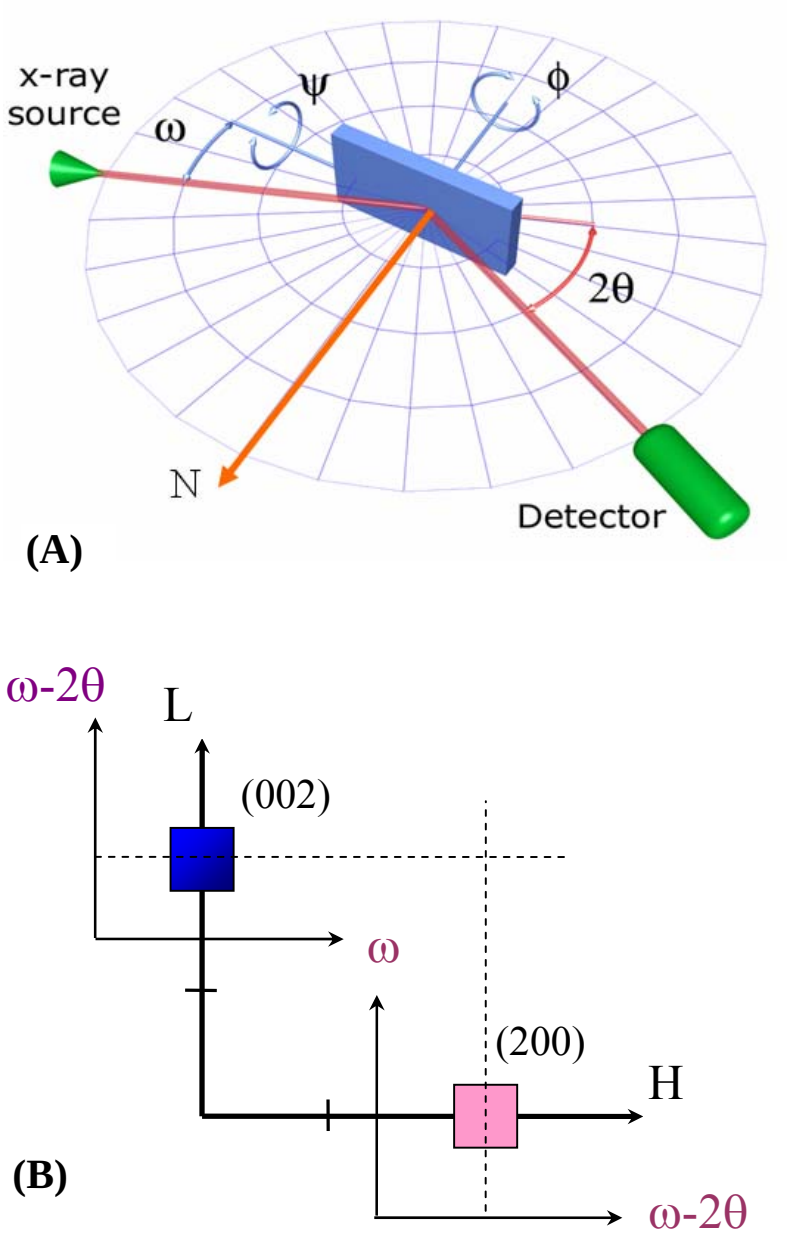

Fig.3-3. Schematics illustration of (a) Philips MPD high resolution x-ray diffractometer; and (b) (200) and (002) mesh scans in the reciprocal (H0L) zone, which are same with two ω-2θ mesh scans in the real space.

3.2.2 Triple-axis neutron scattering

Due to the limited penetration depth of X-rays, neutron scattering is necessary to obtain the bulk information concerning a crystal. Similar to X-rays, neutrons are also diffracted by crystals, following the well-known Bragg's law:

$$\boldsymbol{G}=\boldsymbol{k_f}-\boldsymbol{k_i} \qquad [3.1]$$

$$|\mathbf{G}|=2|\mathbf{k_i}|\sin\theta \qquad [3.2]$$

where **G** is a reciprocal lattice vector, $\mathbf{k_i}$ is the direction of the incident beam relative to the crystal, $\mathbf{k_f}$ is the direction of the diffracted beam, and 2θ is the angle between the incident and diffracted beam for the Bragg condition.

The triple-axis spectrometer (TAS) is the most versatile and useful instrument for use in both elastic and inelastic scattering because it allows one to probe nearly any coordinates in energy and momentum space in the precisely controlled manner. Fig.3-4 shows the schematic diagram of a triple-axis spectrometer;[65] specifically note

1) The first axis of rotation is around the monochromator crystal, where neutrons of a specific wavelength are extracted from the neutron beam and Bragg reflected onto the sample. Diffraction conditions at the monochromator crystal ensure that the neutron beam incident on the sample is monochromatic with fixed initial energy and wavevector (E_i, k_i).
2) The second axis of rotation is at the sample position, where neutrons are scattered inelastically by the sample. The single-crystal sample is mounted with the scattering plane of interest oriented horizontally (i.e. in the plane of the beam).

3) Finally, neutrons scattered by the sample, (possessing a distribution of final energies and wave vectors), are then incident on an analyzer crystal positioned at the third axis. The analyzer is aligned in order to reflect neutrons of a specific energy and wave vector onto the detector.

Since the scattering plane is horizontal, the scattering observed at the detector is a function of only three variables; the energy transfer ($E = E_f - E_i$), and the two components of momentum transfer (scattering vector **Q**) in the plane.

The neutron scattering experiments in this thesis were performed on the BT9 triple-axis spectrometer located at the NIST Center for Neutron Research. Measurements were made using a fixed incident neutron energy E_i of 14.7 meV (wavelength λ=2.359 Å), obtained from the (002) reflection of a PG monochromator, and horizontal beam collimations of 10'-46'-20'-40'. We exploited the (004) reflection of a perfect Ge crystal as analyzer to achieve unusually fine q-resolution near the relaxor (220) Bragg peak, thanks to a nearly perfect matching of the sample and analyzer d-spacings. Close to the (220) Bragg peak, the q–resolution along the wave vector direction is about $0.0012 Å^{-1}$ ($\Delta q/q \approx 2x10^{-4}$).[14]

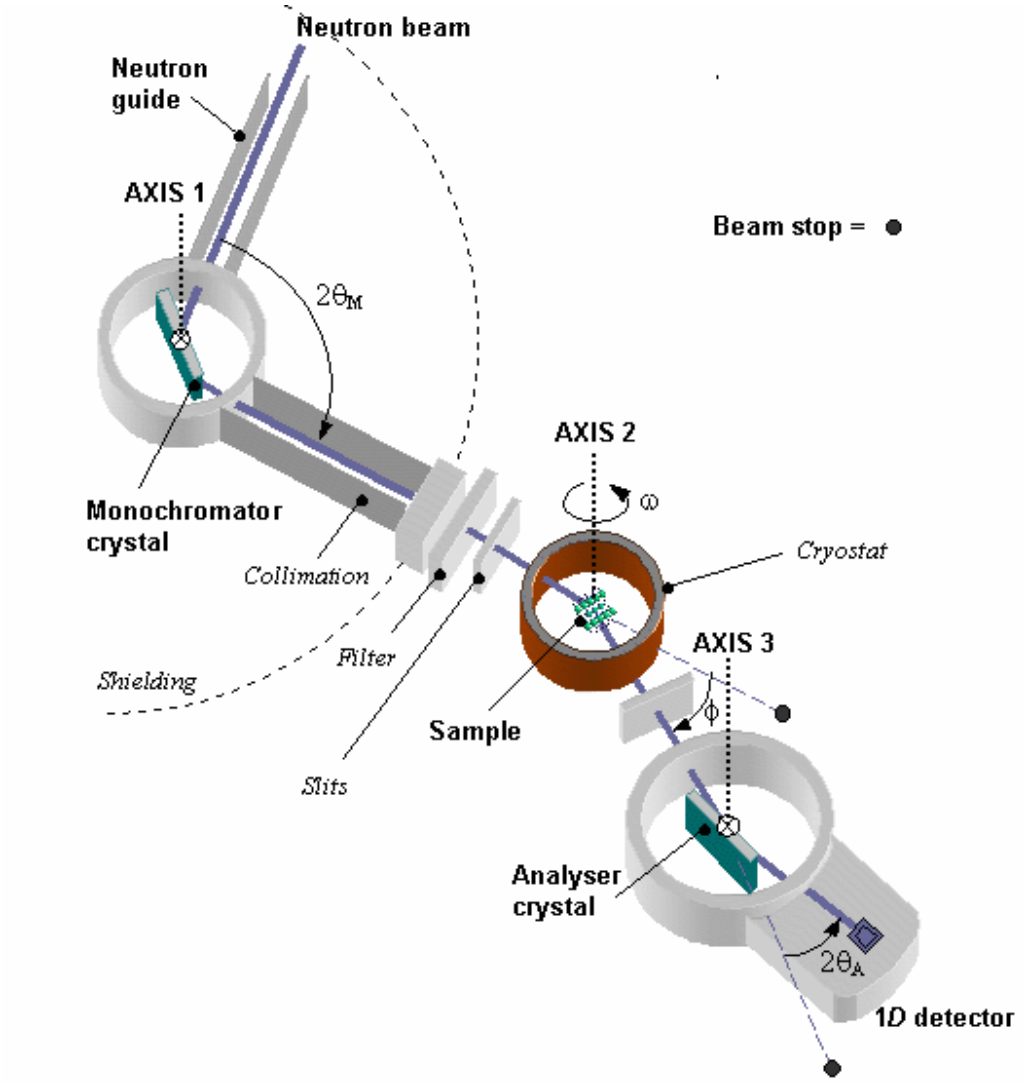

Fig.3.4. Schematic diagram of neutron triple-axis spectrometer (http:// **www.physics.uc.edu/ ~jph/emma/tas.html**)

3.2.3 Scanning force microscope (SFM)

The operation principle of a scanning force microscope (SFM, also call scanning probe microscope, SPM) is based on the detection of the position of a soft cantilever-type spring with a sharp tip mounted at its end. When the tip approaches the sample surface, the forces acting on it causes a deflection of the cantilever according, in a first approximation, to the Hooke's law. The degree of bending can be controlled by a feedback loop, which regulates the vertical position of the tip with respect to the sample surface. By keeping the deflection constant while scanning the sample, a three-dimensional map of the surface topography can be obtained. It can be seen that the key point of the system is mapping the "tip-sample interaction".

There are two main modes of operation according to the type of interaction between the SFM tip and the sample: contact and tapping. In the contact mode, the tip always contacts the sample surface during scanning, and the force between tip and sample maintains a constant value (setpoint), which is controlled by the feedback loop. In the tapping mode, the cantilever is oscillated at or near its resonance frequency with an amplitude ranging typically from 20 to 100 nm. The tip lightly "taps" on the sample surface during scanning, only contacting the surface at the bottom of its swing. The feedback loop keeps a constant oscillation amplitude (setpoint), as shown in Fig.3-5, by which a constant tip-sample interaction is also maintained during imaging. Contact mode has higher scan speed than tapping mode, whereas tapping mode has better lateral resolution on most samples (1~5 nm) and less damage to both the tip and sample. Contact mode works well in detecting real-time strain changes, while tapping mode is more suitable to sense long-distance magnetic or electrostatic interaction.

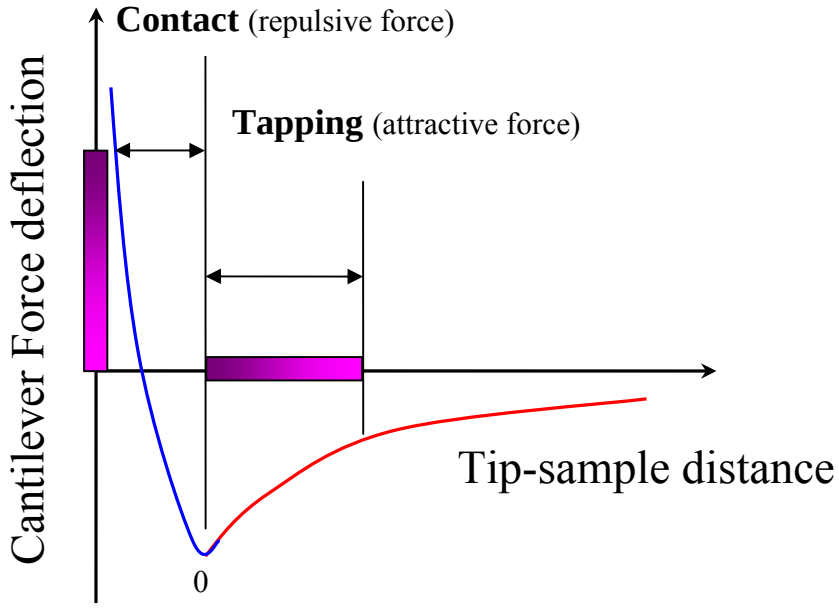

Fig.3-5. Force deflection versus tip-sample vertical distance plot. Contact mode works in the repulsive force range with preset cantilever deflection, "setpoint"; tapping mode works in the attractive force range with preset cantilever oscillation amplitude, "setpoint". The "setpoints" are labeled by two color bars, and light color corresponds to the increase of either repulsive or attractive force.

3.2.4 Piezoresponse force microscopy (PFM)

Also called voltage-modulated scanning force microscopy, this method has proven to be the most suitable method to study and control the ferroelectric domain structure at the nanometer scale. The advantage is that it allows simultaneous modification and detection of the ferroelectric polarization on a local level.

Principle of PFM

The piezoresponse-SFM technique is based on the converse piezoelectric effect. Since all ferroelectrics exhibit piezoelectricity, an electric field applied to a ferroelectric sample results in changes of its dimensions. To detect the polarization orientation, the SFM tip is used as a top electrode, which can be moved over the sample surface. To illustrate the imaging mechanism, let us consider the simplified example circuit shown in Fig.3.6, with the ferroelectric sample sandwiched between a bottom electrode and the conductive SFM tip. Also, let us consider two ferroelectric domains having opposite orientations of polarization, perpendicular to the sample surface. In Fig.3-5(a) no voltage is applied between the electrodes and the two ferroelectric domains have the same dimensions along the z-direction, as the spontaneous strain is identical for both 180^{o} domains. When a voltage is applied to the tip, the electric field generated in the sample causes the domains with the polarization parallel to the field to extend and the domains with opposite polarization to contract. The images (b) and (c) in Fig.3-6 illustrate the z-deformation of the domains when a positive, respectively negative voltage with respect to the bottom electrode, is applied to the tip.[66]

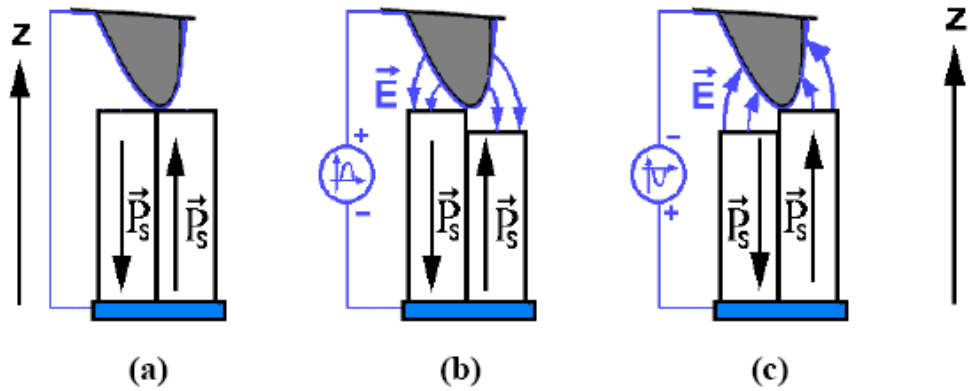

Fig.3-6. Principle of piezoresponse SFM (a) No topographic contrast if no voltage is applied. (b) A change in thickness occurs for a positive voltage applied to the tip (or during the positive half periods of an AC voltage). (c) Opposite thickness changes for a negative voltage (or during the negative half periods). [Ref.66]

Using the constitutive equations for the piezoelectric effect and the above assumptions, the following relation can be obtained:

$$\Delta z = -d^* \cdot V \qquad [3.3]$$

where $d^*=d_{33}$ for positive domains with $P_z>0$; $d^*=-d_{33}$ for negative domains with $P_z<0$.

A typical numeric value for the piezoelectric coefficient, d_{33} = 50 pm/V and applied voltage 4 V, results in a piezoelectric deformation of about 0.2 nm. This value is very close to the lower resolution of a typical SFM, and such a displacement can be easily obscured by topographic features of 5 nm to 10 nm. Therefore, a DC voltage method is not suitable to monitor the ferroelectric domains on rough surfaces. Using an AC method combined with lock-in detection considerably improves the signal-to-noise ratio. By replacing the voltage in Eq. 3.3 with $V=V_{AC}\ \sin(t)$, the surface movements induced underneath the tip are given by:

$$\Delta z = -d_{33} \cdot V_{AC} \sin(\varpi t) \quad \text{for } P_z>0, \text{ or} \qquad [3.4(a)]$$

$$\Delta z = d_{33} \cdot V_{AC} \sin(\varpi t) \quad \text{for } P_z<0. \qquad [3.5(b)]$$

Therefore, opposite orientations of polarization along the z-axis cause the sample surface to vibrate out of phase under a small AC voltage. The name "*voltage-modulated SFM*" of this method originates from the fact that during the scanning process, the SFM tip passes across different ferroelectric domains which modulate the carrier of information (the AC oscillation) with their mechanical response, according to the local polarization orientation.

Set-up of PFM

As shown in Fig.3-7, the vertical position of the SFM tip (or its deflection) is usually monitored using a laser beam, which is reflected by the cantilever on which the SFM tip is mounted.[66] Using an optical detector, the cantilever bending is converted into an electrical signal and is further processed by the SFM controller. In the PFM mode, the deflection signal also contains the induced oscillations of the sample surface transmitted to the tip cantilever. These electrical oscillations can be simply extracted from the global deflection signal using a lock-in amplifier. The lock-in detection rules out any other harmonic components of the deflection signal and the piezoelectric oscillations are in this way separated from the topography. The signal detected by the lock-in amplifier is usually referred to as the *piezoresponse* signal, [29] and is directly related to the amplitude and phase of the surface vibration *via* the detector sensitivity δ :

$$v_{\varpi} = \delta \cdot \Delta z_0 \sin(\varpi t + \Phi) \qquad [3\text{-}6]$$

where $\Delta z_0 = d_{33} V_{AC}$, $\Phi = \pi$ for positive domains and $\Phi = 0$ for negative domains. The piezoresponse signal expressed here contains information about the polarization orientation of the area under the SFM tip, *via* the phase shift Φ and also about the magnitude of the piezoelectric coefficient.

In this thesis, all ferroelectric samples were polished to 0.25 μm finishes. Gold electrodes were then deposited on the bottom face of each sample by sputtering. The electroded face was then glued to the SFM sample stage, and the opposite unelectroded surface was subjected to SFM tip scanning. PFM images were obtained using commercial equipment (DI 3100a by Veeco) equipped with Lock-in amplifier. All scans were performed

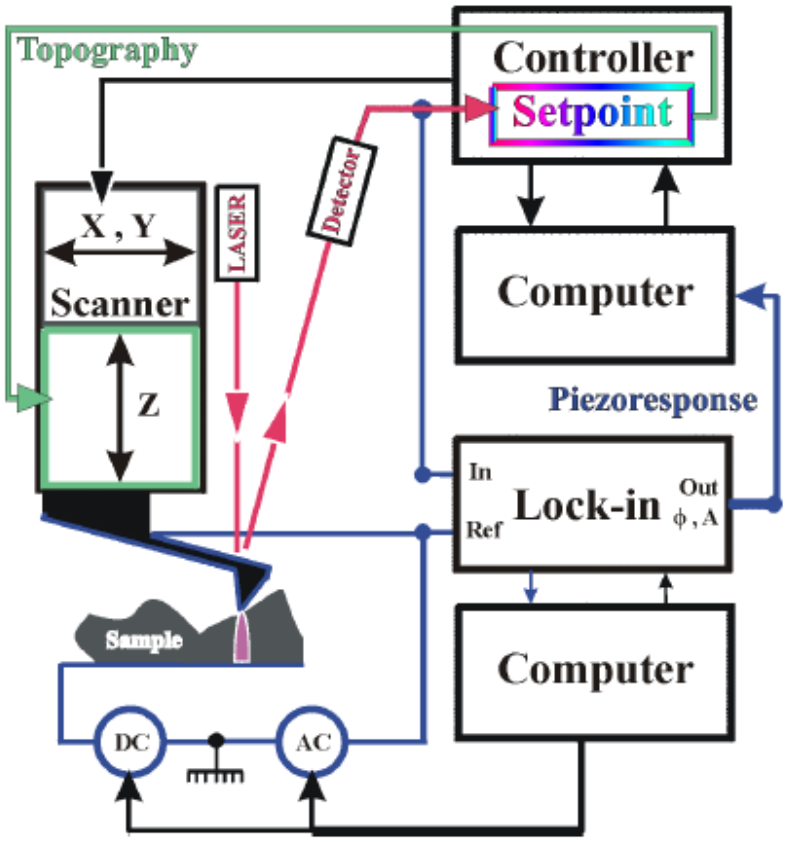

Fig.3-7. Schematic illustration of piezoresponse force microscopy set-up (Veeco DI3100a). [Ref.66]

at room temperature, using a conductive silicon-tip coated with cobalt. An ac voltage with a frequency of 20 kHz and amplitude from 1 and 10V was applied between the conductive tip and the bottom gold electrode.

3.2.5 Magnetic force microscopy (MFM)

In MFM, a tapping cantilever equipped with a special tip coated with magnetic layer first scans over the surface of the sample to obtain topographic information. Using LiftMode as shown in Fig.3-8, the tip then rises just above the sample surface. The surface topography is scanned and monitored for the influence of magnetic forces. MFM measures these influences using the principle of force gradient detection.

In the absence of magnetic forces, the cantilever has a resonant frequency f_0. This frequency is shifted by an amount Δf proportional to vertical gradients in the magnetic forces on the tip. The shifts in resonant frequency tend to be very small, typically in the range 1-50 Hz for cantilevers having a resonant frequency f_0 ~70 kHz. These frequency shifts can be detected three ways: phase detection which measures the cantilever's phase of oscillation relative to the piezo drive; amplitude detection which tracks variations in oscillation amplitude; and frequency modulation which directly tracks shifts in resonant frequency. Phase detection and frequency modulation produce results that are generally superior to amplitude detection. In this thesis, all MFM images were obtained in the phase detection mode by using a Veeco DI 3100a SFM.

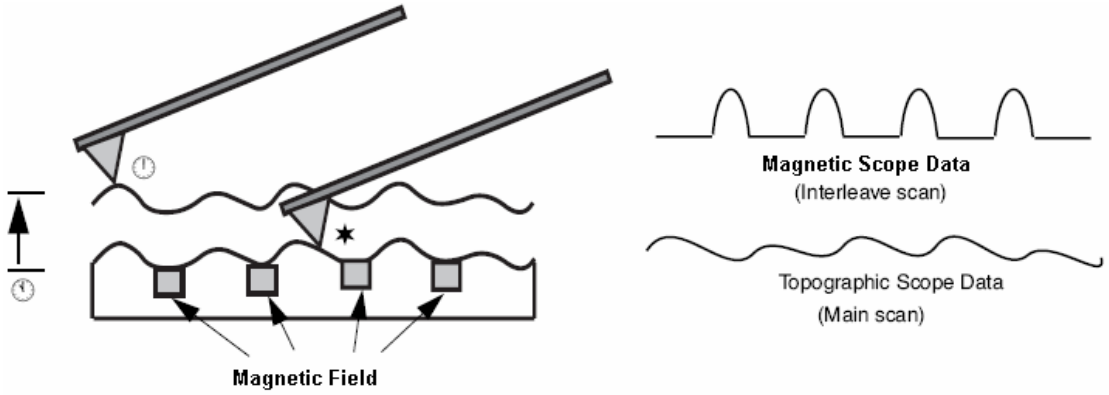

Fig.3-8. Schematic illustration of MFM working at a lifted taping mode. [Ref.67]

Qualitative analysis of magnetic force

The magnetic force between tip and sample can be written as (for simplicity reason, only static interaction will be considered)

$$F_{M-H} = \nabla E_{tip-sample} \qquad [3.7]$$

where $E_{tip\text{-}sample}$ is the energy of the tip-sample interaction. In most cases, the tip-sample interaction is substantially one-dimensional, and thus consideration of the z-component of the force derivative gives satisfactory numerical estimations.

The phase shift $\Delta\phi$ is proportional to the force derivative *F'*:

$$\Delta\phi = -\frac{Q}{k}\frac{\partial}{\partial z}F_Z \qquad [3.8]$$

In addition to the one-dimensional approximation above, some further simplified modes have been proposed to estimate the real distribution of the magnetization of the MFM tip, M_{tip}. There are two most widespread approaches: the point probe model and the extended charge model.[68-70] Expression for the monopole approximation is given as:

$$F_{M-H} = \nabla \int_{tip} M_{tip} H_{sample} dV_{tip} \rightarrow -q \cdot H_{sample} \qquad [3.9]$$

where V_{tip} is the effective imaging volume of the tip, and the total magnetization of the tip is considered as a magnetic pole, *q*. (Using dipole approximation gives the same result in Equation 3.6) Thus we have

$$\Delta\phi = -\frac{qQ}{k}\frac{\partial}{\partial z}H_Z \qquad [3.10]$$

Factors affecting resolution and sensitivity

The most important parameter affecting imaging resolution is Lift height. The range of 10–200 nm is most useful. In general, MFM resolution is roughly equal to the lift height. Smaller Lift Scan heights give better resolution; conversely, magnetic features smaller than the Lift Scan height may not be resolved. The tip also experiences stronger fields close to the surface, giving improved signal-to-noise ratios.

Another important issue about MFM is the selection of magnetic tip. Considerations should include tip sensitivity, coercivity of the tip, coercivity of the magnetic sample and resolution. For example, high sensitivity is preferred for a sample having weak external fields. In this case, a magnetic tip with a thicker coating layer should be selected. A cautionary note is that, in spite of the improved sensitivity, a thicker coating will result in a tip with a larger stray field, raising the likelihood of locally perturbing the micromagnetic structure of the sample. A thicker coating also implies reduced spatial resolution. Therefore, optimization of the MFM response to one of these considerations may sometimes come at the cost of reduced performance of another. Table 3.2 shows the two kinds of cantilevers used in this thesis.

Table 3-1. MFM cantilevers used in this thesis (standard data sheet by Veeco)[67]

Cantilever	Description	Coercivity[a]	Moment
MESP	Standard 50nm-thick Co alloy coated silicon probes.	Medium Approx. 400 Oe.	Medium. 10^{-13} emu.
MESP-HM	High-moment, 150nm-thick coated standard Co alloy thickness.	Medium ≥ 400 Oe.	High. 3.0 x standard.

IV. ROLE OF PNR IN DOMAIN ENGINEERED PMN-PT CRYSTALS

4.1 Introduction

The most dramatic feature in the phase diagram of $Pb(Mg_{1/3}Nb_{2/3})O_3$-$PbTiO_3$ (PMN-PT) and $Pb(Zn_{1/3}Nb_{2/3})O_3$-$PbTiO_3$ (PZN-PT) solid solutions is the morphotropic phase boundary (MPB), where enormous piezoelectric and electromechanical coupling coefficients have been obtained. Structural studies of $Pb(Zr_{1-x}Ti_x)O_3$ (PZT) were the first that revealed the existence of a new ferroelectric monoclinic phase, which was sandwiched between the rhombohedral (R) and tetragonal (T) phases near the MPB.[26] Two monoclinic phases, M_A and M_C, have since been reported in PZN-x%PT and PMN-x%PT.[32-34] The M_A and M_C notation is adopted following Vanderbilt and Cohen.[28] Another M_B phase was reported in PMN-x%PT ($27<x<30$).[71-72] Theoretical works by using first-principles or phenomenological approaches have suggested that the enhanced electromechanical properties near the MPB have the source of induced low-symmetry phase transitions.[27-29]

One mystery of the MPB concerns its compositional width. More precisely, different widths have been reported for the same solid solution, depending on the (i) growth conditions; (2) experiment methods (dielectric constant measurement, X-ray diffraction or neutron scattering); and (iii) the thermal and electrical history of crystals.[73] Chemical short-range ordering related polar nano regions are often invoked for this variance between different measurements, since no long-range ordering occurs in the mixed sublattice of either PZT or PMN–PT systems near their MPBs. However, why and

how PNRs affect the morphotropic phase boundary remains two unresolved questions. To answer these two questions requires evidences from both bulk phase symmetry and local domain evolution studies to establish the dependence of the MPB on composition, temperature and electric field.

Fig.3-1 previously showed the phase diagram of PMN-x%PT in the ZFC condition, replotted according to recent data published by Noheda *et al.*[36] The M_C phase extends from x=31% to x=37%. For x<31%, the phase diagram exhibits a R phase as well as a new phase, designated as X, with an average cubic structure (a=b=c).[63,74] Pronounced anisotropic peak broadening has been reported to the left of the MPB; whereas this broadening is absent to the right of the MPB.[36] This anomalous broadening has been attributed to compositional heterogeneities by Noheda et al.[36] However, Singh and Pandey have argued that the broadening in PMN-x%PT for 27<x<30 can be accounted for in terms of the Cm space group.[71] Accordingly, the structure of PMN-x%PT is R for x<27, M_B type monoclinic for 27<x<30, orthorhombic (O) for x=30, M_C type monoclinic for 30<x<35 and T for x>35.[75]

In the FC condition, previous investigations in poled PMN-35%PT crystals have shown a M_A phase at room temperature by high-resolution synchrotron XRD.[34] As for the stable phase of other poled PMN-x%PT, less data are available compared to PZN-x%PT, where a M_A phase was reported in poled PZN-4.5%PT and an O phase was reported in poled PZN-8%PT and PZN-9%PT crystals.[32-34] In addition, recent neutron diffraction studies of the effect of an electric field (*E*) on PZN-8%PT by Ohwada *et al.*[76] have shown that a cubic (C)→T→M_C transformational sequence occurs when field-cooled, and that an R→M_A→M_C→T sequence takes place with increasing *E* at 350K beginning from the

ZFC condition. An electric field versus temperature (*E*-*T*) diagram was constructed based on these experiments. However, such transformational sequence has not yet been experimentally established for PMN-x%PT under electric field. I believe that such work is very important to extend knowledge of the abnormal MPB, affected by both temperature and E-field, in relaxor systems.

Corresponding to these structural studies, counterpart investigations of the domain structure evolution with increase of PT content have been performed by polarized optical microscopy (POM)[77-80], and transmission electron microscopy (TEM)[81-83]. For example, spindle-like rombohedral domains, monoclinic domains with various optical extinction angles, and stripe-like tetragonal domains have been reported in PMN-24%PT, PMN-33%PT and PMN-50%PT crystals,[77-79] respectively. In addition, previous TEM studies have revealed miniature polar nano domains (or PND) of several hundred angstroms in size for $x<30$, where the average size decreased with decreasing x; small cross-hatched tweed-like domains for $30\approx x<35$; and normal micron-sized 90^{o} domains in the T phase,[82-83] as shown in Fig.1-9. However, these experiment results are far from satisfactory. The POM can not reveal the details of domain configurations due to limited resolution, but rather only provides a representative domain structure averaged throughout the specimen thickness. Also, the high energy of the electron beam in TEM can alter the domain configuration.

In recent years, scanning force microscopy (SFM) in the piezo-response mode (PFM) has been used to study ferroelectric domains in PMN-PT and PZN-PT crystals.[84-85] Small irregular domain structures were observed in the poled condition in both vertical and lateral piezoelectric modes, whereas large antiparallel domains were found in the

unpoled condition, demonstrating that small scale ferroelectric domain features can be identified by this method. The dependence of the domain structure on orientation has also been reported for unpoled PZN-4.5%PT crystals.[86] In the unpoled condition, small irregular domains were reported on (001)-oriented surfaces; whereas for (111) cuts, normal micron-sized domains oriented along permissible crystallographic planes were found. However, systematic domain investigations have not yet been performed comparing the morphological details over a range of length scales for the ZFC and FC domain structures, which is very important to understand the nature of the domain engineered state and resultant anomalous electromechanical properties.

In the following sections, I will present a combination phase transformation and domain structure investigation. My intention is to establish a comprehensive understanding of (i) how the phase stability of average crystal symmetry is altered with temperature and electric field (Section 4.2); (ii) how the domain configurations of different compositions are related with their symmetries in the ZFC condition (Section 4.3) and FC condition (Section 4.4); and (iii) how the domain configurations evolve during poling and switching (Section 4.5). A brief summary will then be given at the end of this chapter.

4.2. Phase transformation sequence of PMN-30%PT under E-field

In this section, my focus is on establishing the structural transformation sequence of PMN-30%PT as a function of temperature and electric field. PMN-30%PT was chosen because it locates just outside of the monoclinic phase in the phase diagram and has the highest electromechanical properties. Careful experiments have been performed using both x-rays and neutrons, starting from an annealed condition and by (i) cooling the sample from 550K to 300K under constant electric field; and (ii) gradually increasing E at constant temperature. The results unambiguously identify a transformational sequence of $C \rightarrow T \rightarrow M_C \rightarrow M_A$ in the FC condition, and of $R \rightarrow M_A \rightarrow M_C \rightarrow T$ with increasing E at constant temperature.[87]

The electric field-temperature measurements are summarized in Fig.4-1. This is done for convenience of reading – raw data will be presented in the following subsections. The top panel of this figure gives the field-cooled diagram, where measurements were made under a constant field on cooling from 500 K, whereas the bottom panel was obtained by increasing E beginning from the ZFC condition at each fixed temperature. Circles represent the transition temperatures and fields determined from each increasing field sequence. Arrows are used to indicate the scanning direction and range of the corresponding measurement sequence.

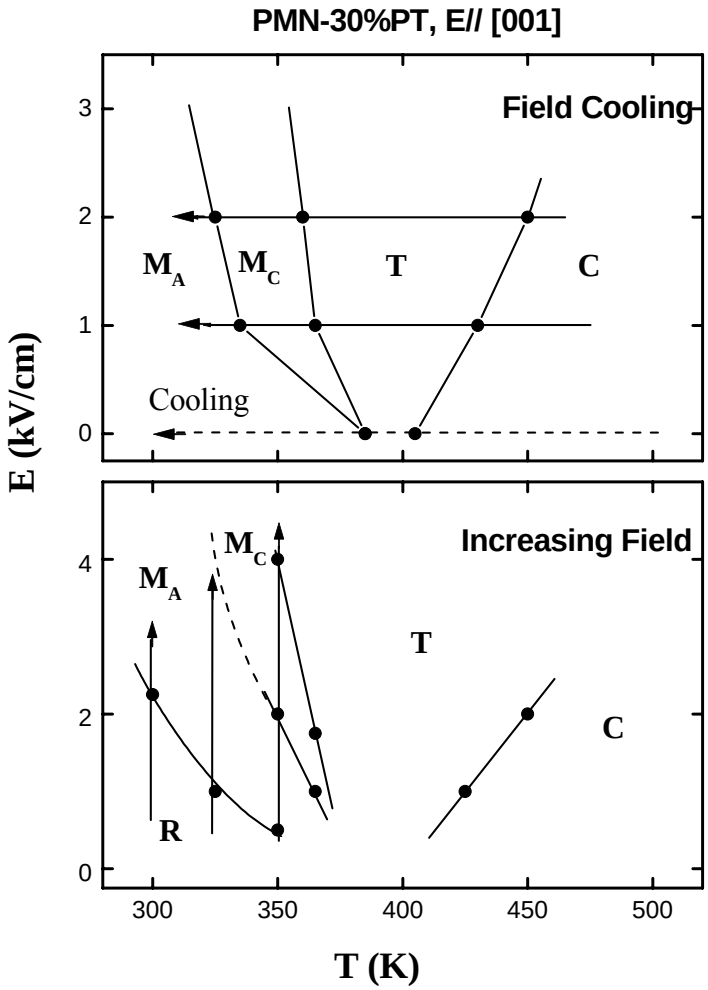

Fig.4-1. *E-T* diagram. Top panel is obtained from FC structural measurements. Bottom panel shows data from the increasing electric-field process after ZFC. Arrows indicate the scanning directions and ranges of the corresponding measurement sequences. Circles represent the transition temperatures and fields determined from each sequence.

4.2.1 XRD investigations

Phase stability in zero-field-cooled condition

The temperature dependence of the lattice parameter was investigated under zero electric field (E=0kV/cm). The specimen was first heated up to 700 K, and it was confirmed that the structure was cubic. Measurements were then made on cooling. A cubic to tetragonal phase transition was observed near 405 K associated with 90° domain formation, which was confirmed by observing a peak splitting of the (200) reflection. By fitting the (200) reflection with a double Gaussian function, we obtained the temperature dependence of the lattice constants c_T and a_T, as shown in the top panel of Fig. 4-2. On further cooling, a subsequent tetragonal to rhombohedral transformation was found near 385 K. This was manifested by the development of a splitting of the (220) reflection, and a simultaneous disappearance of the (200) peak splitting. The rhombohedral lattice parameters and tilt angle (α) were calculated by fitting the (220) reflection to (220) and $(2\bar{2}0)$ peaks. The temperature dependence of α is shown in the bottom panel of Fig.4-2. Our x-ray results under zero field are in close agreement with the x-ray powder diffraction results on PMN-30%PT of Noheda *et al.*[36]

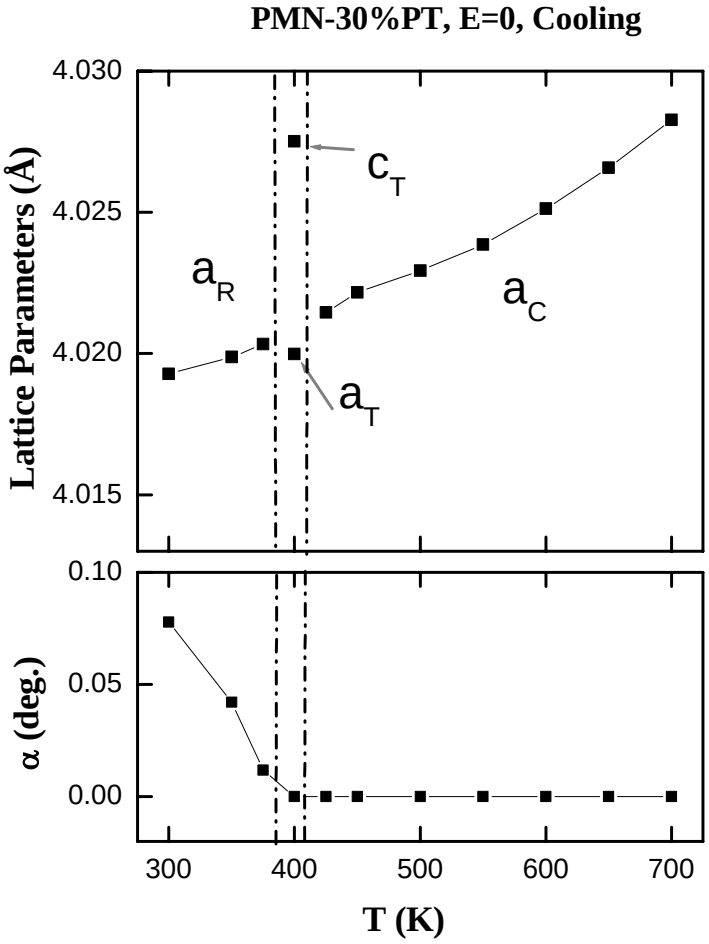

Fig.4-2. The dependence of the lattice parameters (top panel) and α (bottom panel) on temperature under zero electric field.

Phase stability in field-cooled condition

The temperature dependence of the lattice parameter was investigated under electric fields of 1 and 2 kV/cm. The specimen was first heated up to 500 K. An electric field was then applied and measurements were made on cooling. For E=1 kV/cm, a cubic to tetragonal phase transition was observed on cooling near 430 K, as determined by the starting temperature at which 2θ began decreasing (i.e., the c parameter increasing) in the (002) profile on cooling. A tetragonal to monoclinic M_C transformation was found near 365 K, and on further cooling a subsequent monoclinic M_C to monoclinic M_A transition occurred. After increasing E to 2kV/cm, the T→M_C and M_C→M_A transition temperatures decreased, and the phase stability ranges of both T and M_C phases increased.

A sketch of the unit cells and domain configurations in the reciprocal (h0l) plane for the M_A and M_C phases is shown in Fig.4-3(a) and (b), respectively. For the M_A phase, a_m and b_m lie along the pseudo-cubic $[\bar{1}\,\bar{1}\,0]$ and $[1\,\bar{1}\,0]$ directions, and the unit cell is doubled in volume with respect to the pseudo-cubic unit cell. For the M_C phase, a_m and b_m lie along the [100] and [010] directions, and the unit cell is primitive. In both cases, the angle between a_m and c_m is defined as β. Usually, monoclinic symmetry leads to a very complicated domain configuration. However, once the field is applied, the *c* axis is fixed along the field direction. The monoclinic domain configuration then consists of two *b* domains related by a 90° rotation around the *c* axis, and each of the *b* domains contains two *a* domains in which a_m forms angles of either β or 180°- β. In the $(H0L)_{cubic}$ zone, only two *a* domains can be observed for the M_A phase, as shown in Fig.4-3(a); whereas one *b* domain and two *a* domains can be observed for the M_C phase, as shown in Fig.4-3(b).

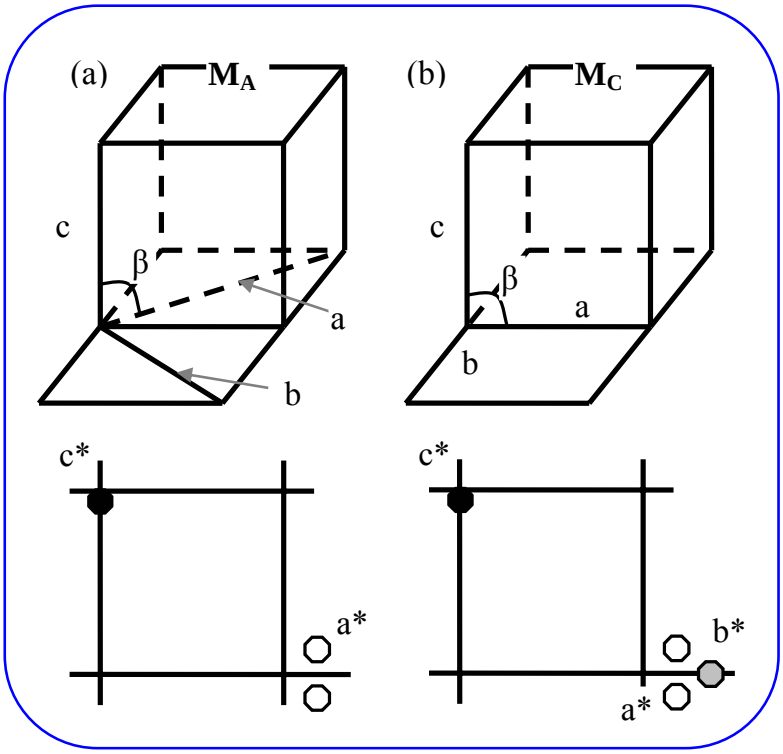

Fig.4-3. Sketch of the unit cell and domain configuration in the reciprocal (h 0 l) plane for monoclinic phases, (a) top: unit cell of M_A phase; bottom: domain configuration in reciprocal space, illustrating the two *a* domains of M_A; and (b) top: unit cell of M_C phase; bottom: domain configuration in reciprocal space, illustrating the two *a* domains (unshaded) and one *b* domain (shaded) of M_C phase.

To best illustrate the observed transformational sequence, XRD mesh scans around (200) and (220) reflections are shown in Fig.4-4 taken at temperatures of 375, 350 and 300 K. These scans were all obtained under an applied dc electrical bias of E=1 kV/cm. For T=375 K, the lattice constant c_T is elongated, whereas a_T is contracted. This indicates phase with tetragonal symmetry. For T=350 K, the (200) reflection was found to split into three peaks, consisting of two (200) peaks and a single (020) peak; whereas, the (220) reflection was found to be split into two peaks. These results indicate a phase with monoclinic M_C symmetry. On further cooling, significant changes in the mesh scans were found. For T=300 K, the (200) reflection was found to split only into two peaks, which can be attributed to the presence of two domains, whereas the (220) reflection was found to split into three peaks. This indicates a phase with monoclinic M_A symmetry. The room temperature mesh scans are consistent with those previously reported by Ye *et al.* for PMN-35%PT crystals,[34] demonstrating that the M_A phase is stable in the FC condition. Moreover, our results also give conclusive and direct evidence of an $M_C \rightarrow M_A$ transition on cooling in the FC condition for PMN-30%PT. This is different from the results for PZN-8%PT single crystals, where an $M_C \rightarrow M_A$ transition was not observed in the FC condition.[76]

Fig.4-5 shows the temperature dependence of the structural data in the FC condition for E=1 kV/cm. The top panel of this figure shows the lattice parameters, and the monoclinic tilt angle ($\beta - 90^o$) is shown in the bottom panel. The lattice constant c_T (a_T) gradually increases (decreases) with decreasing temperature. Near T=365 K, where the $T \rightarrow M_C$ transition occurs, the value of the lattice constants abruptly changes and a monoclinic tilt angle of $\beta_{Mc} - 90^o \approx 0.08^o$ forms between the (001) and (100). In the M_C

phase region, the lattice parameters a_{Mc}, b_{Mc}, c_{Mc}, and β_{Mc}. are relatively temperature independent over the range of temperatures investigated. The value of b_{Mc} can be viewed as a natural extension of the a_T lattice parameter; the value of a_{Mc} is close to the value of the cubic lattice parameter, whereas the value of c_{Mc} is notably different than either c_T, a_T, or a_c. Near T=330 K, the lattice constants and the tilt angle abruptly change, where the $M_C \rightarrow M_A$ transition occurs. Again, in the M_A phase region, it was found that lattice parameters are only weakly temperature dependent over the range of temperatures investigated.

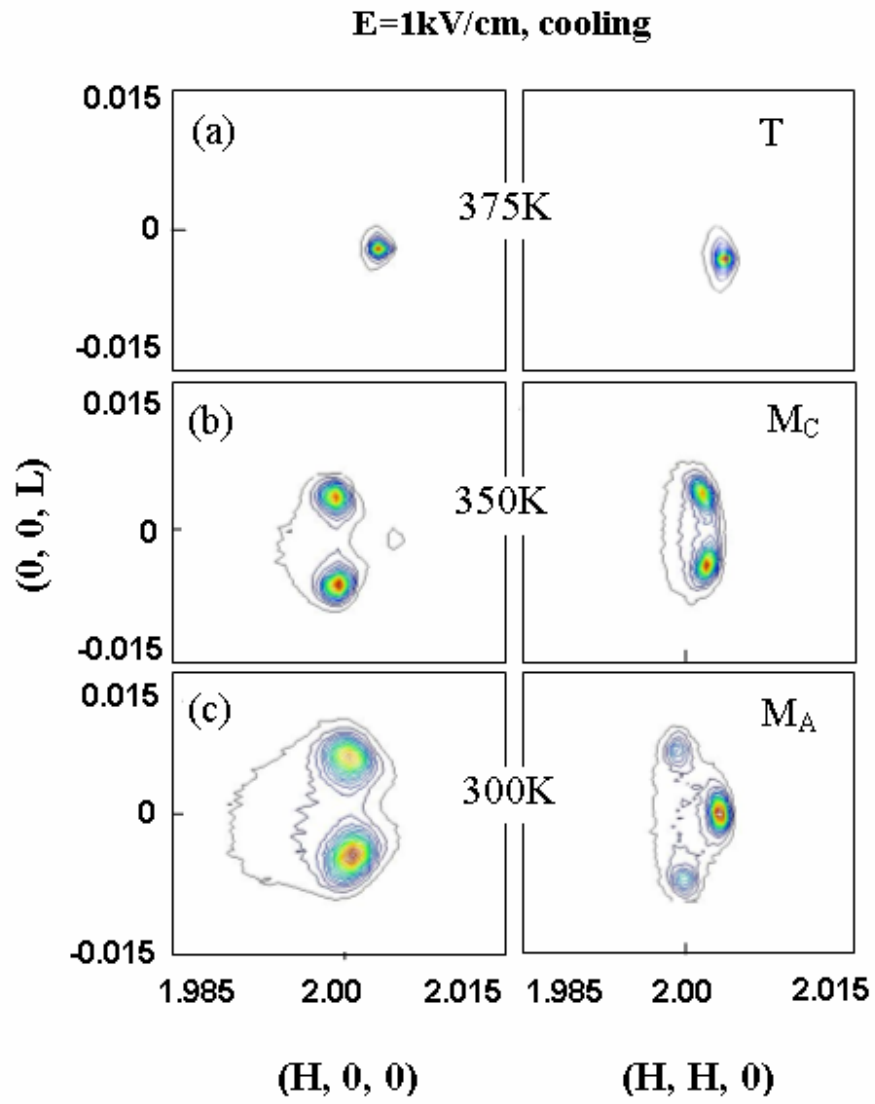

Fig.4-4. Mesh scans around the (200) and (220) reciprocal lattice positions at different temperatures in field-cooled process.

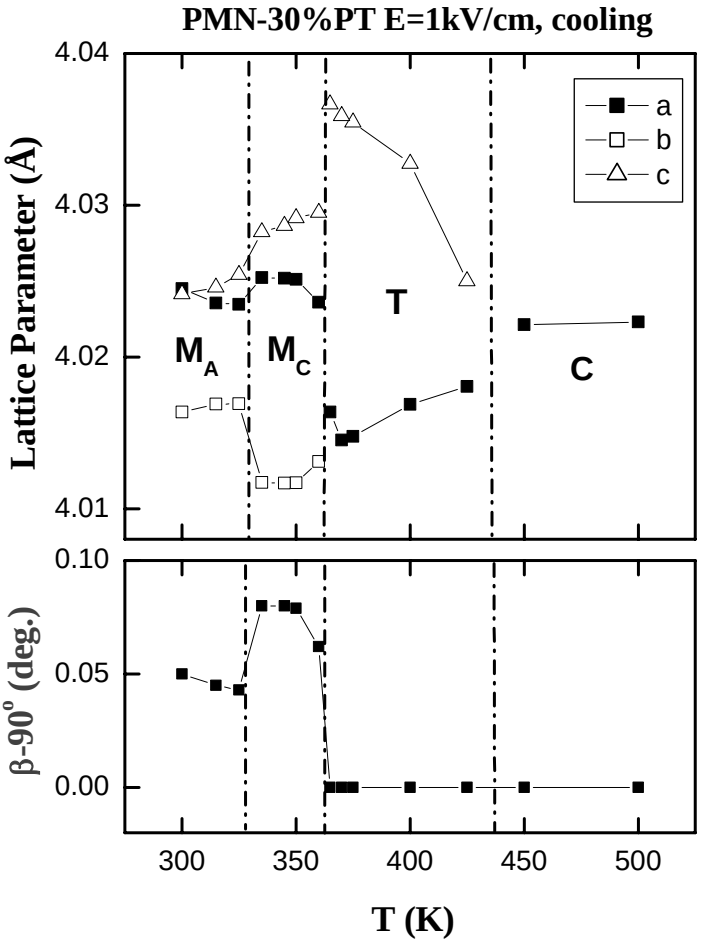

Fig.4-5. Temperature dependence of the lattice parameters (top panel), and 90°-β (bottom panel) observed in field-cooled process. For the M_A phase, the lattice parameters $a_{Ma}/\sqrt{2}$, $b_{Ma}/\sqrt{2}$ and c_{Ma} are plotted; whereas, for the M_C phase the lattice parameters a_{Mc}, b_{Mc} and c_{Mc} are plotted. Solid lines drawn through the data points are guides to the eyes.

Phase Stability at fixed temperatures with increasing E

The field dependence of the lattice structure was investigated at various temperatures. The specimen was first heated up to 550 K and then cooled under zero field. This was done at the beginning of measurements at each temperature, thus ensuring that the specimen was always properly zero-field cooled. XRD mesh scans were then performed at various dc electric biases for $0 \leq E \leq 4$ kV/cm. Both $R \rightarrow M_A$ and $M_A \rightarrow M_C$ transitions were observed with increasing E.

Mesh scans around (200) are shown in Fig.7 taken at 0, 0.5, 3 and 4kV/cm. These scans were all obtained at T=350 K. The corresponding lattice parameters were listed in Table 1. For E=0 kV/cm, a rhombohedral phase was found. Under E=0.5 kV/cm, the (200) reflection was found to be split into two peaks. This indicates an $R \rightarrow M_A$ transition with increasing E. Under E=3 kV/cm, the (200) was found to be split into three peaks, revealing a monoclinic M_C phase. And under E=4 kV/cm, the (200) was found to become to one peak, revealing a tetragonal T phase.

These changes in the mesh scans provide conclusive evidence of an $R \rightarrow M_A \rightarrow M_C \rightarrow T$ phase transition sequence with increasing E starting from the ZFC condition. The field at which the $R \rightarrow M_A$, $M_A \rightarrow M_C$ and $M_C \rightarrow T$ transitions occur varies with temperature, and is summarized in the *E-T* diagram of Fig.4-1(b). Upon removal of the field, the R phase does not recover, but instead a monoclinic phase appears. For T<350 K, the M_A phase is recovered; whereas for T>350 K, the M_C phase is recovered. Thus, the M_A phase dominates the *E-T* diagram. This is different from the previous results for PZN-8%PT, where the M_C phase recovers after removal of the field, instead of the M_A phase.[76]

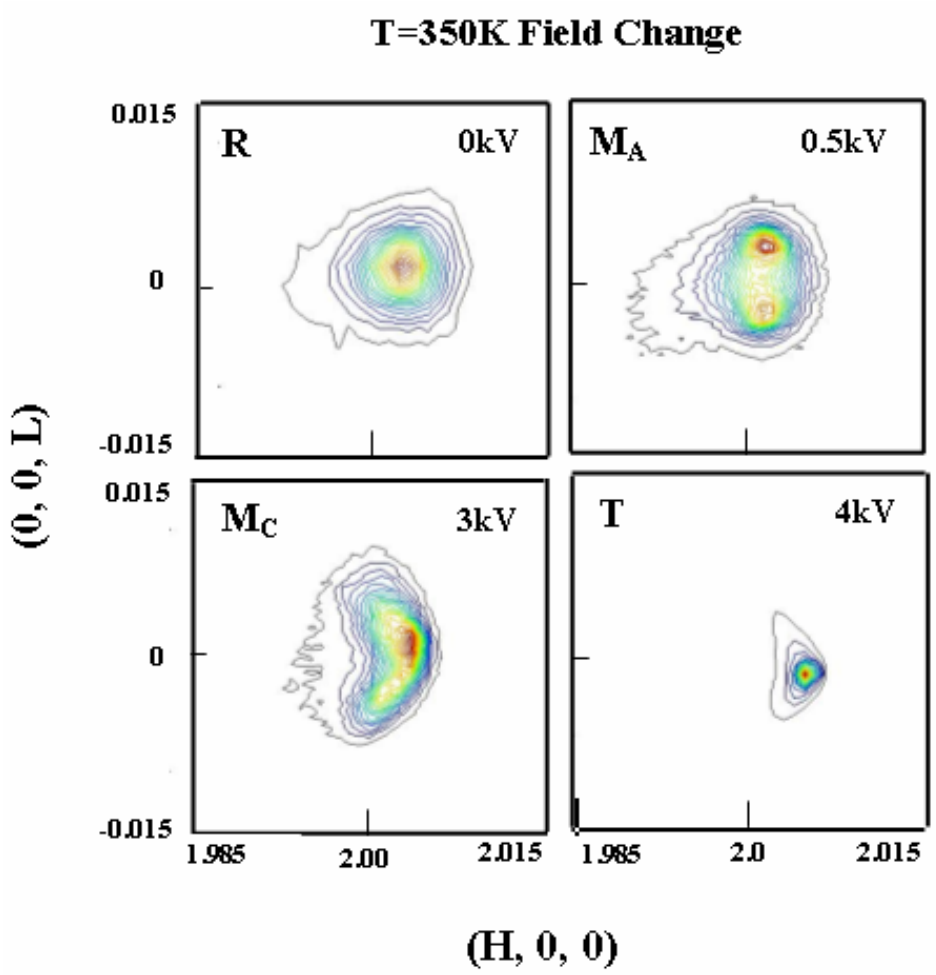

Fig.4-6. (200) mesh scan at 350K with increasing field, which clearly shows a sequential phase transition from R→M_A→M_C→T.

Table 4-1. Lattice parameter for the PMN-30%PT at 350K with increasing electric filed, measured by XRD. Errors = $\pm$0.002Å.

	a (Å)	b (Å)	α(=γ) (°)	β (°)	Phase
ZFC from 550K, E=0	4.020				R
E=0.5kV/cm	4.023		90	90.08	M_A
E=2kV/cm	4.019	4.014	90	90.09	M_C
E=4kV/cm	4.015	4.015	90	90	T

Table 4-2. Lattice parameters of PMN-30%PT under zero-field, measured by neutron scattering. Errors= $\pm$0.001Å

T (K)	Phase	a (Å)	b (Å)	c(Å)	α(=γ) (°)	β (°)
600	C	4.022	4.022	4.022	90	90
550	C	4.020	4.020	4.020	90	90
450	C	4.019	4.019	4.019	90	90
400	T	4.017	4.017	4.023	90	90
350	R	4.019	4.019	4.019	89.96	89.96
300	R	4.019	4.019	4.019	89.91	89.91
200	R	4.018	4.018	4.018	89.87	89.87
100	R	4.017	4.017	4.017	89.84	89.84

4.2.2 Neutron scattering investigations

Neutron scattering investigations were also performed in the zero-field-cooled state. The crystal was first heated up to 600 K, where again it was confirmed that the structure was cubic. Measurements of both (220) and (002) reflections were then made on cooling between 600K and 50K. A cubic to tetragonal phase transition is observed near 410 K, and confirmed by the peak splitting of the (002) reflection, similar to that found by XRD. A tetragonal to rhombohedral phase transition is observed near 385 K, as evidenced by the disappearance of the (002) splitting, and the development of a (220) splitting. The rhombohedral phase persists down to 50 K.

Fig.4-7 shows (220) scans taken at 500K and 100K. The single peak at 500K confirms that the structure is cubic, while the splitting of the (220) is clearly evident in the low temperature rhombohedral phase. In addition, a dramatic change in the line width was found on cooling. The line width was nearly an order of magnitude broader in the rhombohedral phase, relative to that in the cubic phase.

By fitting the (002) reflection with a double Gaussian function, we obtained the tetragonal lattice constants c_T and a_T. The lattice parameter and tilt angle (α) of the rhombohedral phase were calculated by fitting the (220) reflection to (220) and ($2\bar{2}0$) peaks. A summary of the temperature dependence of the lattice parameters is presented in Table 2. The neutron results clearly show that the rhombohedral phase is stable at room temperature, in agreement with our XRD studies and previous investigations by Noheda *et al.*[36]

Mesh scans of a poled PMN-30%PT single crystal were also obtained by neutron scattering. A (200) peak splitting along the transverse direction was found, as can be seen

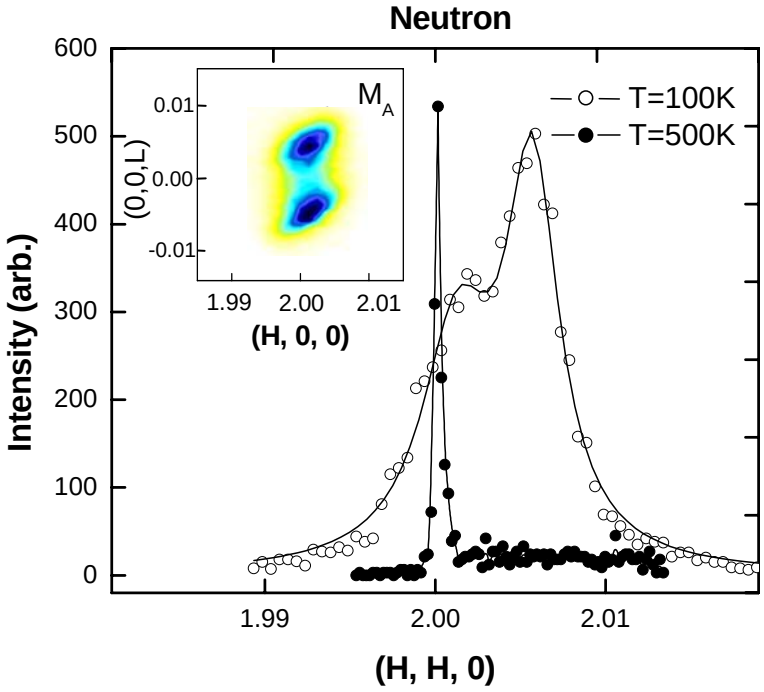

Fig.4-7. Neutron (220) profiles for PMN-30%PT. The sample was cooled under E=0. The solid lines are fits described in the text. The inset shows a neutron intensity contour around the pseudo-cubic (200) reflection in the H0L zone at 300K, which confirms the existence of the M_A phase in the FC condition. These data were all taken using a perfect crystal Ge (004) analyzer[17].

in the inset of Fig.4-7. The (200) splitting can be attributed to two *a* domains. This neutron mesh scan is nearly identical to the XRD mesh scan shown in Fig.4-4. The neutron mesh scan shows that the M_A phase is stable in the bulk of the crystal.

4.2.3. Discussion and summary

Our results for PMN-30%PT in the ZFC condition demonstrate a phase transformational sequence of C→T→R with decreasing temperature (T_c≈405K). The results are in agreement with the phase diagram given in Fig.2-1, which provides a confirmation for the composition of the crystal. This is important to know for sure, as if x had been slightly higher, M_c could have been the stable ground state, rather than R.

The stability of the M_A phase

With decreasing temperature under a constant applied field (i.e., in the FC condition), we find that PMN-30%PT undergoes the phase transformational sequence C→T→M_C→M_A. This sequence is similar to that observed in PZN-8%PT,[76] except that our x-ray and neutron investigations reveal an M_C→M_A transition with decreasing temperature, which was not found for PZN-8%PT. Moreover, with increasing field at fixed temperature starting from the ZFC condition, we find that PMN-30%PT exhibits the phase transformational sequence R→M_A→M_C→T. The R→M_A transition is irreversible upon removal of the field, whereas the M_A→M_C transition is reversible. Similar studies of PMN-25%PT (data not shown) also indicate that the M_A phase is stable at room temperature in the after-poled condition. Clearly, compared with the MPB compositions of PZN-x%PT, the M_A phase dominates the *E-T* diagram of PMN-x%PT, and not the M_C

phase. Ohwada *et al.* explained the M_C phase in PZN-8%PT by a hidden orthorhombic symmetry, located on the T-M_C-O polarization rotational pathway.[76] However, more thought is required to explain the reversibility of the $M_C \rightarrow M_A$ transition in PMN-x%PT after removal of the field, since the M_C phase is currently believed to be the ground state at the MPB.

Recent investigations by Singh *et al.* on polycrystalline PMN-x%PT for $0.27 \leq x \leq 0.30$ have reported a monoclinic M_B phase at room temperature.[71] In the M_B phase, the polarization would be constrained to the $(100)_c$ plane, and there would be two *a* domains in the reciprocal (hk0) plane where the lattice parameters fulfill $a_{Mb} > c_{Mb}$. Our investigations have failed to find an M_B phase, either in the ZFC condition (where we found the R phase) or in the FC condition (where we found two *a* domains with $a_{Mb} < c_{Mb}$, i.e., the M_A phase). However, recent investigations by Viehland and Li have indicated that the M_B phase can be induced *only* by an electric field applied along $(011)_c$, where the M_A phase is recovered on removal of E.[72]

Diffuse nature of phase transformational sequence

The *E-T* diagrams in Fig.4-12 show that the temperature stability range of the M_A, M_C, and T phases is significantly increased by the application of an electric field. This can be further noted by comparisons of the lattice parameter data for the ZFC state in Fig.4-2 with that for the FC state (E=1 kV/cm) in Fig.4-4.

We performed dielectric constant measurements under the same temperature and field conditions as that for the ZFC and FC lattice parameter data. Fig.4-13 shows the dielectric constant as a function of temperature for (a) E=0 kV/cm on cooling, and (b) E=1 kV/cm on cooling. The dielectric response in both cases is a single, broad featureless

peak, which is typical of a diffuse phase transition. The temperature of the dielectric constant maximum (T_{max}) did *not* change between the ZFC and FC measurements – T_{max} is ~405K in both cases. In this regard, the dielectric constant data reveal a notable difference with respect to the corresponding lattice parameters. Previous studies of PZN-8%PT by Ohwada *et al.* have shown a similar large change of the C→T boundary with increasing E in the *E-T* diagrams;[76] in addition, recent dielectric investigations of PMN-30%PT have shown a field independence of T_{max},[88] similar to that shown in Fig.4-8.

One would expect that the changes in the lattice parameters would occur at temperatures below T_{max}. This is required either for a 1st or 2nd order transition. However, in the FC state, our data show that a tetragonal splitting develops at $T>T_{max}$. In diffuse transitions, local polar regions are believed to have transition temperatures notably greater than that of the dielectric maximum.[89] According to the theory of diffuse transitions, the prototypic cubic and low temperature ferroelectric phases coexist over a broad temperature range, where the relative volume fractions of the coexisting phases change with temperature. However, our structural investigations demonstrate a single phase tetragonal region over the temperature range of $365<T<430$K, even though the observed T_{max} from the dielectric constant was ~405K.

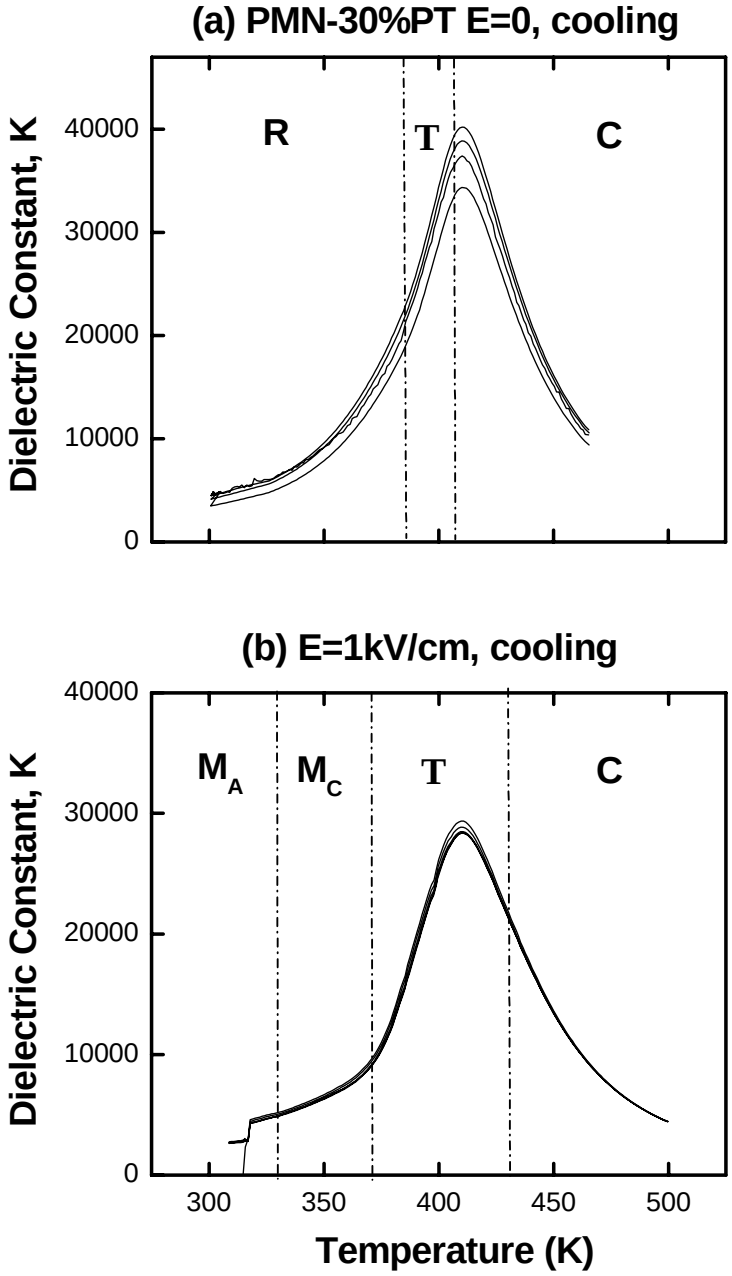

Fig.4-8. Temperature dependence of dielectric constant of PMN-30%PT PT (a) zero field cooled at E=0; and (b) field cooled at E=1 kV/cm. The dashed lines indicate the phase range determined by XRD studies.

Indications of non-conventionality were also found in the $FE_{Ma} \rightarrow FE_{Mc}$ transition. It is important to first remind ourselves that the M_c and M_a phases do not have subgroup relationships between the symmetries of their point groups. Glazer has recently noted the relevance of this fact to MPB transitions in ferroelectrics.[90] Thus, in a displacive transformation, originating from an m3m prototypic symmetry, the $FE_{Mc} \rightarrow FE_{Ma}$ transition *is required* to be first order. A common way to determine the order of a ferroelectric transition is by a Curie-Weiss plot of the dielectric constant. Fig.4-9 shows the Curie-Weiss plot, K^{-1} vs. T, during field cooling. Neither a 1st nor 2nd order transition was found at the $M_C \rightarrow M_A$ transition. Rather, the data is featureless, indicative of a diffuse $M_C \rightarrow M_A$ transition and that the transition can not be understood as a conventional displacive structural phase transition. Furthermore, a clear 2nd order transition was found during a $M_C \rightarrow M_A$ transition. However, it was found that the lattice parameters of T and M_C phase had the intrinsic relationships predicted by the adaptive theory. Thus the $T \rightarrow M$ transition was believed an atomic level domain rearrangement instead of a true phase transition. However, it is still unknown whether domain rearrangement can produce dielectric constant peak or not.

In conclusion, we have established that the phase transformational sequence of PMN-30%PT is (i) $C \rightarrow T \rightarrow M_C \rightarrow M_A$ on cooling in the FC condition; and (ii) $R \rightarrow M_A \rightarrow M_C \rightarrow T$ with increasing E at constant temperature starting from a ZFC condition. The $R \rightarrow M_A$ transition is irreversible, but the $M_A \rightarrow M_C$ transition is reversible upon removal of the electric field. As a consequence M_A is the dominant phase for $T<T_c$ in the *E-T* diagram. Evidence is also given that the $FE_{Ma} \rightarrow FE_{Mc}$ is not 1st order, but rather diffusive.

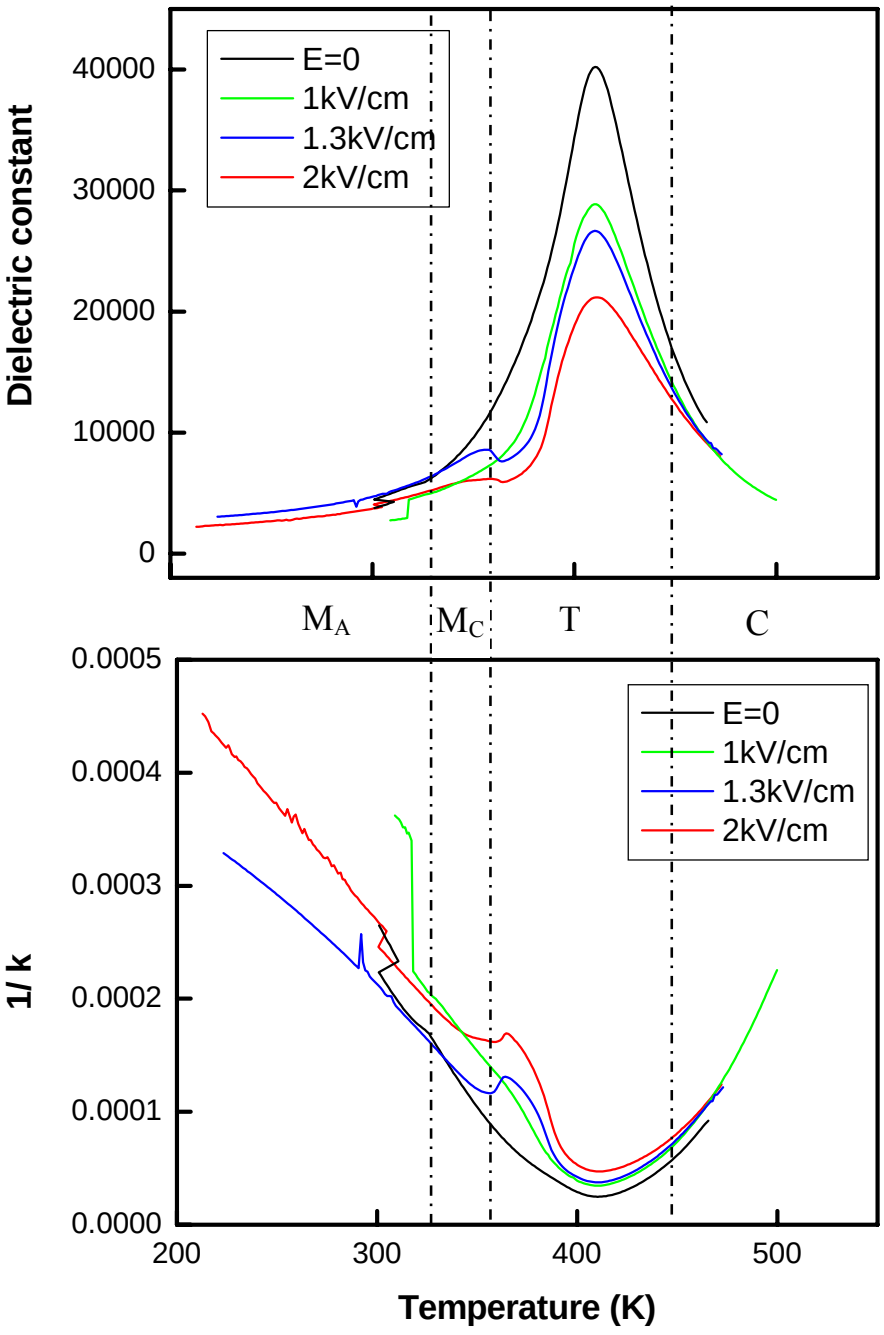

Fig.4-9. Temperature dependence of dielectric constant of PMN-30%PT during field cooling at a frequency of 100kHz, (a) k vs. T plot and (b) Curie-Weiss plot. The dashed lines indicate the phase range determined by XRD studies under E=2kV/cm.

4.3 Domain hierarchy in PMN-x%PT crystals

4.3.1 Domain evolution with various compositions

First, we illustrate changes in the PFM (real-space) images for unpoled (001)-oriented PMN-x%PT crystals with various values of x between 10 and 40%, as given in Fig.4-10. Polar nanoregions (PNRs) were found for PMN-10%PT, which were quite irregular in morphology and distribution. The average PNR size was small, close to the tip's resolution limit (~40nm). With increasing PT content to 20%, the density of PNRs increased, and some limited assembly into regular patterns observed. With increasing x to 30%, the average size of the PNRs continued to increase, and their distribution became increasingly regular. For x=35%, self-assembly of PNR into long and thin <110>-oriented domain striations was apparent. These <110> striations subsequently assembled into 90^o macro-domain plates that were aligned along the <010>. Finally, for PMN-40%PT, only 90^o micron-sized tetragonal domains with a <100> preferred orientation were found, typical of a ferroelectric tetragonal phase.

Next in Fig.4-11, we show the FFT (reciprocal space) images that correspond to the domain structures in the respective parts of Fig.4-10, where π/λ_x and π/λ_y are the domain wave-vectors along the x- and y- directions. For PMN-10%PT, the average value of π/λ_x was quite large, reflecting small average domain sizes (40nm). The intensity distribution of the FFT image resembled a halo that was very diffuse and symmetric about the x- and y-axes. The halo feature shows that there is no preferred crystallographic orientation of PNR, and the diffuseness reveals the presence of a broad distribution in PNR sizes. Accordingly, the PNRs are independent of each other, and essentially are not stress accommodating to each other. It also can not be ruled out that weak contact forces

with the SiN probe-tip might alter the PNR state at the crystal surface, as it is presumably quite fragile. With increasing x to 20%, the FFT images remained broad, diffuse and symmetric along both x- and y-axes. Accordingly, both PMN-20%PT and PMN-10%PT do not have any significant degree of geometrical organization of their PNRs along any preferred crystallographic direction – they are insensitive to domain engineering.

Upon increment of PT-content from 30<x<40%, significant changes in the FFT images were observed. For x=30%, the value of the average domain size was increased to λ=340nm. In addition, an elongation of the intensity distribution within the FFT image was found along the <110>, indicating some self-organization of PNRs into longer-scale domain features that are partially stress accommodated. However, for x=35%, a significant degree of crystallographic regularity in the domain features was found along <110>, as evidenced by the sharp splitting of the FFT intensity distribution about this direction. FFT analysis yielded an average domain width and length of λ_y~300nm and λ_x~5000nm, respectively. This significant enhancement in domain self-organization indicates that stress accommodation along the <110> becomes increasingly important in the vicinity of the MPB. Finally, on increment of the PT-content to x=40%, the FFT image revealed strict domain alignment along <100> – a signature of a tetragonal ferroelectric phase. The average domain length was DC (~10 μm in this image, but 40 μm using a larger scan area) and the average width was ~2 μm. The large domain size and strong <100> alignment shows that the tetragonal phase is fully formed. [Also see reference 91]

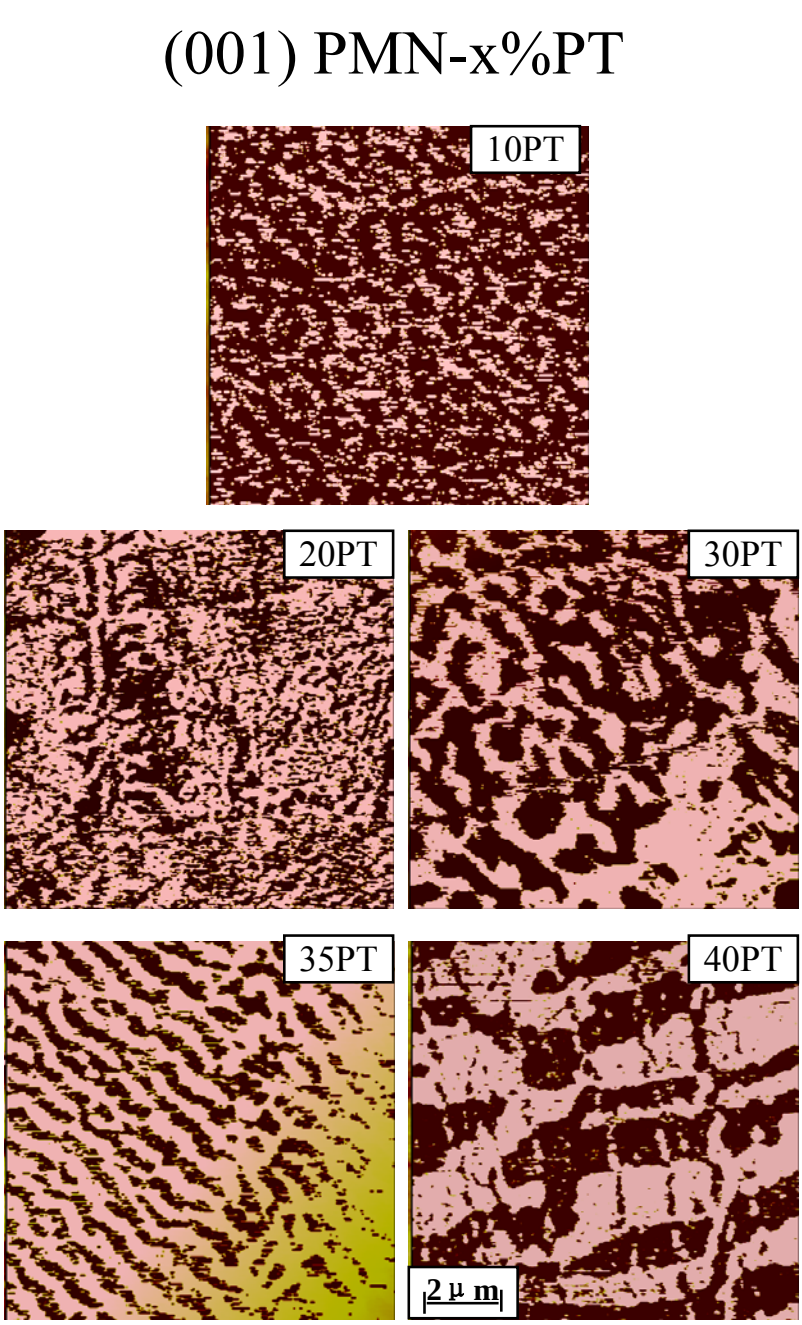

Fig.4-10. Piezoresponse force images for various (001)-oriented PMN-x%PT crystals.

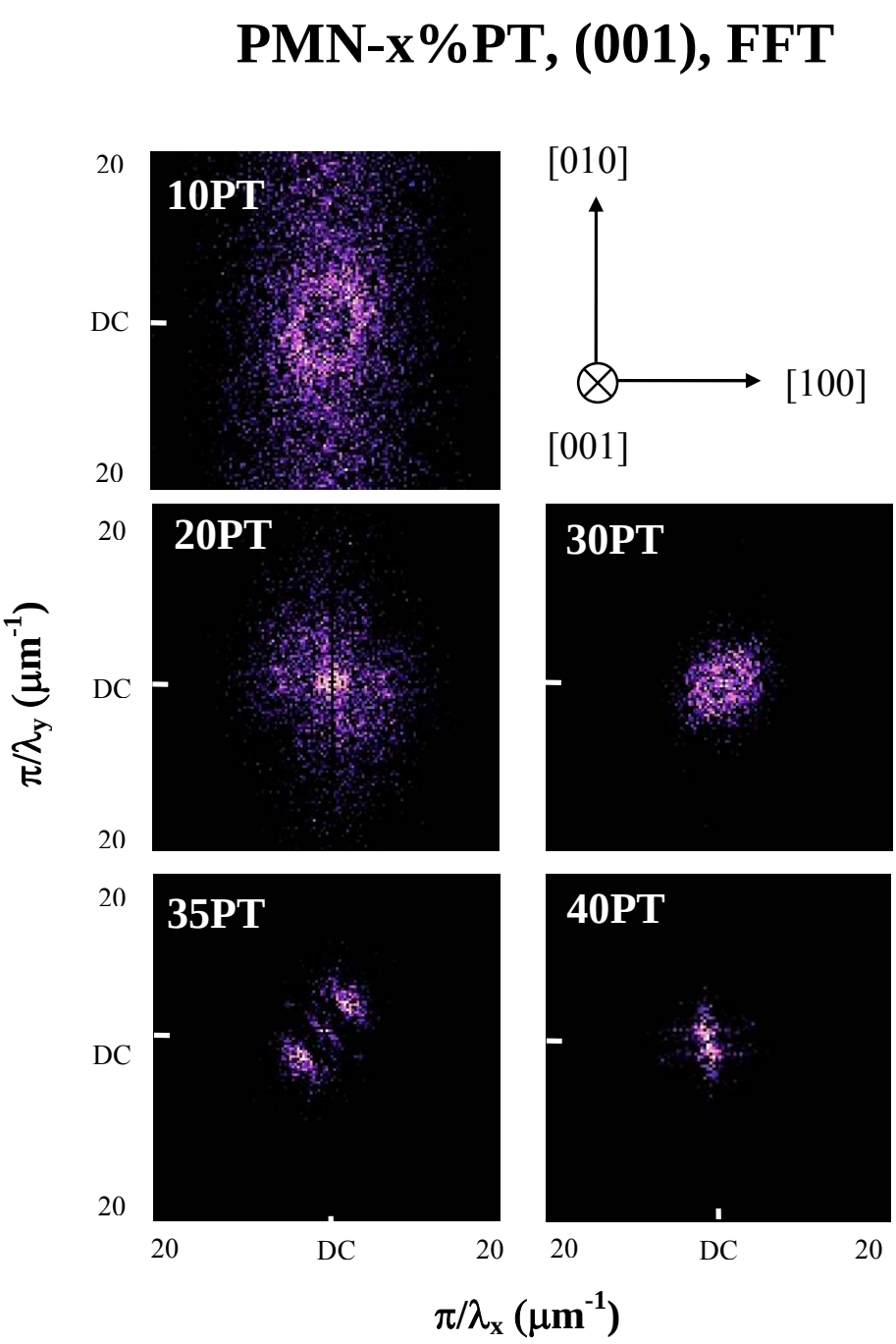

Fig.4-11. Fast Fourier Transformation of images in Fig.4-10.

4.3.2 Characterization of domain structures over various length scales

For (001)-oriented PMN-10%PT, which is of the X phase,[63] POM revealed a featureless image. However, the corresponding PFM image, shown above, revealed the presence of PND. Comparison of these results show that phase X consists of PND, which do not self-assemble into macro-domain plates. The PND are essentially non-stress accommodating, and thus their boundaries are not restricted by elastic compatibility. A similar domain structure was observed for PMN-20%PT. However, with increasing PT concentration, more regular domain patterns became evident, as to be shown below, indicating an importance of stress accommodation.

Fig.4-12 shows POM and PFM images taken over various lengths scales for (001)-oriented PMN-30%PT, which is of the R phase.[36] Part (a) shows a POM image that reveals rhombohedral macrodomain plates twinned close to a <110>, which have a spindle-like morphology. The macrodomain widths are ~1 μm and their lengths are ~20 μm. Inside of the macrodomain plates, miniature 'wavy' domains oriented close to a <110> were found, as shown in the PFM image of Part (b). A higher resolution PFM image, shown in Part (c), illustrates that the domain boundaries are rough, and that there are irregularities of similar size to PND internal to the 'wavy' domains. In Part (d), cross-sectional line analysis along the [110] direction revealed an average domain spacing of ~0.34μm, where the phase difference fluctuated pronouncedly as a function of distance.

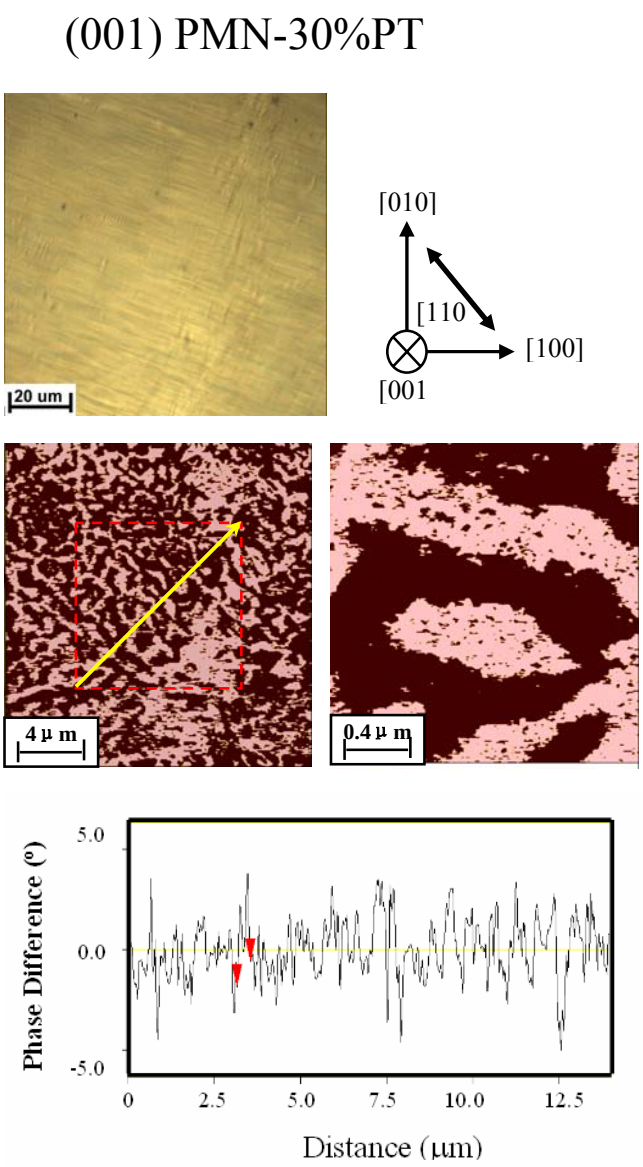

Fig.4-12. Domain hierarchy of (001)-orientated PMN-30%PT in R phase. (a) Spindle-like macrodomain plates with a <110> type preferred orientation by POM; (b) wave-like self-assembled domains by PFM; (c) high resolution PFM image illustrating non-smooth domain boundaries and irregularity; and (d) cross-sectional line analysis normal to [110].

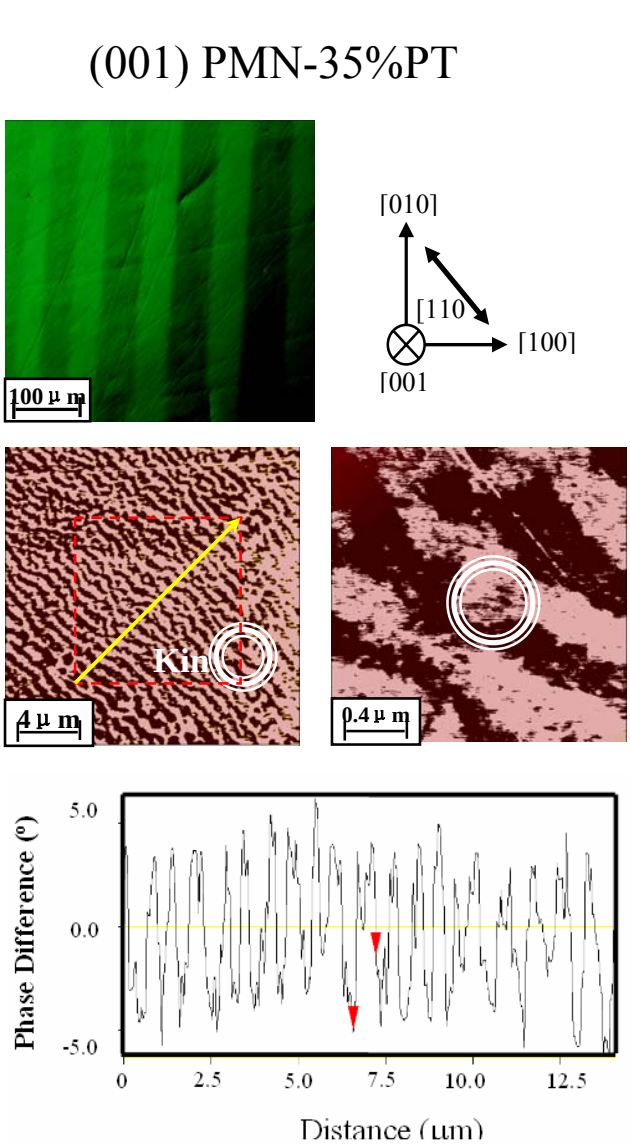

Fig.4-13. Domain hierarchy of (001)-orientated PMN-35%PT in Mc phase. (a) Stripe-like macrodomain plates with a [010] type preferred orientation by POM; (b) micro domain striations with a <110> type preferred orientation by PFM, kinks are illustrated at boundaries; (c) high resolution PFM image, illustrating non-smooth domain boundaries and irregularities; and (d) cross-sectional line analysis normal to [110].

Fig.4-13 shows the domain hierarchy for (001)-orientated PMN-35%PT, which is of the M_c phase.[36] Broad stripe-like domains oriented close to a <001> direction were found by POM, as shown in Part (a). The average domain width was ~50μm. Inside the macrodomain plates, alternating domain striations oriented close to a <110> were found that had a width of <0.5μm, as shown in the PFM image of Part (b). Kinks between neighboring striations, illustrated by a circle, are 90^o twins between them. A higher resolution PFM image is given in Part (c). The striations can be seen to be rough and non-uniform in thickness, having internal irregularities of similar size to PND. Cross-sectional line analysis, shown in Part (d), yielded an average domain spacing of ~0.35 μm. In addition, the analysis indicated pronounced contrast variation within a domain, as illustrated by the peaks between two triangles, which may be sub-domain structures corresponding to PNDs in Part (c).

The domain hierarchy of PMN-40%PT is shown in Fig.4-14, which is of the T phase.[36] Stripe-like tetragonal domains oriented close to a <001> are apparent in the POM image of Part (a). These macrodomain plates are similar to those of PMN-35%PT, except for thin 90^o fringes, indicative of a larger transformation stress. Internal to the macrodomains, fine broken domain striations were found that were oriented close to a <001>, as can be seen in the PFM image of Part (b). Their lengths varied from several to ~30μm. It is relevant to note that these macrodomains and internal striations were both oriented along the same direction, unlike that for PMN-35%PT. Part (c) shows a higher resolution PFM image, revealing that the striations are quite rough. Cross-sectional analysis taken along the [010], shown in Part (d), reveals an average domain spacing of ~2 μm that fluctuated notably, possibly reflecting the domain heterogeneities in Part (c).

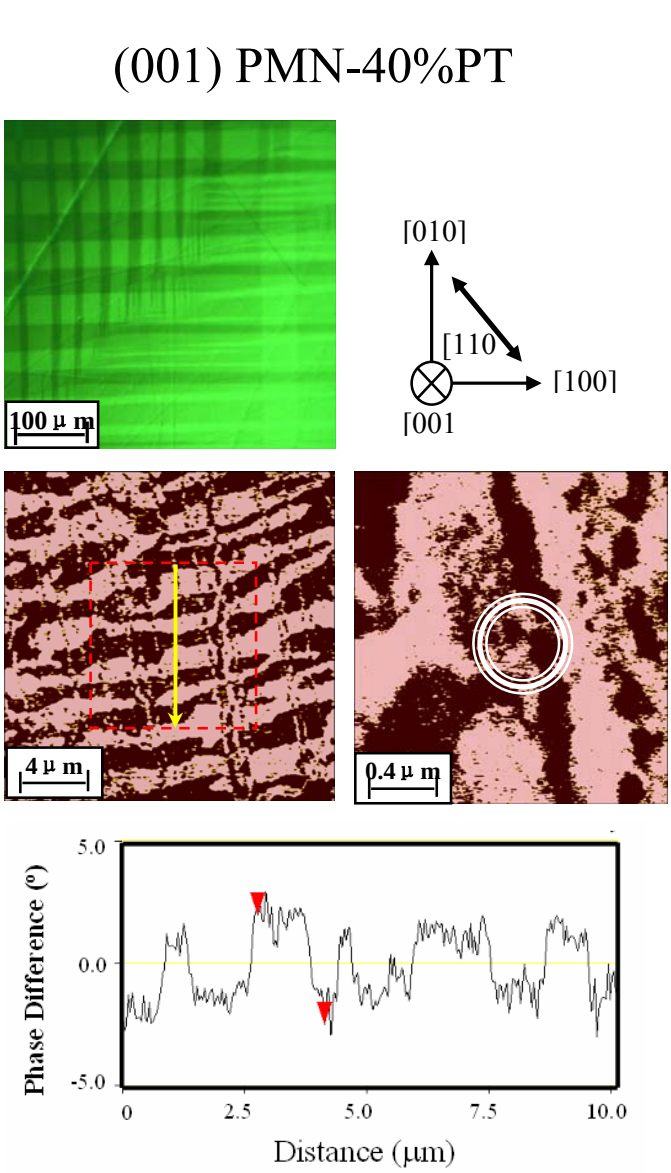

Fig.4-14. Domain hierarchy of (001)-orientated PMN-40%PT in T phase. (a) Stripe-like macrodomain plates with a <100> type preferred orientation by POM; (b) <100> orientated stripe-like micro domains with fibrous sub-domain structures by PFM; (c) high resolution PFM image, illustrating domain irregularity; and (d) cross-sectional line analysis normal to [100].

4.3.3 Evolution from PNR to macro domain

The results above are very helpful to explain the [002] line scans of PMN-x%PT by XRD, as shown in Fig.4-15. For 10%PT, although there are many PNRs embedded in a cubic matrix, the size of these PNRs is well below the coherence length of X-ray.[19] So a very sharp peak was observed with a FWHM (full width at half maximum) of 0.0276. For 20%PT, both the size and density of PNRs have significantly increased. The PNR should now be called as *polar nano domain* (PND) with the appearance of a bulk ferroelectric phase. XRD shows a typical signature of R phase: one peak for a {002} line scan, two peaks for {101} or {111} line scans. These PNDs are now detectable by X-ray and cause broadening of the (002) peak with a FWHM of 0.058. However, there is no clear boundary between PNR and PND or between cubic and rhombohedral phase on the phase diagram, which is actually depending on the detection wavelength.

With PT concentration increasing to 30%PT, even broader (002) peak was observed with a FWHM of 0.1200 - 4x of that of 10%PT. This is due to the high density of PND in PMN-30%PT crystal. Also, it should be noted that the (002) peak is left-asymmetric, which was found in both XRD and neutron scattering.[87] There are two possible causes for the asymmetry: stress or the appearance of a second phase. As mentioned above, all samples were annealed at 550K to remove residual stress. Since the line scan plot exhibits three splits for (110) peak, it is reasonable to state that a second phase coexists with the rhombohedral phase. However, it may be of a low volume fraction, and thus was not be resolved by mesh scans.

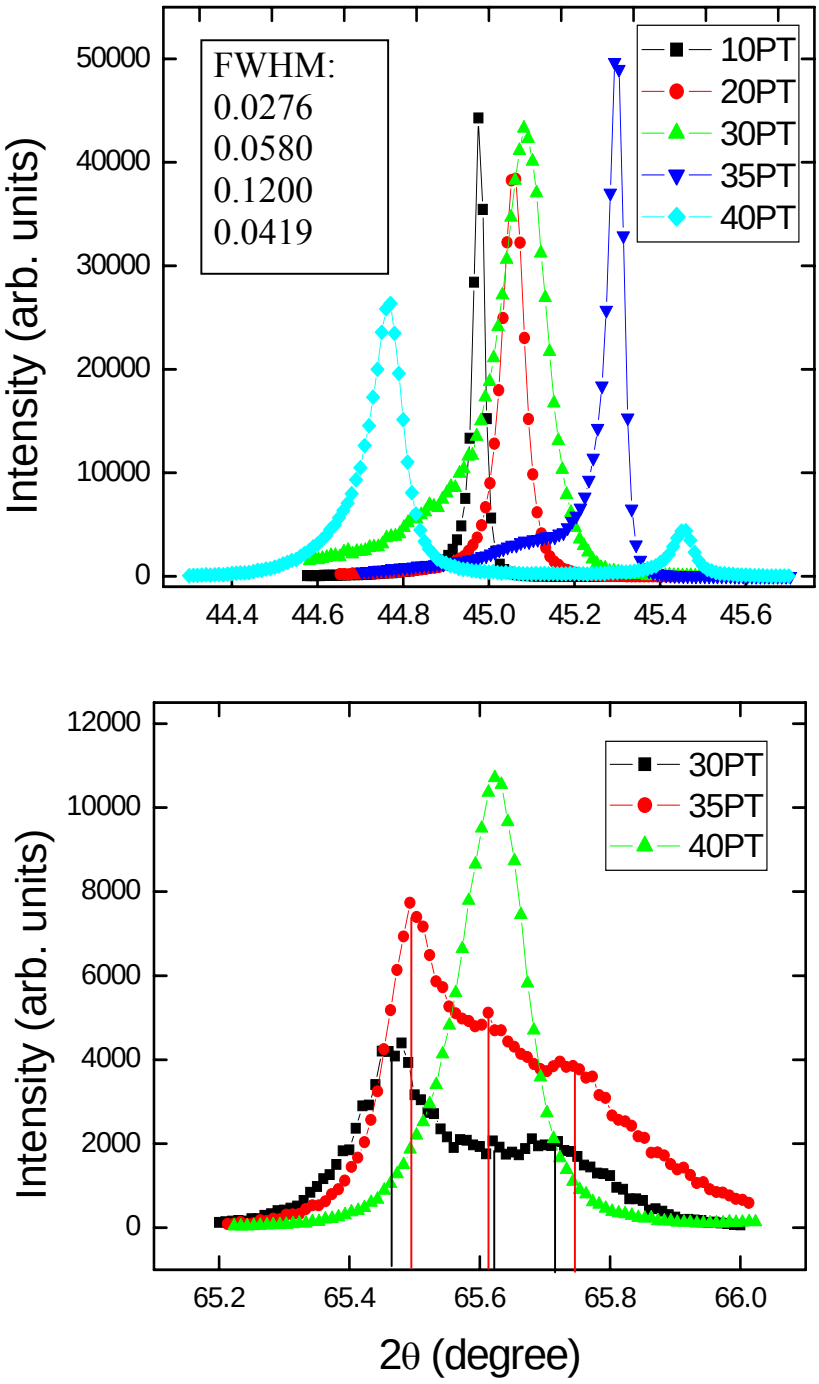

Fig.4-15. XRD of PMN-x%PT (x=10, 20, 30, 35 and 40), (a) (200) line scans; and (b) (110) line scans. Note the left asymmetric (200) peak of PMN-30%PT.

The PNDs evolve into stress-accommodated *micro domains* in PMN-35%PT with clear [110] preferred orientation. No macro twin structure was found. However, [001] oriented kinks are observed, which are the tetragonal domain boundaries observed by POM. The size of these domains are larger than the X-ray coherence length, thus a narrower peak was observed in the (200) line scan with a FWHM=0.0419. In addition, there were clearly two peaks on the (200) line scan. Noheda et al. have suggested a coexistence of M and T phases in PMN-35%PT. We thus confirmed different domain symmetries on different scale levels: a monoclinic one at the microdomain level observed by PFM and a tetragonal one at the macro domain level observed by POM.

For 40%PT, in spite of the fact that well-aligned stripe-like macro-domains were observed by POM and clear tetragonal splitting was found in the {200} line scan, small PNDs may still persist due to compositional inhomogeneity. This could contribute to broadening along the (200) and (002) peaks, where FWHM were found to be 0.0993^{o} and 0.0631^{o} respectively.

In summary, our results demonstrate (i) a domain hierarchy on various lengths scales between nano- and milli-meters for certain compositions; and (ii) evolution from PNR to macro domain by stress accommodation with increasing PT concentration, as shown in Fig.4-16. In details, phase C consists of PNR, which do not self-assemble into macrodomain plates that can be detected by X-ray or neutron beam; phase R (x=20, 30) consists of PND that begin to self-assemble into colonies close to a <110>; Phase M (x=35) consists of micron-domains, which first self-assemble into <110> striations of μm size and then <001> macrodomain plates of mm size; and phase T (x=40) consists of <001> oriented striations of μm size that still have an internal nano-scale heterogeneity.

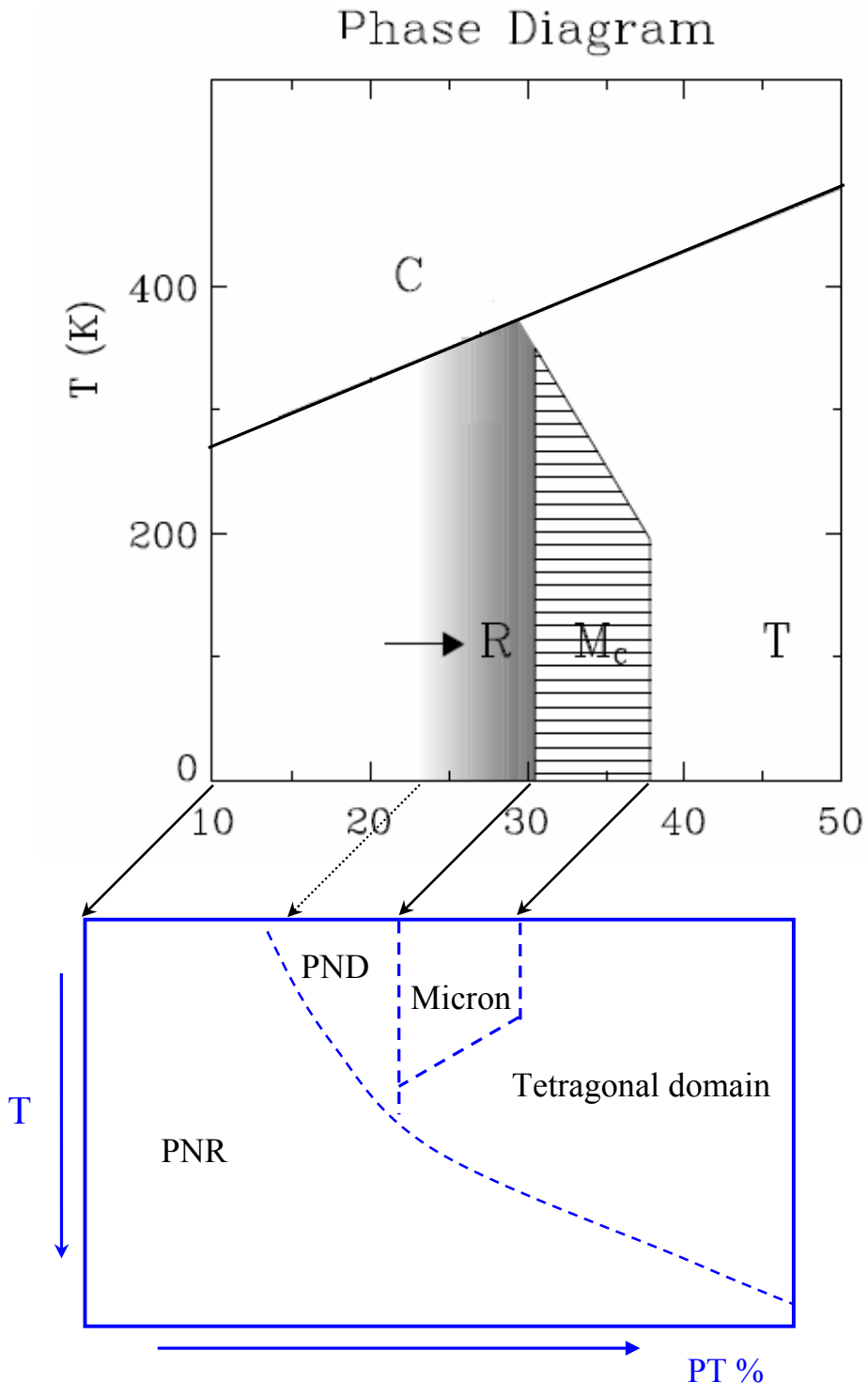

Fig.4-16. Schematic illustration of domain evolution from PNR to macrodomain plate with respect to relevant phase symmetries in PMN-x%PT crystals.

4.4 Domain configurations of after-poled PMN-x%PT

In the after-poled conditions, 20PT and 30PT change from R to M_A phases; 35PT and 40PT are still M_C and T phase, however, domain rearrangement occurs during field cooling. In the following sections, the domain structures of field-cooled (FC) PMN-x%PT crystals were investigated. [Also see reference 92]

4.4.1 Domain structures in the field-cooled condition

PMN-20%PT

Fig.4-17 shows POM and PFM images taken over various length scales for (001) PMN-20%PT in the ZFC and FC (E=6kV/cm) conditions. In the ZFC condition (see Part (a)), which is of the X phase, no larger scale domain features were found by POM. Similar POM images were obtained for the FC condition, but are not shown. However, miniature polar domains of nano-meter size (PND) were found in the PFM images, whose morphology and distribution were quite irregular, as shown in Part (b). The volume fractions of light and dark color regions, representative of different domain variants, were roughly equal. In the FC condition (see Part (c)), miniature domains of irregular shape remained present, and there was no clear evidence of significant domain growth. However, the relative volume fraction of one domain variant was strongly favored over the others, indicating an alignment of PND along an easy axis.

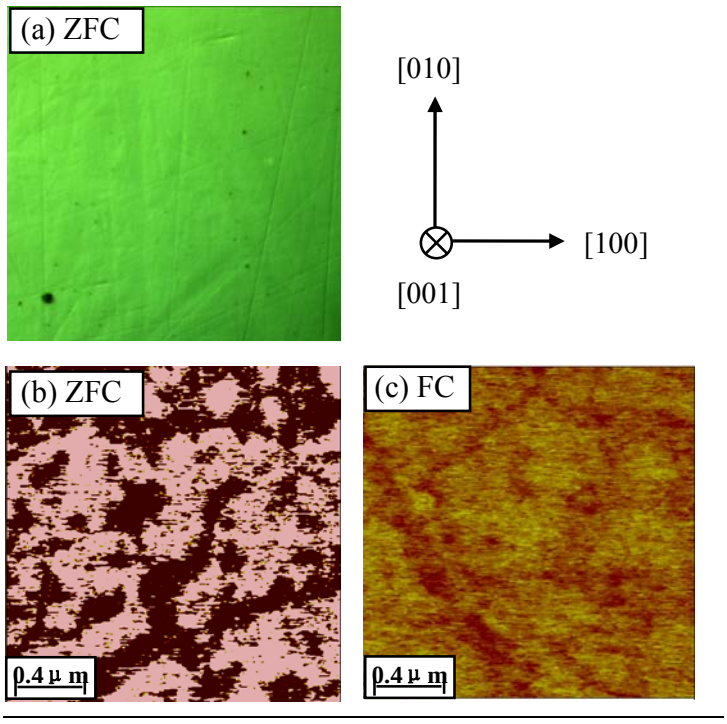

Fig.4-17. Domain hierarchy of (001)-orientated PMN-20%PT in the ZFC and FC conditions. (a) Lack of macro-domain plates in the POM image for the ZFC condition, a similar image was found for the FC condition; (b) PFM image for the ZFC condition; and (c) PFM image for the FC condition

PMN-30%PT

Fig.4-18 shows POM and PFM images taken over various lengths scales for (001) PMN-30%PT in the FC condition. The stable phase is of the M_A structure.[87] Part (a) shows a POM image that reveals tiny domains developing inside of spindle-like domains, forming at almost 90^o angles. The spindle domains are ~1 μm in width; and maintain a {110} orientation, consistent with the polarization of the M_A phase being confined to the $(1\bar{1}0)_c$ plane. The internal structure of the FC domains was probed using PFM, as shown in the image given in Part (b). Miniature polar domains were found in the PFM images, whose morphology and distribution were quite irregular. Part (c) shows a higher resolution PFM image. Comparisons of Parts (c) of Fig.4-12 and 4-18 in the ZFC and FC conditions will reveal a dramatic decrease in the size of the miniature domains on poling for PMN-30%PT. In the ZFC condition, the miniature domains demonstrate a significant degree of self-assembly, although irregularities of similar size and morphology to PND were found within the domain striations; whereas in the FC condition, self-assembly was no longer apparent on a length scale distinguishable by PFM, rather only the irregularities were apparent. Cross-sectional analysis confirmed a significant decrease in the size of the miniature domains in the FC condition (0.04 μm), relative to that of the ZFC (0.25 μm in width and microns in length).

PMN-35%PT

Fig.4-19 shows POM and PFM images taken over various lengths scales for (001) PMN-35%PT in the FC condition. The stable phase is also of the M_C structure.[35-36] Part (a) shows a POM image that reveals the presence of macrodomain plates oriented along {001} that are ~50 μm wide, which is quite similar with the POM image in ZFC

condition. The internal structure of the FC macrodomains was probed using PFM, as shown in the image given in Part (b). Part (c) shows a higher resolution PFM image. Inside the macro-plates was found alternating domain striations; however, comparisons of the higher resolution PFM images in the ZFC and FC conditions, Parts (c) of Fig.4-13 and 4-19, will clearly reveal two important differences. First, the FC domain striations were notably shorter in length, than the corresponding ZFC ones – less than one micron compared to tens of microns, although the widths were quite similar. Second, the FC domain striations were zig-zagged between {010} variants about the {110}, as indicated in Fig.4-19(c). In both the FC and ZFC conditions, internal irregularities of similar size to PND were found. Cross-sectional analysis yielded similar average domain sizes for both the FC and ZFC conditions (~0.25 μm).

PMN-40%PT

Fig.4-20(a) and (b) show POM and PFM images in the FC condition, respectively. The macrodomain plates in the PLM image can be seen to be similar to those for the ZFC condition in terms of size, an internal fibrous structure, and the presence of fringes. However, in the PFM image, comparisons of the internal fibrous structure between the ZFC and FC conditions will reveal that the {001} lamella domains are wider, longer, and more regularly spaced in the FC condition: application of E caused some to grow in a sidewise direction to the field, and others to shrink. However, inspection of the lamella domains will reveal many internal irregularities, indicating that domain growth does not occur by a coherent boundary movement, but rather by the re-organization of internal irregularities.

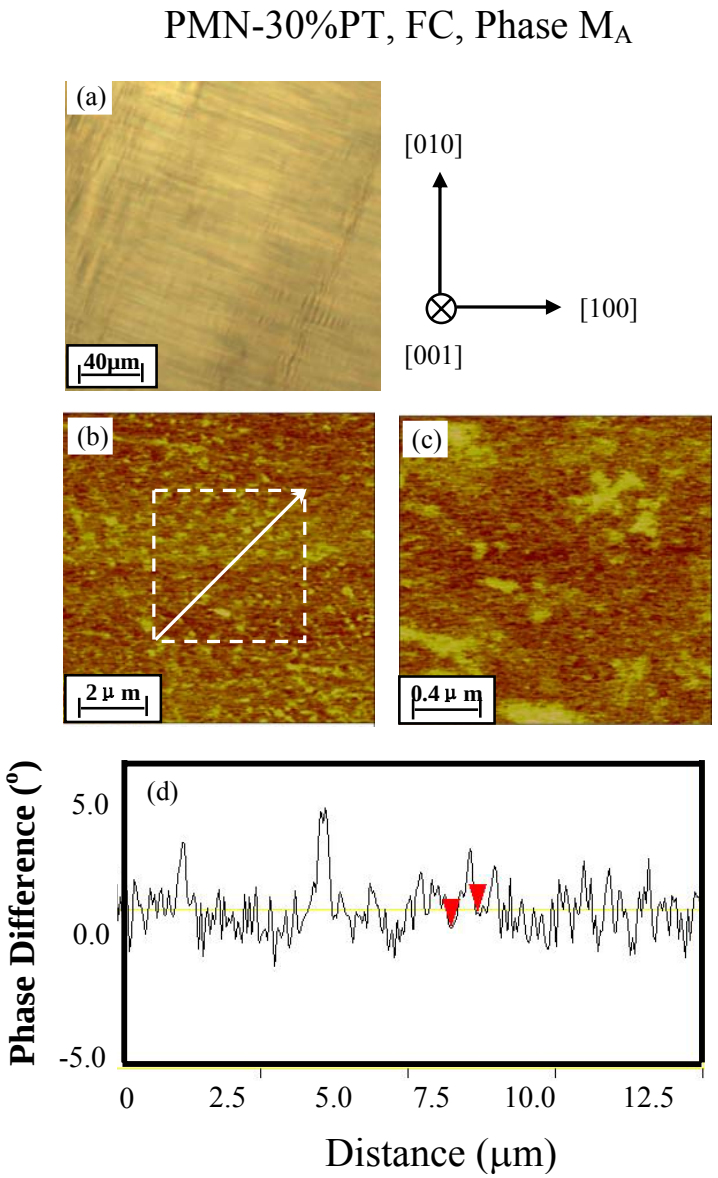

Fig.4-18. Domain hierarchy of (001)-orientated PMN-30%PT in the FC condition, which is of the M_A phase. (a) Spindle-like macro domains with <110> preferred orientation by POM; (b) identification of polar nano-domains or PND by PFM; (c) high resolution PFM image illustrating size of PND; (d) cross-sectional line analysis normal to [110].

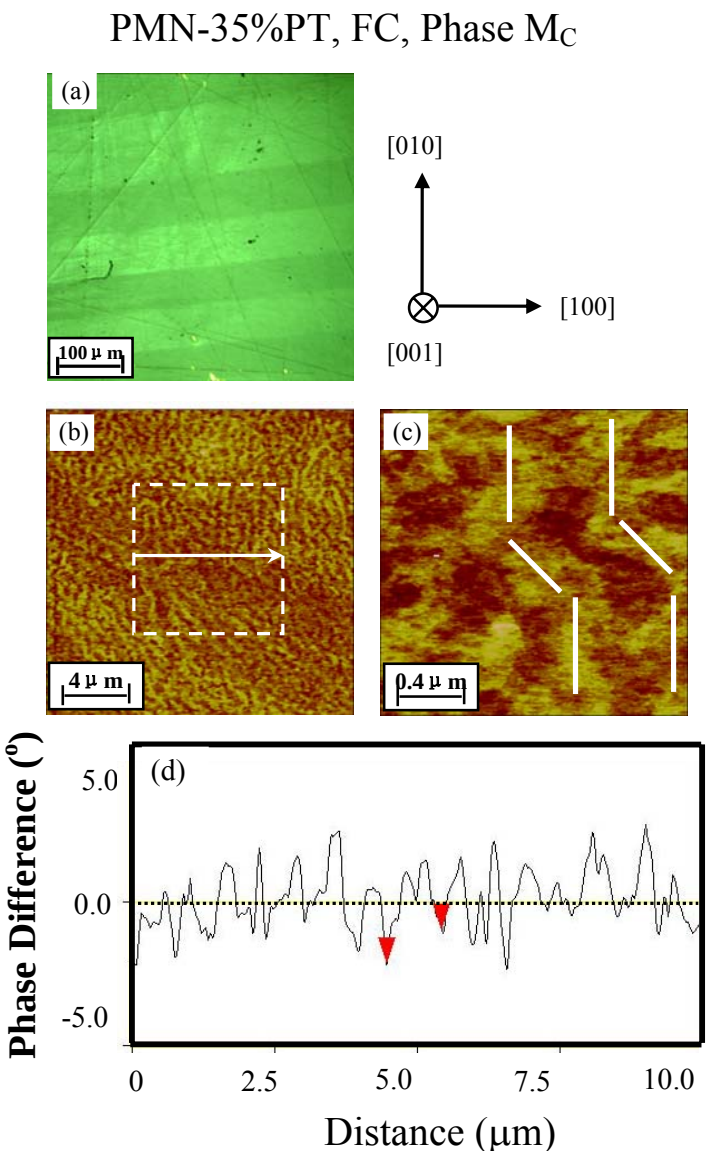

Fig.4-19. Domain hierarchy of (001)-orientated PMN-35%PT in the FC condition, which is of the M_C phase. (a) Stripe-like macro domains with [100] preferred orientation by POM; (b) domain striations with either [110] or [001] preferred orientation by PFM, which are of notably smaller length than those of the ZFC condition; (c) high resolution PFM image; (d) cross-sectional line analysis normal to [100].

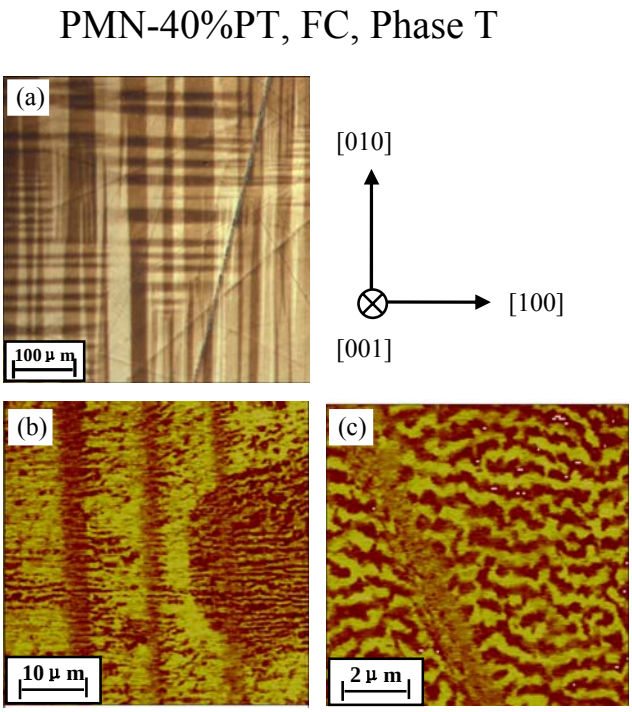

Fig.4-20. Domain hierarchy of (001)-orientated PMN-40%PT in the FC condition, which is of the T phase. (a) Stripe-like macro domains with <100> preferred orientation by POM; (b) [100]-orientated strip-like micro domains with fibrous sub-domain structures by PFM; and (c) high resolution PFM image illustrating irregularity.

4.4.2 Comparison of domain structures in the ZFC and FC conditions

Our PFM results provide important insights into the nature of the domain engineered state in PMN-x%PT crystals. The results demonstrate the presence of a domain hierarchy on various length scales, ranging from nano- to milli-meters, which depends upon the electrical history of the crystal. The findings can be summarized with respect to relevant phases.

For x=20at%, in phase X, the results show the presence of PND that do not self-assemble into macro-domain plates. The PND are essentially non-stress accommodating. The boundaries between them are not restricted by elastic compatibility. Field-cooling aligns PND, however it fails to induce the formation of normal micron-sized domains, or their assembly into macro-domain plates.

In phase R (i.e., the ZFC condition of PMN-30%PT), the PND assemble into 'wavy' domains with some preferential orientation along {110}. These 'wavy' domains then self-assemble into macrodomain plates that are oriented along {111}. However, in phase M_A (i.e., the FC condition of PMN-30%PT), the hierarchy of domain structures is notably changed, specifically resulting in a dramatic decrease in the domain size, although the macrodomain plates keep the same {110} orientation.

In phase M_C, for both the ZFC and FC conditions, the PNDs self-assemble into domain striations; however, there are important differences in the internal structure of the striations. The striations in the ZFC condition are long and preferentially oriented along only {110}; whereas those in the FC condition are more limited in spatial extent, consisting of zig-zags between {010} variants about {110}. In both the ZFC and FC conditions, the domain striations self-assemble into much larger macrodomain plates which are oriented along {001}.

Phase T (x=40%) consists of {001} oriented striations of μm size that have an internal nano-scale heterogeneity, which self-assemble into macrodomain plates of mm size oriented along a {001}. Application of E results in growth of some {001} striations at the expense of others, via re-organization of internal irregularities.

4.4.3 Origin of Domain-engineered state

A natural question to ask is what is the origin of the domain hierarchy, and subsequent changes with composition and electrical history. It is important to compare our results with conventional ferroelectric 'fingerprint' domains in $BaTiO_3$. In this case macrodomain plates have been observed, which contain internal 'fingerprint' domains. Following conventional thought, these 'fingerprint' patterns are 180^o T domains, whose distribution achieves polarization compensation; whereas the macrodomain plates are 90^o ferroelastic domains, whose distribution achieves stress accommodation. Accordingly, in this classic case, a domain hierarchy exists, consisting of (i) micron-sized 180^o ferroelectric domains oriented along {001}, which exists inside of (ii) larger 90^o ferroelastic domains, also oriented along {001}.

So what is different in PMN-x%PT crystals? First, the 'fingerprints' in PMN-x%PT crystals were oriented along {110}, for both PMN-30%PT and PMN-35%PT. Second, the "fingerprints" were apparently built from finer scale polar structures or PND – there is an additional lower end of the hierarchal scale. Third, the *'fingerprints'* were quite irregular in morphology – the 'wavy' domain boundaries indicate that random-fields disrupt the long-range polar order, partially compensating the polarization. Thus, the domain hierarchy can not be completely adjusted at each length scale in an independent manner, i.e., polarization compensation and stress accommodation occur at all stages of

the hierarchy, and not at separate length scales independent of the other. Fourth, '*fingerprints*' within macrodomain plates were found only in phases R and M_C; and not in phases X, M_A, and T. Finally, the '*fingerprints*' in PMN-x%PT crystals were very thin – the hierarchy consists of an extremely high domain wall density. In particular, the density of 'fingerprints' was extreme near the MPB: at lower PT contents domain irregularities dominated the morphology, and at higher PT contents '*fingerprints*' did not form.

Self-assembly due to Stress Accommodation in Adaptive Martensite

Alternatively, let us consider the conventional ferroelastic microstructure. On a fine length scale, alternating layers of twin-related domains exist, which also form a 'fingerprint' pattern, as shown in Fig.4-21.[93] The twin boundaries of the 'fingerprints' are not restricted to be 180^o. Self-assembly is achieved by varying the relative domain layer thicknesses of the 'fingerprints', which are adjusted to establish the macroscopic invariance of the habit plane,[94-95] and in so-doing eliminating the long-range stress fields generated by crystal lattice misfits.[96-98] This requires the domain-averaged stress-free transformation strain of each plate to be an Invariant Plane Strain (IPS), where the invariant plane is parallel to the habit plane. Stress-accommodating alternating domain layers (or 'fingerprints') typical of ferroelastics will occur for any displacive transformation, which can form a domain-averaged transformation strain that is an IPS – including ferroelectrics.

Recently, a theory for the conformal miniaturization of the self-assembled domain topology was developed.[42-44] This theory considered the case of abnormally small domain wall energy, or extreme domain wall density. The theory was applied to ferroelastics and ferroelectrics containing miniaturized domains – in particular to PMN- x%PT and

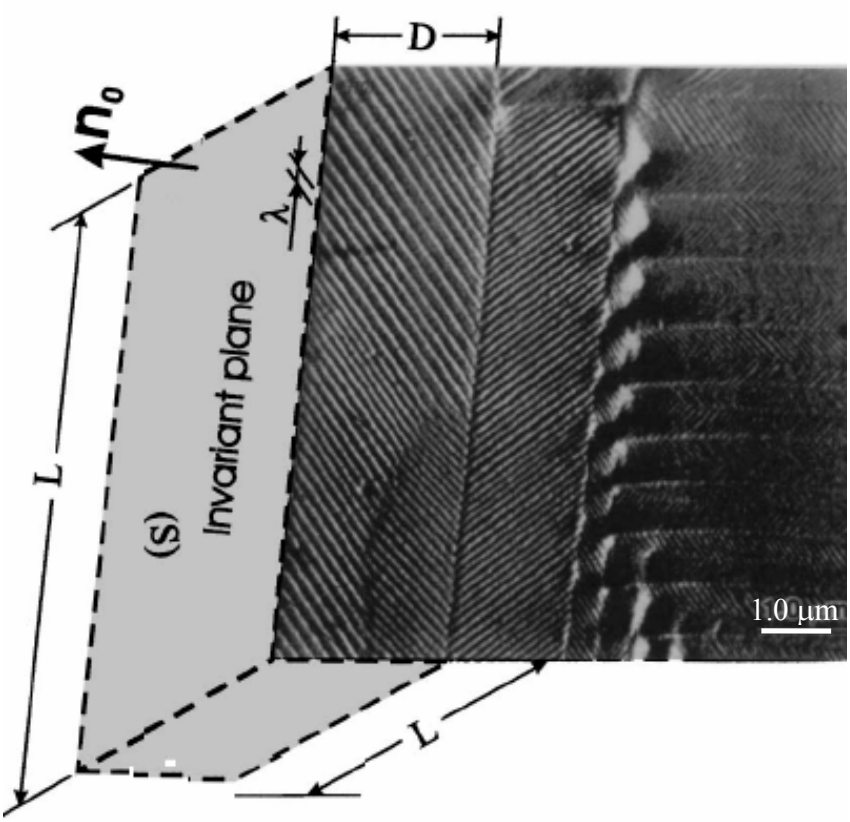

Fig.4-21. Structure of a polydomain martensitic plate consisting of alternating lamellae of two twin-related orientation variants (domains) of the martensite shown by black and white. The boundary between the lamellae is the twin plane. The ratio of the "black" and "white" domain thicknesses provides the macroscopic invariancy of the habit plane. These plates fully fill a sample. [Ref.44]

PZN-x%PT crystals. It predicted the self-assembly of nano-domains into particular topologies, whose hierarchy was determined by stress accommodation and specific geometrical invariant conditions. The theory unambiguously predicted that the M phases of PMN-x%PT and PZN-x%PT are not homogeneous, but rather an adaptive mixed structural state with microdomain-averaged adjustable topological parameters. Changes in PND topology then resulted in changes in domain hierarchy, and also in an apparent phase stability.

Self-assembly of Domain Engineered States in PMN-x%PT

In PMN-x%PT crystals, we believe three ingredients – stress accommodation, polarization compensation, and random fields[99] – are key to understanding the domain hierarchy. Partial stress accommodation may occur at the 'fingerprint' boundaries, in addition to partial polarization compensation. Also, hierarchal self-assembly is apparently complicated by random-fields, which partially compensate the polarization.

At lower PT contents, random-fields may limit self-organization of the domain hierarchy. Thus, only PNRs or PNDs are observed, which do not assemble into striations or 'fingerprints', nor do macrodomain plates form. The domain morphology is non-stress accommodating. However, with increasing PT content, as the MPB is approached which has a significantly higher c/a ratio, stress accommodation of the PND may become critical. To minimize the elastic energy, the PND may begin to assemble into geometrical patterns that achieve the invariant conditions required of stress accommodation. Since the invariant plane for R and T domains lies along the {110} and {010} respectively, it is natural that colonies of PND assemble with a morphology oriented along these two planes, as showed in Fig.4-19(c). To achieve a more complete stress accommodation,

macrodomain plates then form. At higher PT contents, in the T phase region, the domain hierarchy is much more like that expected of a conventional C→T phase transition in ferroelectric perovskites. Critical to the fine 'fingerprints' is a low domain wall energy density – which is the key requirement for the conformal miniaturization of stress-accommodation. Our results show that this requirement is satisfied only in the vicinity of the MPB.

Field cooling may alter the distribution of PND. Thus, the domain hierarchy can be changed by electrical history. In the FC condition, for both PMN-30%PT and PMN-35%PT, the domain striations were reduced in size relative to the ZFC one. This significant increase in domain wall density may favor the conformally-miniaturized stress accommodating (or adaptive) ferroelectric state. In the ZFC condition, the lattice symmetry of PMN-30%PT is phase R, and X-ray reflections are relatively broad; whereas in the FC condition, the lattice symmetry is M_A, and the reflections considerably sharper.[87] Sharpening of the reflections also occurs in the M_c phase of PMN-35%PT on field-cooling. Comparisons of these observations with the PFM images indicate that field-cooling may favor a shorter-scale geometrical patterning of miniature polar domains. In this case, the reduction in the inhomogeneous line broadening may reflect a relaxation of the elastic strain energy between miniature domains, which also alters the domain hierarchy.

4.5 Polarization switching in (001)_oriented PMN-x%PT

Polarization rotation instabilities under field within FE_M phases are known, where rotation occurs against a very small anisotropy.[29] Investigations of the induced polarization (P) have shown significant differences depending upon whether the crystals are driven under unipolar or bipolar electric field (E): unipolar results in anhysteretic P-E responses, whereas bipolar results in significant hysteresis.[100-101] Clearly, domains play an important role in polarization switching under bipolar drive.

Polarization switching has been extensively investigated in normal ferroelectric materials by measuring current transients in response to square wave electrical pulses of reverse electric field (E).[102-109] Early investigations by Mertz revealed a model for polarization reversal where 2-D nucleation of reversed clusters is restricted to 180^o domain walls,[102] and where 1-D growth of reversed step-like domains is restricted to be coherent in a direction perpendicular to that of E. It is known in finite-size systems that the Mertz model is inapplicable,[110] which has been modified by Scott et al.[111] However, it was not until recently that defects were considered to play a vital role in polarization switching.[112-114] For example, in PMN-x%PT,[99,113-114] polarization switching under E has been understood by heterogeneous nucleation in the vicinity of quenched random fields that act conjugate to E.

However, direct (in-situ) evidence of polarization switching by heterogeneous nucleation in the vicinity of random fields has not previously been reported. The purpose of this investigation was to study the domain evolution of (001)-oriented PMN-20%PT and PMN-35%PT crystals with changing DC electric bias by SFM in the piezoresponse

mode. The results provide direct evidence of heterogeneous domain nucleation and growth, where nucleation is not restricted to occur at domain boundaries.

SFM images were again obtained in the piezoresponse mode. During image scanning, an ac voltage with a frequency of 20 kHz and amplitude between 1 and 10V was applied between the conductive tip and the bottom gold electrode. During polarization and/or switching, the ac bias was reduced to zero; and a step-changed dc bias was superimposed on the bottom electrode to switch the polarization within a small central portion of the initial image, which was achieved by moving the grounded SFM tip only over this small area. [Also see reference 115]

Fig.4-22 shows the piezoresponse force images of PMN-20%PT for various electrical histories. Data are shown in this figure beginning from the initial annealed state, followed by increasing positive V_{dc} on the central $2\times2\mu m^2$ area (left-hand column), subsequently followed by increasing magnitude of negative V_{dc} on the central $1\times1\mu m^2$ area (right-hand column). The sequence of bias changes can be followed by the arrows in the figure. In the initial annealed condition (center top), polar nano domains (PND) were observed, somewhat similar to those previously reported by electron microscopy [25,26]. The distribution of PNDs was almost random, although there was evidence of organization of PND into regular colonies with some spatial correlation. On application of positive V_{dc} (left-hand column), the self-organization of the colonies was broken down, leaving only randomly distributed polar regions of nano-meter size. With increasing V_{dc}, the density of the PND was decreased, eventually becoming a single domain state at V_{dc}=10V (solid dark area). On subsequent application of negative V_{dc} (right-hand

column), nano-sized polar nuclei were formed, which were randomly distribution within the matrix. With increasing V_{dc}, the density of these nuclei was increased, until a reversed single domain state (solid bright area) was formed. These results directly show that polarization switching in (001)-oriented PMN-20%PT crystals occurs by heterogeneous nucleation, where nuclei creation is not confined in the vicinity of domain boundaries, but rather can occur throughout the crystal volume.

Fig.4-23 shows the piezoresponse force images of PMN-35%PT for various electrical histories, presented in a similar manner as that of Fig. 1. In the annealed condition (center top), long and thin domain striations oriented along {110} were apparent, which had a somewhat regular spacing. The domain lengths were on the order of tens of microns, whereas the widths were dramatically less. On application of positive V_{dc} to the central $4\times4\mu m^2$ area (left-hand column), the striations became thinner and less regular. With increasing V_{dc}, the striations broke down into isolated PND, eventually becoming a single domain of the same polarization at V_{dc}=12V (solid dark area). On subsequent application of negative V_{dc} to the central $2\times2\mu m^2$ area (right-hand column), polar nuclei of nano-meter size formed, which were randomly distributed. With increasing V_{dc}, the nuclei density increased and self-organized into {110} striations, indicating a stress-accommodated domain growth process. However, the twin boundaries appeared fuzzy or diffuse, presumably due to the interaction of polarization with charged point defects. These results indicate that polarization switching initiates by preferential nucleation near pre-existing twin boundaries; however with increasing V_{dc}, nucleation occurs heterogeneously throughout the crystal volume. At higher voltages, a reversed single domain state (solid light area) was found at V_{dc}= -9.0V (solid bright area).

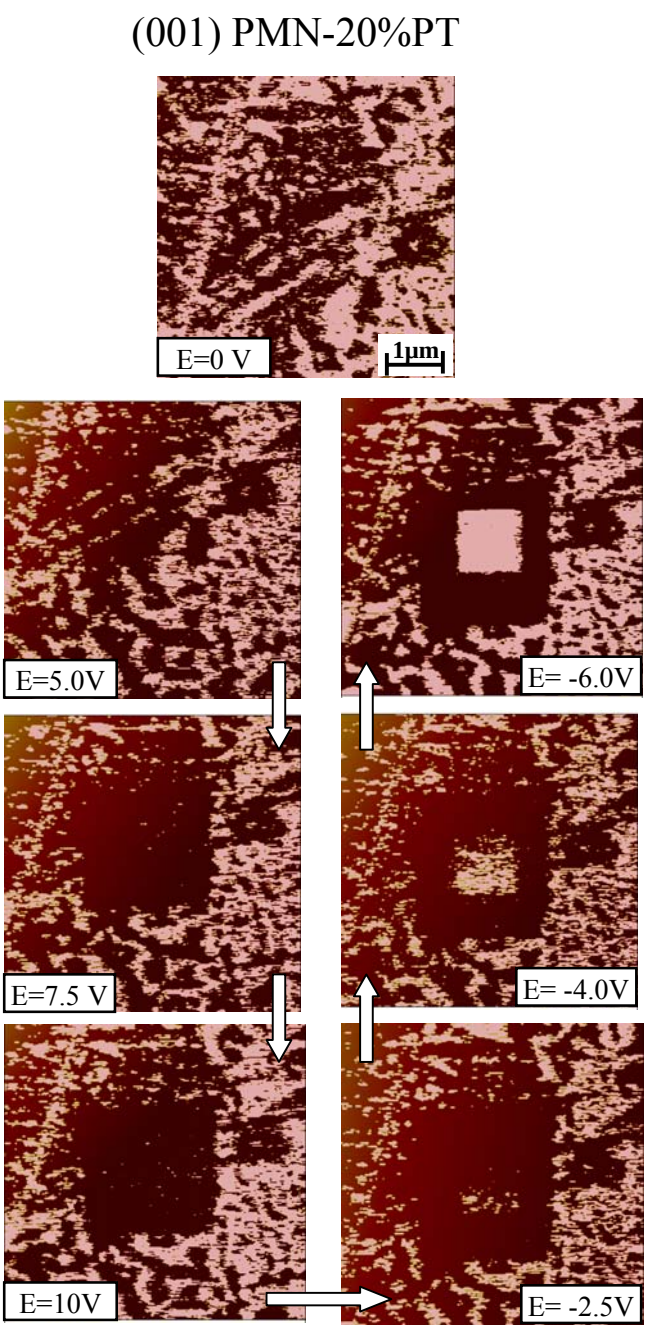

Fig.4-22. PFM images for a (001)-oriented PMN-20%PT crystal under various dc electrical voltages, top center: the initial annealed condition; left-hand column: under positive bias on the bottom electrode; right-hand column: under negative bias on the bottom electrode.

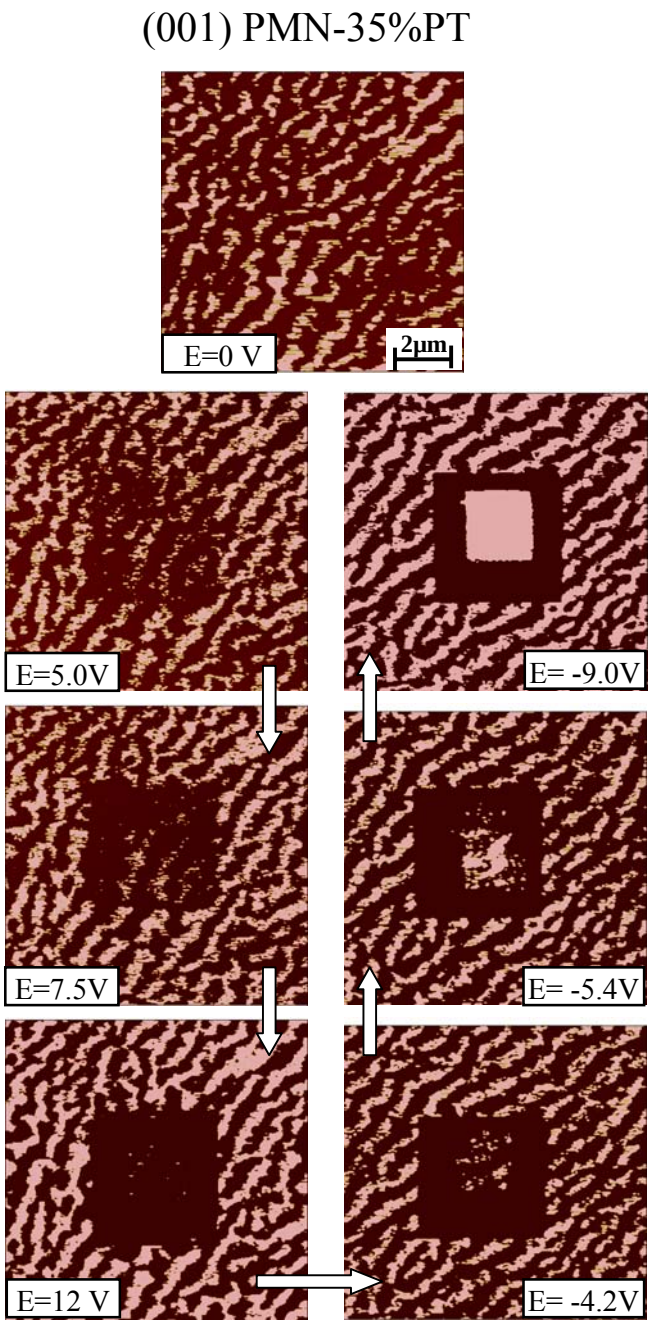

Fig.4-23. PFM images for a (001)-oriented PMN-35%PT crystal under various dc electrical voltage, top center: the initial annealed condition; left-hand column: under positive bias on the bottom electrode; right-hand column: under negative bias on the bottom electrode.

Our results are consistent with recent pulsed polarization switching investigations of PMN-x%PT and PZN-x%PT by current transient methods [20-22]. In these investigations, polarization switching for PMN-30%PT and PZN-4.5%PT was found to follow stretched exponential behavior. Following the random-field theory of disordered magnetic systems,[116-117] the results were explained as heterogeneous nucleation of nano-sized domains in the vicinity of quenched random fields that act conjugate to E. Accordingly, switching occurs by a mechanism where domain walls become diffuse with increasing E, due to the creation of polar nuclei heterogeneously throughout the crystal volume; rather than by the creation of 2-D nuclei of reversed clusters geometrically restricted to the vicinity of pre-existing 180^o walls. Recent investigations by Jullian et al.[114] revealed two long-time transients that followed stretched exponential behavior: one for $t>10^{-2}$ sec under moderate E which was dimensionally confined to domain walls (n=2), and a second for $10^{-4}<t<10^{-2}$ sec under higher E which was a volume process (n=3) that was geometrically unconfined with nucleation preferentially occurring in the vicinity of defects or random-fields. For lower PT content crystals which are closer to relaxor systems, our piezoresponse force images directly reveal, that nucleation is a volume process occurring in the vicinity of quenched random fields; whereas for higher PT content crystals near the MPB, nucleation is initially geometrically confined to domain walls (n=2), but with increasing voltage a switchover to a volume process (n=3) occurs that is unconfined.

In summary, domain switching of (001)-oriented PMN-x%PT has been investigated by SFM in a piezoresponse force mode under various superimposed DC electrical voltages. The results provide direct evidence of heterogeneous domain nucleation for

PMN-20%PT, where nucleation is not restricted to occur at domain boundaries. With increasing PT content to 35%PT, nucleation preferentially initiates near existing twin boundaries; however, the boundaries become diffuse with increasing V_{dc}, due to heterogeneous nucleation and growth throughout the volume.

4.6. Summary

Both bulk phase transformation and local domain structures of PMN-x%PT ($10<x<40$) relaxor-type crystals have been investigated by XRD and PFM. Significant contribution of PNRs to the enhanced electromechanical properties in compositions near MPB has been found, which can be summarized as followed,

1) The phase transformational sequence of PMN-30%PT crystal is (i) $C \rightarrow T \rightarrow M_C \rightarrow M_A$ in the FC condition; and (ii) $R \rightarrow M_A \rightarrow M_C \rightarrow T$ with increasing E at constant temperature starting from a ZFC condition. Thus the MPB range can be enlarged by apply E-field along [001] direction. M_A is the dominant phase at room temperature, whereas M_C phase becomes stable above 350K.
2) Inhomogeneities of PNR exist in a wide range for $10<x<40$ in PMN-x%PT. With increasing PT concentration, they first grow into PNDs with R phase symmetry that can be resolved by XRD or neutron scattering; then self assemble into micron domains with <110> preferred orientation (R or M symmetry) by stress-accommodation. With increment of the c/a ratio, the M domains further assemble into <100> macro plates (T symmetry). Since full stress accommodation and complete polarization compensation can not be achieved on one length scale due

to the existence of random fields, a domain hierarchy is developed on various length scales ranging from nanometer to millimeter.

3) The existence of a domain hierarchy down to the nm scale fulfills the requirement of low domain wall energy, which is necessary for polarization rotation. Thus, upon applying an E-field along <001> direction(s) in a composition near the MPB, low symmetry phase transitions can easily be induced, by altering the orientation and distribution of PNDs. For compositions with T symmetry, applying an E-field only assists sidewise growth of large domains along the direction of E-field and shrink of others.

4) Finally, polarization switching is also controlled by the density of PNRs (or PNDs) and their degree of stress accommodation. For PMN-20%PT with a high density of PNDs and weak stress accommodation, heterogeneous domain nucleation was favored, which was not restricted to occur at domain boundaries. However, for PMN-35%PT with a low density of PNDs and strong stress accommodation, domain nucleation is tuned by applied E-fields: nucleation preferentially initiates near existing twin boundaries; however, the boundaries become diffuse with increasings E-field, due to heterogeneous nucleation and growth of domains.

V. ROLE OF INHOMOGENIETIES IN FE-GA CRYSTALS

5.1 Introduction

The recent discovery of a large magnetostrictive strain (λ_{100}>200ppm) in Fe-Ga single crystals demonstrates that the magnetostriction of Fe can be dramatically enhanced by substitution of non-magnetic elements.[52] Compared to commercially available magnetostrictive Terfenol-D alloys, Fe-Ga alloys have additional advantages, such as (i) high mechanical strength; (ii) good ductility; and (iii) high-imposed stresses, which are particularly good at low applied magnetic fields (H<150 Oe).

The most puzzling question is why a non-magnetic alloying element can increase the magnetostriction by ten times. Investigations of the dependence of the magnetostriction on composition in Fe-x at.% Ga alloys have shown that the value of λ_{111} is almost independent of Ga concentration.[54] However, λ_{100} increases with increasing Ga content, reaching a maximum for x~17-19, subsequently decreasing sharply for 20<x<25; and a second maximum in λ_{100} occurs in the composition range of x=27.5, as shown in Fig.5-1.[54] Furthermore, the position of the first maximum of λ_{100} has been reported to be dependent on thermal history. The first maximum in the magnetostriction is shifted from x≈17 in the furnace-cooled (FC) condition, to x≈19 in the rapidly-quenched (RQ) one. In addition, for 15<x<20, the stable condition in the FC condition has been reported to be a two-phase field of A2+DO_3 phases; whereas in the RQ condition, the same crystal maintains a single phase A2 cubic structure until x≈19at%.[59] All these results indicated

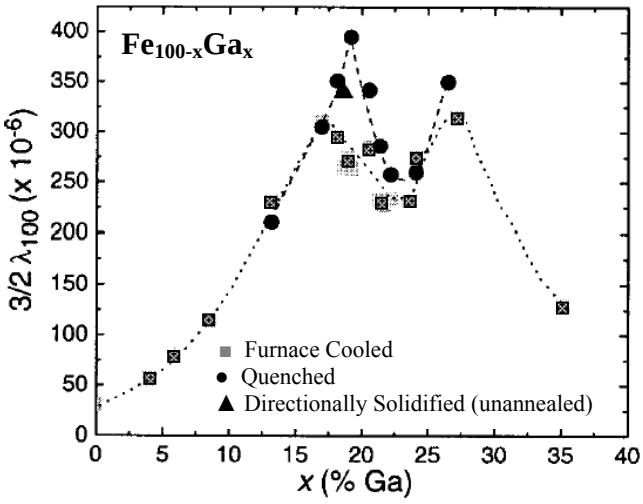

Fig.5-1. $(3/2)\lambda_{100}$ as a function of Ga concentration for furnace cooled, quenched and directionally solidified $Fe_{100-x}Ga_x$. (Ref.54).

that the large magnetostriction in Fe-Ga alloys might be related to clusters of short-range Ga pairs along <100> crystallographic orientation(s), which act as both magnetic and magnetoelastic defects. In other words, Ga-pairs induced low-symmetry distortion may increase the magnetoelastic coefficient, and soften the elastic modulus along <100> direction, as reported by Clark et al.[54] In addition, Ab-initio calculations have also indicated that the tetragonal structure – induced by short-range ordering of Ga atoms – is important to enhanced magnetostriction.[60]

However, structural studies of the distortions induced by short-range clusters of Ga-pairs have yet to be provided. Previous XRD studies of FC Fe-19 at.% Ga have revealed a cubic structure with notable transverse line broadening in (001) mesh scans, indicating a short lateral correlation length.[118] In addition, XRD analysis in the quenched Fe-19 at.%Ga crystal has shown an unexpected peak in the (100) and (111) line scans, which was not consistent with either a disordered bcc or a long-range ordered DO_3 structure.[59] An alternative arrangement of Ga atoms in the unit cell was then suggested: the so-called modified DO_3 phase with a body-centered tetragonal structure, having lattice parameters of $a_t=b_t=4.1$Å and $c_t=2.9$Å.[59] However, since X-rays have only a very limited penetration depth of 3~5μm in Fe-Ga alloy, the obtained results may be affected by surface quality or residual stress. Thus it is necessary to perform neutron scattering in order to probe the bulk structural information of the crystals.

Furthermore, measurements of the magnetic anisotropy have found that K_2 is equal to $-9K_1/4$ over a wide composition range from 5 to 20 at.%Ga.[119] The same type of magnetization versus field behavior has been observed in magnetic shape memory alloys, such as NiMnGa or NiFeGa,[120] over a range of temperature above the cubic to tetragonal

transition. In addition, NiMnGa alloys also show a very soft tetragonal shear modulus, similar with Fe-Ga alloys. It has been reported that an intermediate low-symmetry phase was produced above the martensitic transformation (MT) temperature (T_m), which is known as the precursor effect of the MT. Magnetic domain structure studies in $Ni_{51}Fe_{22}Ga_{27}$ alloys have also provided important evidence of such precursor patterns above T_m.[121-122] It was hypothesized that a similar structure may occur in Fe-Ga alloys. However, to date, investigations of the magnetic domain structure of Fe-x at.% Ga crystals have not been reported. We believe that such studies could provide important information concerning the origins of the enhanced magnetostriction, and why the maximum in λ_{100} is dependent on thermal history.

In the following sections, I will present a combination structural investigation of Fe-x at.% Ga crystals for x=12, 20 and 25 by neutron scattering and magnetic force microscopy (MFM). My intention is to establish (i) the bulk lattice structure of Fe-x at.% Ga to verify if there is any evidence of the local structural distortions; (ii)the dependence of the magnetic domain structure on Ga concentration, determining if there are magnetic domain inhomogenieties; (iii) the relationship between the magnetic domain structures and their thermal history, resolving why the maximum magnetostriciton shifts with thermal history; and (iv) the evolution of the domain configuration during domain rotation under a step-increased magnetic bias.

5.2 Structural investigations by neutron diffraction

The neutron scattering experiments were again performed on the BT9 triple-axis spectrometer located at the NIST Center for Neutron Research. Measurements were made using a fixed incident neutron energy E_i=13.7 meV, obtained from the (002) reflection of a PG monochromator, and horizontal beam collimations of 15'-46'-10'-20'. We exploited the PG (004) analyzer to achieve a fine q-resolution of 0.0104 $Å^{-1}$. At 300K, the pseudo-cubic lattice constant of Fe-20 at.% Ga is 2.903 Å, corresponding to the reciprocal lattice unit (or l rlu) is $a^*=2\pi/a=2.164$ $Å^{-1}$. All mesh scans shown in this study were plotted in reference to this reciprocal unit.

Fe-12 at. %Ga

Fig.5-2 shows neutron mesh scans of Fe-12 at.% Ga taken in the (H0L) zone (a) the (002); and (b) the (200) mesh scan. Comparisons of the results from these two zones show that the crystal growth direction is not a significant influence. Our mesh scans exhibit at least four satellite peaks along the transverse direction, qualitatively similar to that found by XRD (not shown here). Clearly, the transverse splitting is a bulk phenomenon, and not confined to the outer-layer regions of the crystal.

Fig.5-3 shows the (200) and (002) line scans of Fe-12 at.% Ga taken in the (H0L) zone. A single 2θ peak was found in both scans by Gaussian peak fit. A typical value for FWHM was 0.0052 r.l.u. However, there is clear difference between the peak center positions: for the (200) peak, the d-spacing was 2.888 Å; whereas for the (002) peak, the d-spacing was 2.901 Å. Although the resolution of current triple-axis neutron scattering is about 0.0048 r.l.u., these results may indicate the presence of a tetragonal-like distortion.

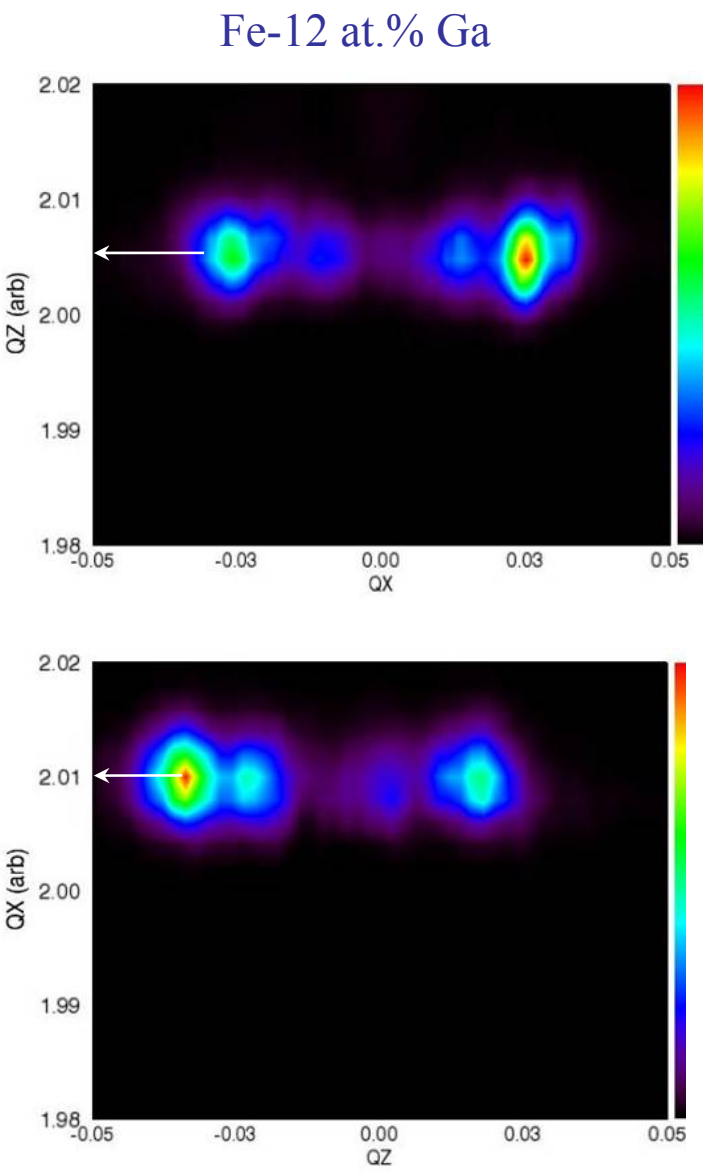

Fig.5-2. (a) (002) and (b) (200) mesh scans of Fe-12 at.%Ga alloy in the (H0L) zone, where Q_x corresponds to (H, 0, 0) and Q_z corresponds to (0, 0, L).

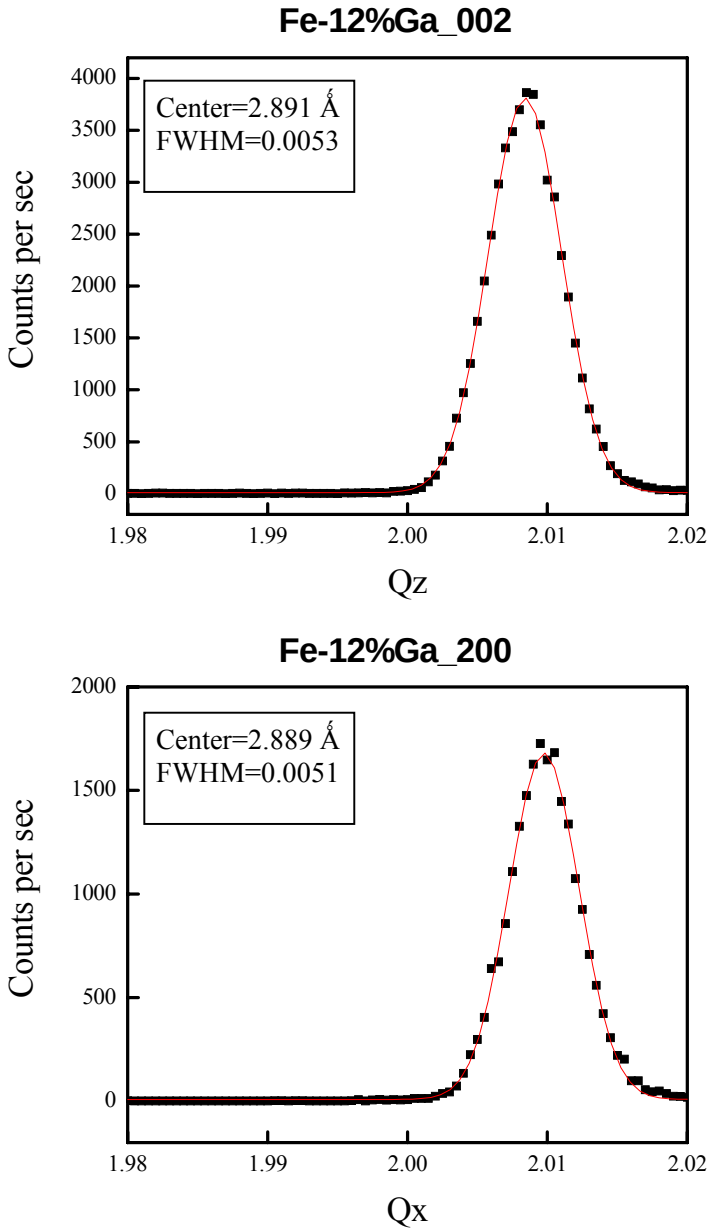

Fig.5-3. (a) (002) and (b) (200) line scans of Fe-12 at.%Ga alloy in the (H0L) zone, where Q_x corresponds to (H, 0, 0) and Q_z corresponds to (0, 0, L).

Fe-20 at.% Ga

Fig.5-4 shows neutron mesh scans of Fe-20 at.% Ga taken in the (H0L) zone, (a) the (002) mesh scan; and (b) the (200) mesh scan. Similar peak splitting along the transverse direction has been found. There are clear two differences compared with the corresponding mesh scans of 12 at.% Ga, which are (i) the number of satellite peaks decreases to three, which may indicate an improvement of the crystal homogeneity; and (ii) the 2θ peak along the longitudinal direction is very broad, extending from approximately $1.99 \leq L \leq 2.01$.

We then performed (200) and (002) line scans with a finer step size, as shown in Fig.5-5. Gaussian fits revealed a single broad peak for both line scans, with a typical FWHM about 0.008 r.l.u., and a lattice parameter of a=2.904 Å. According to the phase diagram, Fe-20 at.% Ga is located within the A2+DO_3 two phase region, where the volume fraction of each phase depends on the thermal history of the crystal. If the phase fractions are not equivalent, the 2θ peak will be asymmetric. Accordingly, we tried to fit the line profiles with two Gaussian peaks, but obtained a fitting with a higher error than that by a single peak. In addition, a typical FWHM of ~0.006 r.l.u. was obtained, larger than that of Fe-12at.%Ga. We then repeated these experiments using a Ge (004) analyzer with a much better resolution of 0.0012 $Å^{-1}$: again, a similar broad peak was observed. Since the structures of A2 and DO_3 are very similar, precipitation of DO_3 nuclei within the A2 matrix could lead to fine-scale microstructure in which it is difficult to distinguish one phase from another. Thus, we conclude that Fe-20at.% Ga has a pseudo-cubic structure, i. e. an averaged-cubic structure; however, this does not exclude the possibility of an intimate mixture over a length scale smaller than that of neutron beam coherence.

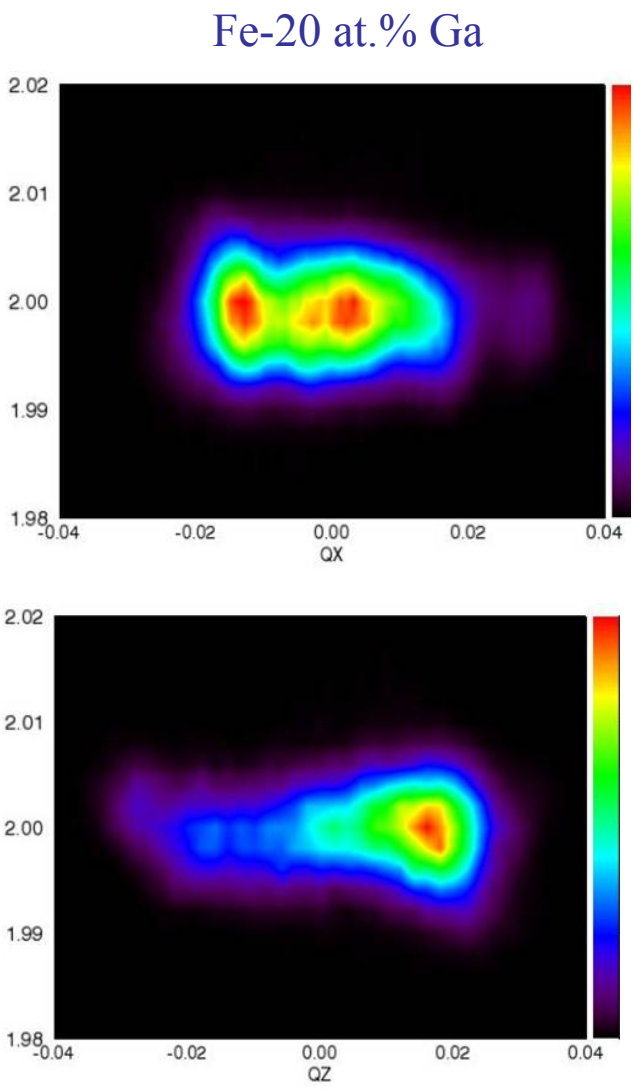

Fig.5-4. (a) (002) and (b) (200) mesh scans of Fe-20 at.%Ga alloy in the (H0L) zone, where Q_x corresponds to (H, 0, 0) and Q_z corresponds to (0, 0, L).

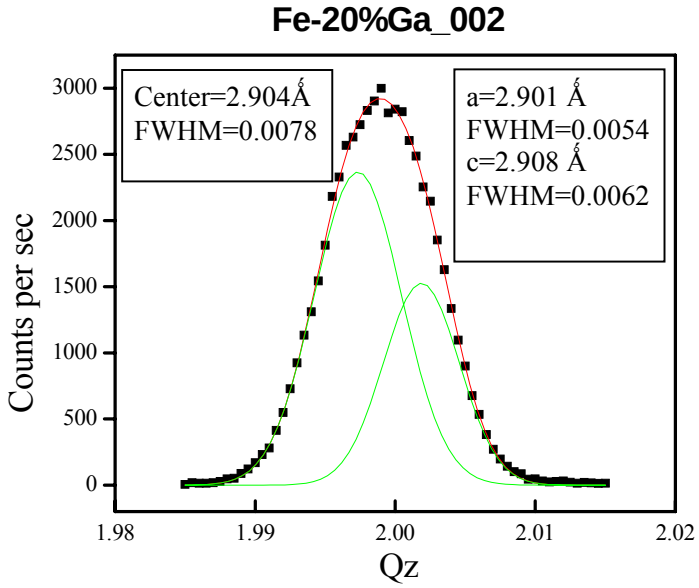

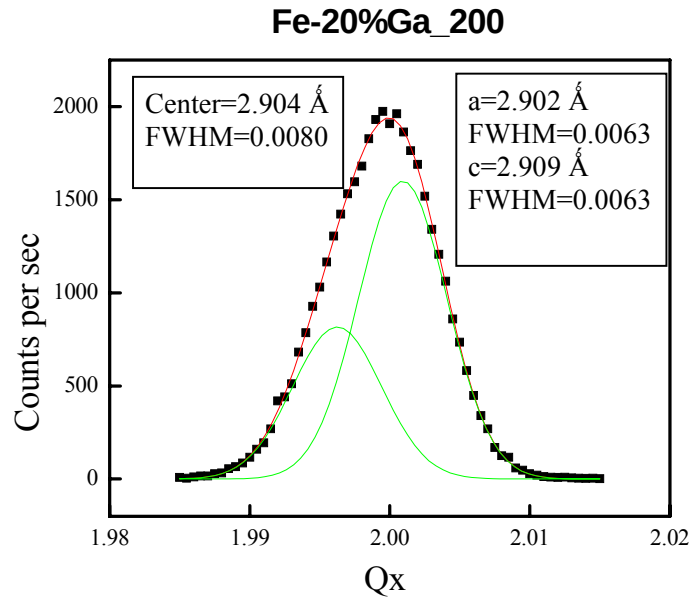

Fig.5-5. (a) (002) and (b) (200) line scans of Fe-20 at.%Ga alloy in the (H0L) zone, where Q_x corresponds to (H, 0, 0) and Q_z corresponds to (0, 0, L). Red lines were fitted by single Gaussian curve; green lines were fitted by two Gaussian curves.

Fe-25 at.% Ga

Fig.5-6 shows neutron mesh scans of Fe-25 at.% Ga taken in the (H0L) zone, (a) the (002) mesh scan; and (b) the (200) mesh scan. Only two satellite peaks along transverse direction were found, which may indicate further improvement in crystal homogeneity. Fig.5-7 shows the (200) and (002) line scans of Fe-25 at.%Ga taken in the (H0L) zone. A sharp single peak was found by Gaussian peak fit in both scans. A typical value of FWHM was 0.0044 r.l.u. And analysis of the peak center positions of (200) and (002) line scans yielded an identical lattice parameter of a=2.901 Å.

Discussion and summary

The mesh scan results demonstrate the presence of regions that are slightly tilted with respect to each other. In each case, the angle of rotation about the transverse direction was quite small ($<0.5^{o}$). We found that it was possible to distinguish between A_2 (x=12), intermediate bridging (x=20), and DO_3 (x=25) phase regions by the type of splitting along the transverse direction. A 4-fold splitting was found for A_2; a 3-fold for the intermediate region; and a 2-fold for DO_3. All satellite peaks have a similar transverse FWHM of ~0.0078 r.l.u. We believe that the tilting of {001} planes results in a texture pattern that one might loosely say in colloquial-terms resembles a "quilt" – in that it consists of slightly different pieces that have all been stitched together nice and snug, not perfectly, but with some (crystallographic) character. The texture pattern then changes with x, being notable different in the various phase regions of the crystalline solution. We note that changes in structural texture may influence magnetic domain size and regularity,

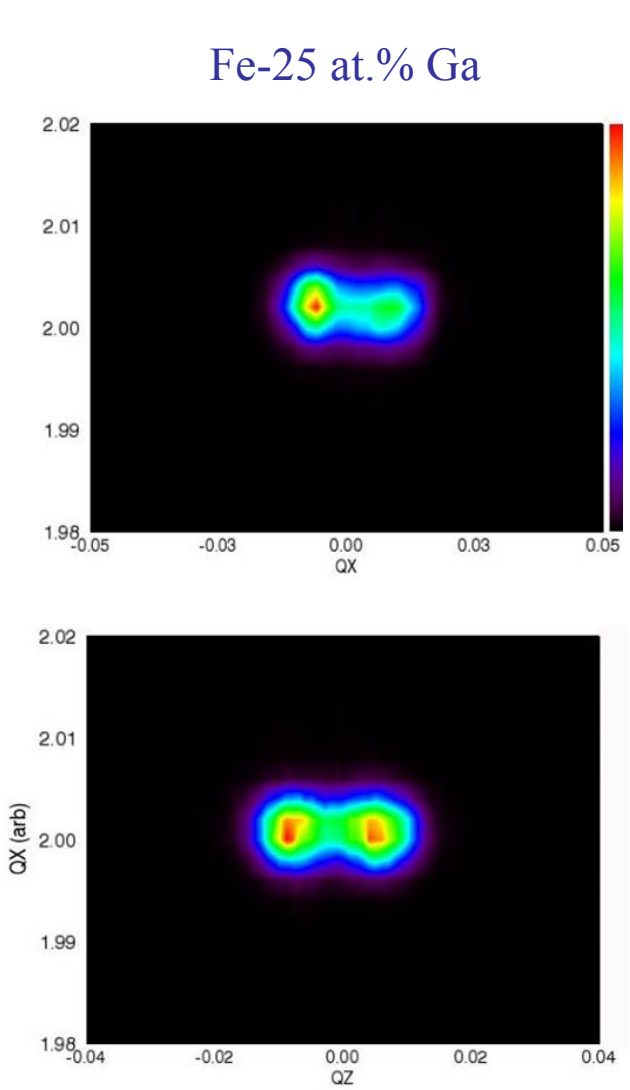

Fig.5-6. (a) (002) and (b) (200) mesh scans of Fe-25 at.%Ga alloy in the (H0L) zone, where Q_x corresponds to (H, 0, 0) and Q_z corresponds to (0, 0, L).

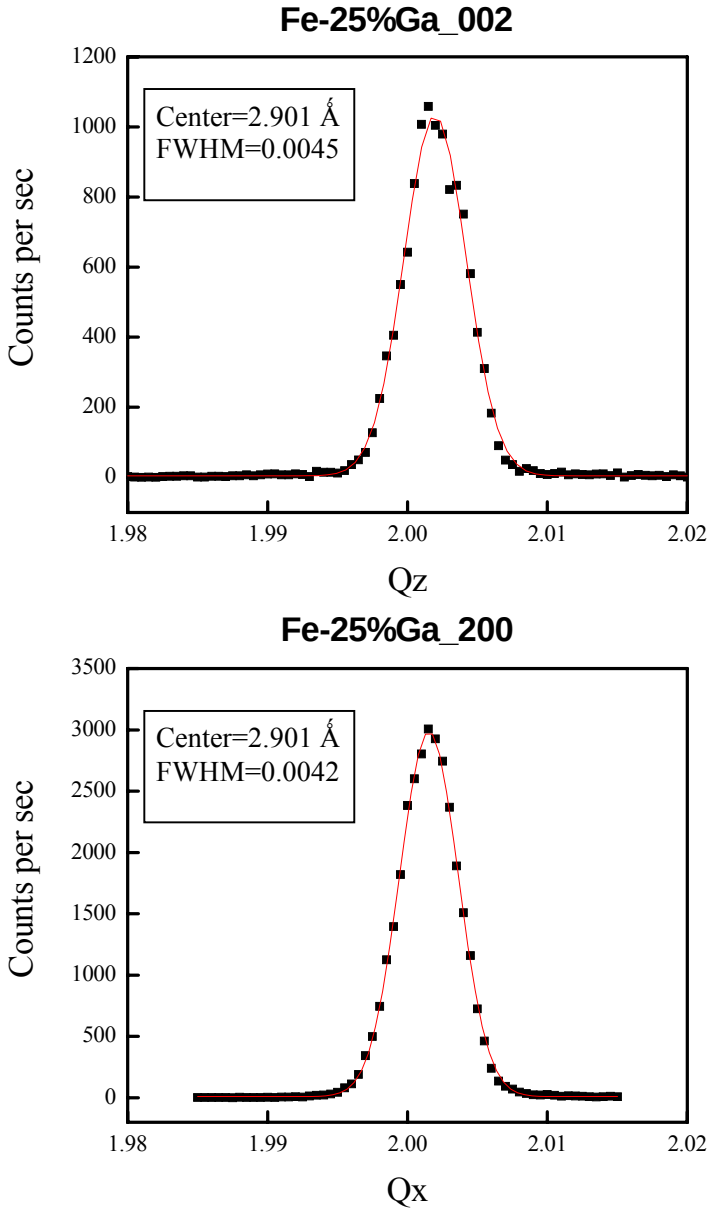

Fig.5-7. (a) (002) and (b) (200) line scans of Fe-25 at.%Ga alloy in the (H0L) zone, where Q_x corresponds to (H, 0, 0) and Q_z corresponds to (0, 0, L).

as will be shown in Section 5.3: in the A_2 phase, macrodomain plates with a strong {001} preferred orientation have been observed by MFM; whereas for DO_3, only miniature domains with much reduced preferred orientation were found.

Furthermore, our results have clearly shown a 2θ peak broadening sequence of 20 at.% Ga>12 at.% Ga>25 at.% Ga. Normally, the lattice structure determined by XRD or neutron scattering is the same as the local structure in a single crystal. However, in systems consisting of inhomogeneous entities, whose size is less than or close to the coherence length of X-rays or neutron beams, the diffraction pattern may reflect an averaged lattice structure, rather than the crystal lattice of individual parent phase or inhomogeneity. This is similar with what we have discussed in ferroelectric relaxors with PNRs. According to phase diagram, Fe-12 at.%Ga has a disordered A2 phase, Fe-20 at.% Ga has A2+DO_3 phase and Fe-25 at.% Ga has a pure DO_3 phase. However, there is actually no clear phase boundary between the A2 and DO_3 phases, which is strongly dependent on the thermal history of the crystals. Local DO_3 or modified-DO_3 clusters (Ga-pairs) may coexist with the A2 phase over a wide composition range, contributing to the broadening of the 2θ peak. Accordingly, Fe-20 at.% Ga has a broader peak due to the increase of Ga concentration and degree of fine-scale local inhomogeneities. However, Fe-25 at.% Ga is generally regarded as a pure long-range ordered DO3 phase, so the 2θ peak is very sharp. According, the change of peak broadness with Ga concentration is consistent with the change of magnetostriction predicted according to Ga-pairs model.

Finally, it might be helpful to clarify the difference between “Ga-pairs” and “pre-martenstic” (PM) phenomena in the literature. Premartensite is found above the

martensitic transition temperature in either Ni-Al or Heusler-type NiMnGa alloys: it has a clear low/reduced symmetry structure, monoclinic or orthorhombic, compared to either the parent austenite (cubic) or fully formed martensite (tetragonal) phase.[40,123] In these regards, PM is an intermediate phase. Khachaturyan et al. has thus developed an adaptive theory for these particular low-symmetry intermediate phases,[42] which I designate as **PM_I**. (also see Section 1.2.4) According to this theory, T_m is actually above the temperature where PM_I appears. In the PM_I state, tetragonal domains are conformally miniaturized, and geometrically arranged to achieve particular invariant conditions that minimize the elastic energy. However, following Kartha,[41] there is another "glassy" PM state (I designate here as **PM_{II}**), where tetragonal clusters exist within a austenite (parent) matrix. In this case, the elastic compatibility between neighboring domains is not necessary to achieve. This is consistent with previous elastic neutron scattering investigation of Ni_2MnGa,[123] in which a diffuse quasi-elastic peak was found in the same peak position of PM_I during cooling, however, at a temperature above T_M. Accordingly, with regards to Fe-Ga alloys, my results reveal similarities to PM_{II} for compositions close to A2-DO_3 boundary: fine-scale structural inhomogeneities (i.e., local tetragonal distortion) results in diffuse scattering, but do not geometrically arrange into colonies to achieve elastic accommodation.

In summary, our experiments reveal (i) a tetragonal-like distortion for x=12, (ii) a single broad pseudo-cubic peak for x=20, which may be caused by local inhomogenities of Ga-pairs; and (iii) a splitting transverse to the (002), revealing a structural domain texture in which domains are slightly tilted with respect to each other, and whose pattern changes with x.

5.3 Magnetic domain structures of Fe-x at.% Ga

5.3.1 MFM Images

Fig.5-8(a) and (c) shows the domain structures of furnace-cooled (FC) Fe-12 at.% Ga. To better illustrate the overall domain morphology and local domain features, images with different scan scales are shown. It should be noted that there are some magnetic defect lines on the MFM images due to physical scratches, however, these scratches are homogenous in topography (not show here) and thus have little influence on our domain alignment analysis. In the region designated by the symbol **A** in Part (c) of this figure, the magnetic domains can be seen on average to be aligned along the [100] direction. The domain width is ~0.5μm, and its length ≥10μm. However, we did find regions in which the domain alignment was disrupted, and a typical magnetic closure pattern was established, as designated by the symbol B. According to Lord, when the domain configuration is terminated by a surface defect, the demagnetization or magnetostatic energy will in general attempt to reduce the volume of any domain having a magnetization normal to the surface, and thus generates closure domain patterns. Domain structures of Fe-12 at.% Ga in the post-annealed (PA) condition are shown in Figs.5-1(b) and (d), again images with different scan scales are shown. A similar domain structure was found; except that the domains were much wider, and also had a higher degree of [100] alignment. These slight differences in domain structures between the FC and PA conditions may reflect corresponding variations in the magnetostriction with thermal history that was previously reported.[54]

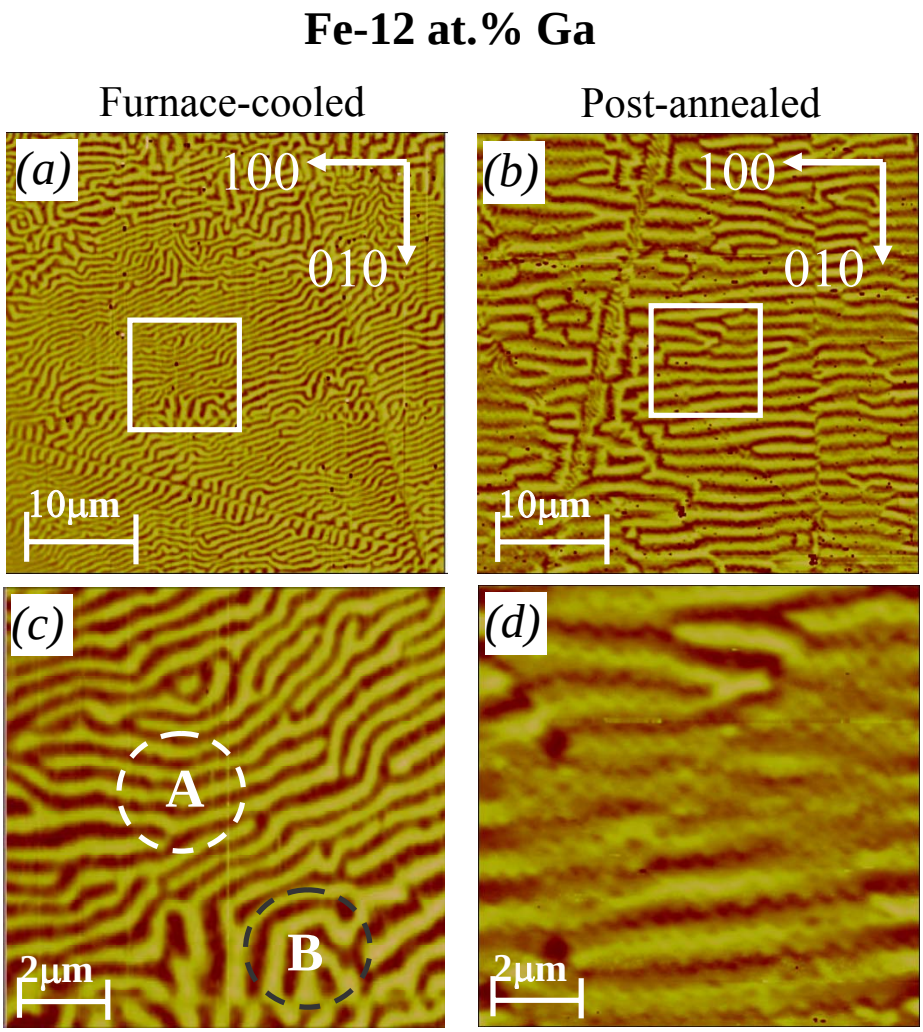

Fig.5-8. MFM images of the (001) surface of Fe-12 at.% Ga at furnace cooled condition, (a) and (c); and after being post-annealed, (b) and (d). Region A shows an area populated by domains preferentially aligning along [100] direction and region B shows broken domains and magnetic closure patterns.

Fig.5-9 shows MFM images of the domain structure of Fe-20 at.% Ga. Part (a) and (c) show the domain structure in the FC state. In Part (a), small domains of micron-size or below can be seen to be arranged within [001]-oriented domain platelets of 5-10 μm width and 30-50μm length. Part (c) shows an image with a higher resolution of $10x10\mu m^2$, which better illustrates the features of the finer domains. These domains can be seen to be much smaller in size and much less regular than the corresponding ones for Fe-12 at.% Ga, as can be seen by comparing Fig.5-8(c) and Fig.5-9(c). The fine scale domains of FC Fe-20 at. %Ga were ~0.4μm in width and <2μm in length. These fine scale domains, or sub-domains, tended to have some [010] preferential orientation; however, (i) the domain walls were often bent or rough, (ii) there was considerable bending between [010] and [100] variants, and (iii) there were domain regions not restricted to this crystallographic direction. Part (b) and (d) show the domain structure in the PA state. The image in Part (b) shows the presence of [001]-oriented domain platelets of 5-10μm width and 30-50μm length that have a finer internal domain structure – in these two regards, the results from the FC and PA conditions are similar. However, there was a significant difference between these two conditions, with regards to the morphology and distribution of the fine domain structure within the platelets. Part (d) shows a higher resolution image taken from an area of 10 μm^2. This image illustrates that the sub-domains organize into dendrite morphology.

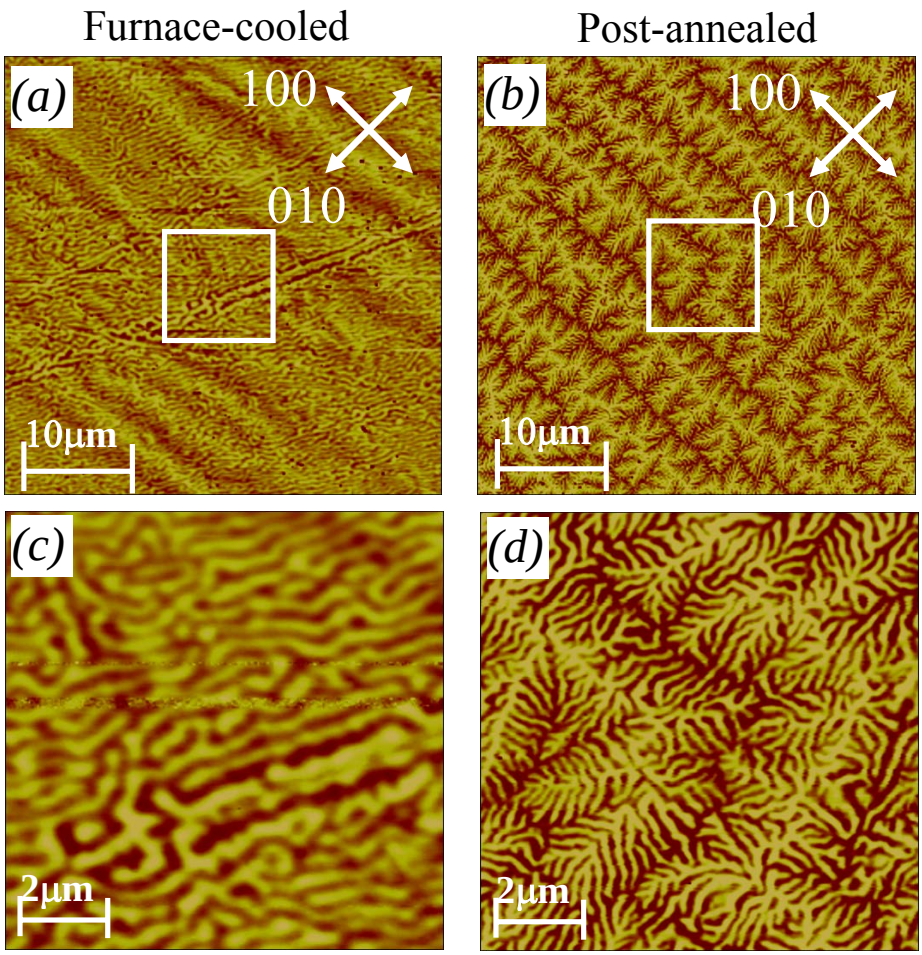

Fig.5-9. MFM images of the (001) surface of Fe-20 at.% Ga at furnace cooled condition, (a) and (c); and after being post-annealed, (b) and (d).

Finally, the magnetic domain structures of Fe-25 at.% Ga are shown in Fig.5-10: Part(a) in the FC condition, and Part (b) in the PA conditions. Similar domain structures were found for both conditions. Macrodomain platelets were not found, rather the only observable feature in the MFM images was the finer sub-domains. A typical length and width of these sub-domains was <1μm and <0.2μm, respectively. The fine domains have somewhat preferred alignment along [010] direction, but notably less than that for lower Ga-content crystals. These results indicate that the DO3 phase is fully formed for Fe-25 at.% Ga. This was confirmed by XRD, and is consistent with prior results which have reported the boundary between the two phase (A2+DO3) and DO3 phase fields at about x=23 at.% Ga.[57]

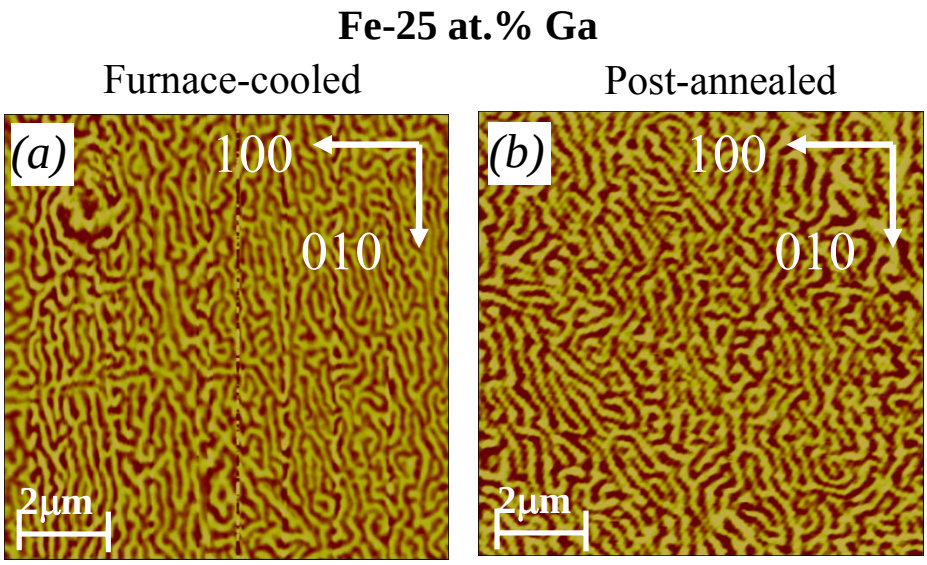

Fig.5-10. MFM images of the (001) surface of Fe-25 at.% Ga in the furnace-cooled state, (a) and after being post-annealed, (b), to show similar domain structures less preferentially aligned along [010].

5.3.2 Fast Fourier Transformations analysis of MFM images

Next, we performed Fast Fourier Transformations (FFT) on the MFM images. This allowed us to obtain a better measure of domain alignment and features, in both x- and y-directions. The FFT algorithm separates the original waveform into its constituent parts, mapping each wavelength on a 2D spectral plot, providing information on (i) domain alignment - well aligned domains have narrow frequency bands and thus sharp contrast in FFT images; (ii) domain orientation - the symmetry of the wavelength distribution reflects domain orientation; and (iii) the value of the wavelength represents the average width of aligned domains – the shorter wavelengths lie around the periphery of the plot, whereas the longer wavelengths lie near its center, and the center-most point is labeled as "DC" (for "direct current") which corresponds to a size equal to that of the image.

Figs.5-11(a) and (b) show the FFT of the Fe-12 at.% Ga images originally given in Figs.5-8(a) and (b), which are FC and PA states respectively. A two-fold symmetry along the x-axis ([100] direction) can be seen for both images, clearly revealing that the domain structure has a significant degree of [100] preferred alignment, i.e., 180^{o} oriented along [100]. In the FC condition, relative to the PA, we noticed (i) two additional peaks with notably weaker intensities that were slightly rotated away from the [010], indicating 90^{o} domains that are slightly tilted presumably to relax the elastic energy; and (ii) that the intensity had a diffuse halo, with a relatively broad distribution of radii, indicating significant domain size non-uniformity. The wavelengths were then determined to be $1.7<\lambda_x<4\mu m$ and $0.6<\lambda_y<0.9\mu m$ for the FC state, and λ_x=DC and $\lambda_y\approx1.4\mu m$ for the PA state. These results clearly show that post-annealing increases the domain size and its regularity.

Figs.5-11(c) and (d) show the FFT result of Fe-20 at.% Ga in the FC and PA states, originally shown in Figs.5-9(a) and (b) respectively. Similar to 12 at.% Ga, a two-fold symmetry was also found for Fe-20 at.% Ga, which was strictly aligned along [010]. The average wavelengths were $\lambda_x \approx 10$ and $\lambda_y \approx 10$ μm for the FC state, and $\lambda_x \approx 8$μm and $\lambda_y \approx 8$μm for the PA one – which corresponds to the size of the [100] macrodomain plates in the MFM image. We then obtained the FFT of the higher resolution MFM images for Fe-20 at.% Ga (Figs.5-9(c) and (d)), shown in the insets of Figs.5-11(c) and (d) respectively. These insets show a diffuse halo with peaks close to the [100] and [010] directions. Post-annealing was found to result in an increase in the diffuseness of the halo, and an increase in its radii. The FFT of Fe-20 at.% Ga evidences hierarchial domains organized over different length scales, whose degree of organization and wavelengths are both decreased by post-annealing.

Figs.5-11(e) and (f) show FFTs of Fe-25 at.% Ga in the FC and PA states, respectively. [Please note the different frequency scales.] The signature feature of the FFT for Fe-25 at.% Ga crystals was a broad and diffuse halo, with $0.3<\lambda_R<0.5$μm ($\lambda_R = \sqrt{\lambda_x^2 + \lambda_y^2}$). The results indicate a lack of organization of the miniature domains into a crystallographically regular pattern; although, weak intensity peaks indicate some residual domain alignment along [010].

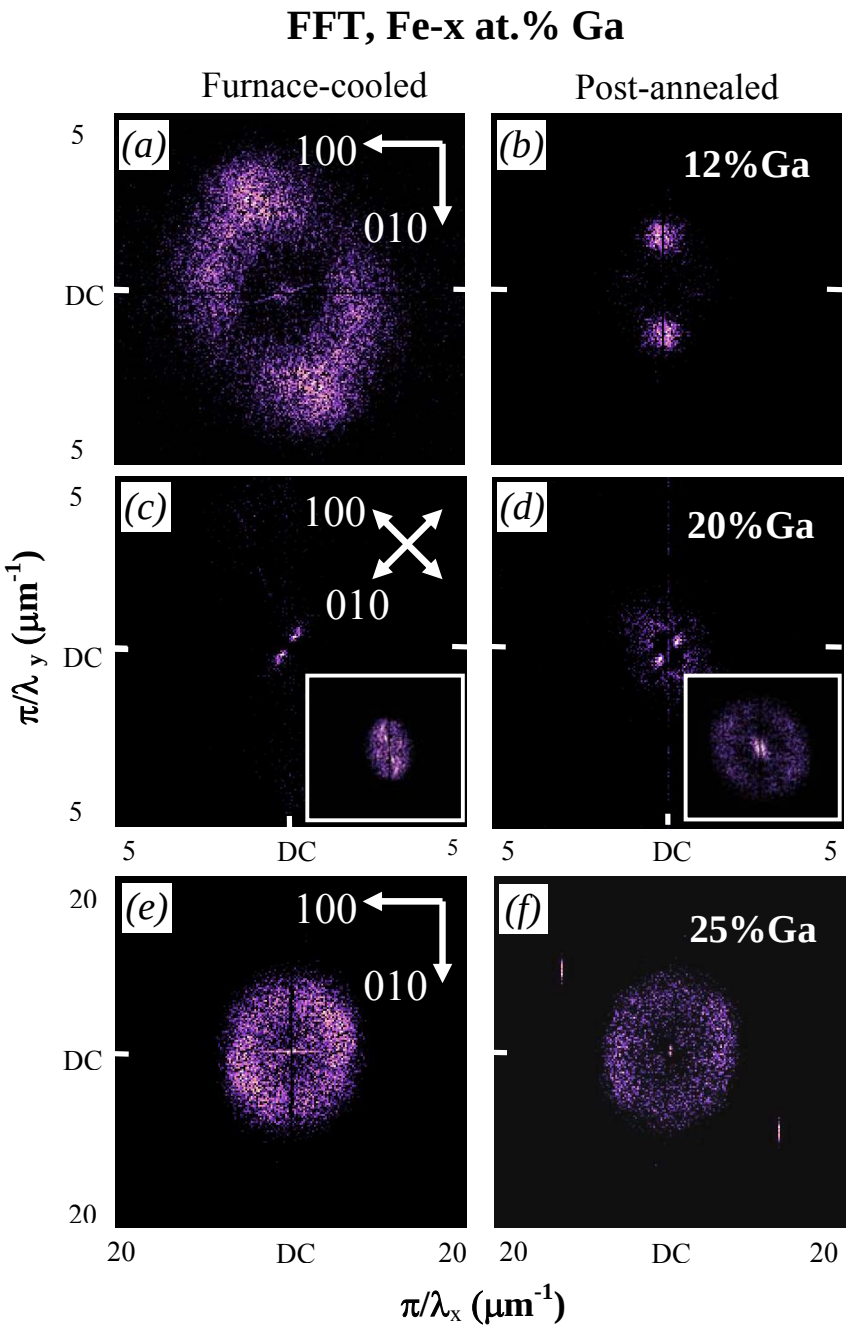

Fig.5-11. FFM images of (001) surface of Fe-12 at.% Ga, (a) and (b); Fe-20 at.% Ga, (c) and (d); and Fe-25 at.% Ga in the furnace-cooled and post-annealed state, respectively. The insets are the FFT images corresponding to Figure 3 (c) and (d) with fine domain structure to show domain hierarchy in different scales. Both of the insets have a frequency scale from 20 μm^{-1} to DC.

5.3.3 Discussion and Summary

Thermal history dependent magnetostriction

The observation of sub-domains with a dendritic morphology in Fig.5-9 is indicative of a phase change, possibly due to the DO_3 structure as previously reported.[57] According to the phase diagram in Fig.3-2, the phase boundary of A2+DO_3 and DO_3 is located at x~22.5at%Ga. Recent work by Clark et al. has shown that slowing cooling favors precipitation of the DO_3 phase.[54] Thus, it is reasonable to conjecture that the dendrite contrast in the MFM image may arise due to an intimate two phase mixture of DO_3 and A2 phases, which have magnetization differences. The self-organization of the dendrites into [100] oriented macrodomain plates indicates that these two phases maintain a degree of mutual adaptivity with respect to each other on cooling below the Curie temperature into their magnetostrictive states. Decomposition may affect the local magnetization contrast, but does not prevent elastic accommodation on a longer length scale that results in conventional macordomain plates.

We also carried out structure analysis to investigate the effect of annealing. Fig.5-12(a) shows the lattice parameters of Fe-20 at.%Ga crystals with different thermal histories. A clear peak position shift and phase separation process can be seen from FC state to the PA conditions. Fig.5-12(b) shows the (200) line scans of Fe-x at.%Ga. It can be seen that the lattice parameter increases with increasing the Ga concentration. This is consistent with previous XRD studies.[124] Comparison of Fig.5-12 (a) and (b) revealed that the peak center position of Fe-20 at.% Ga has a lower 2θ value than that of Fe-25at.%Ga, which has also been confirmed by neutron scattering, as shown in Section 5.2.

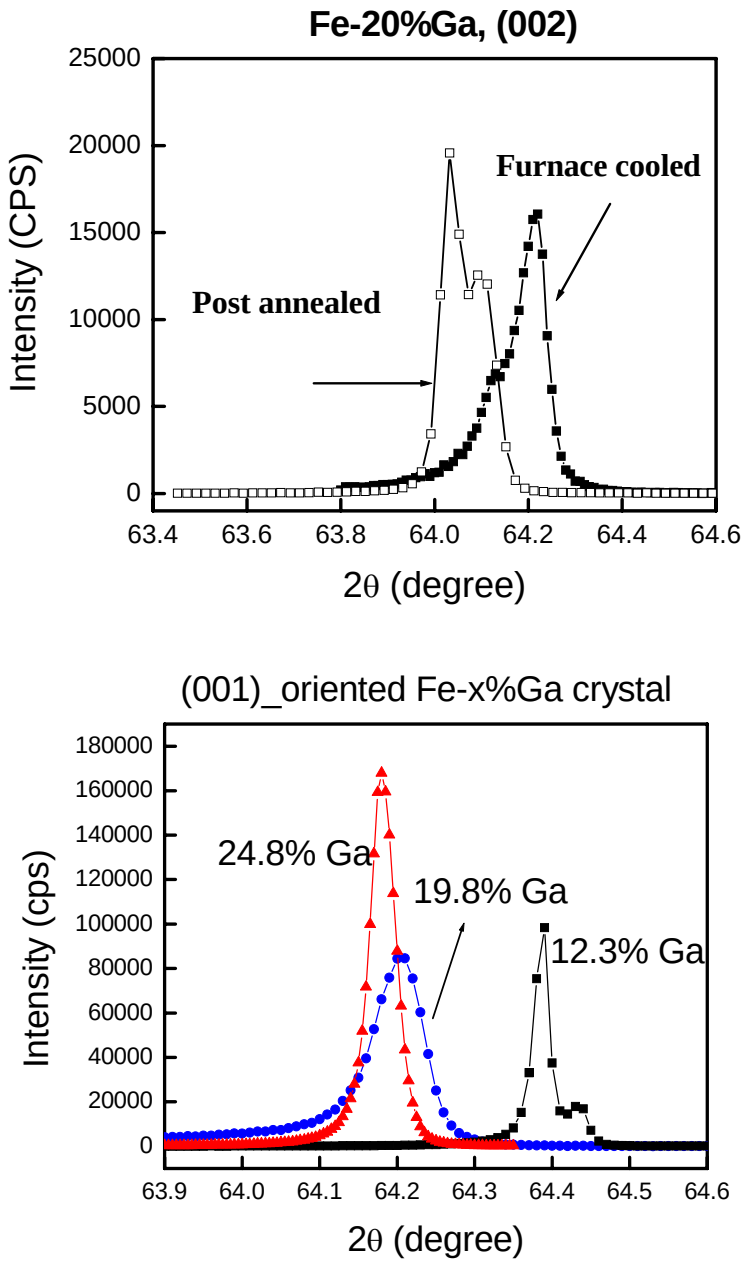

Fig.5-12. X-ray diffraction line scans taken along the (002) zone for (a) Fe-20at%Ga in the furnace-cooled and post-annealed conditions; and (b) various (001)-oriented Fe-x%Ga crystal in the as-grown condition for 12<x<25.

Accordingly, it can be inferred that the post annealing shifts the lattice parameter of 20at.%Ga in a similar manner to that of a crystal with a higher Ga concentration.

One remaining question of the thermal history influence on the magnetostriction of Fe-x at.%Ga near A2 and DO_3 phase boundary is whether the number of Ga-pairs is dependent on cooling rate or not. The question is very important since we might further enhance magnetostriction by increasing the number of Ga-pairs along the <100> directions. The comparison of furnace-cooled and fast quenched from 800°C (>T_c) Fe-x at.%Ga mentioned earlier has evidenced an enhanced magnetostriction for 17<x<19.[54] However, it is well known that fast cooling favors complete disordering instead of Ga-pairs along the special <100> directions. Thus, only those pairs along <100> directions existing prior to cooling can undergo para- to ferro-magnetic transformation and persist down to room temperature. Consequently, increasing the cooling rate only helps to (i) stabilize disordered A2 phase to high Ga concentration in phase diagram; and (ii) increase the number of Ga-pairs due to the increase of total Ga concentration, both of which are important for large magnetostriction. However, raising the cooling rate can not increase the number of Ga-pairs for a constant composition. This is why no enhancement was observed for 5<x<17 composition.[54]

Magnetic domain inhomogeneities

The results of our investigation demonstrate with increasing x that (i) the typical domain size is decreased; (ii) the domain morphology becomes increasingly irregular; and (iii) the degree of [100] preferential orientation is reduced. These results clearly show increasing domain inhomogeneity with increasing Ga content. The enhancement of λ_{100}

with increasing x below 19 (see Fig.5-1) has previously been attributed to the emergence of directional short-range ordering of Ga pairs.[58] However, our MFM results indicate that domain non-uniformity may also play a key role in enhanced magnetostriction. This may be due to an increase in the ease of domain movement – it is much easier to move a diffuse wall than a sharp one in the presence of quenched disorder.[125] Recent investigations of elastic constants have shown that the value of $\frac{1}{2}(C_{11}-C_{12})$ decreases as the Ga content is increased in the Fe-x at. % Ga alloys. The combination of these prior[54,58] and our present results indicate that metastable pre-martensitic states may be trapped by quenched disorder, as predicted by earlier theories of Kartha et. al.[41]

The fact that the magnetic domains in Fe-12 at.% Ga had a strong degree of preferred [100] orientation on the (001) plane, instead of [100] and [010] closure domains, indicates an intrinsic deviation from a conventional BCC structure in the A2 phase. This crystallographic restriction is not unique to tetragonal structures, but rather can also be found in lower symmetry orthorhombic and monoclinic domain variants, which have in-equivalent c- and a-axes. As mentioned in Section 5.1, previous XRD studies of quenched Fe-19 at.% Ga crystals have shown that (i) the c-axis of the tetragonal distortion lies parallel to the direction of Ga-pairing;[59] and (ii) an elongation of the diffraction peak (i.e., peak broadening) along the [101] direction in mesh scans, indicative of orthorhombic or lower symmetry structural modulations.[113] These prior XRD results that indicate distortions from a conventional tetragonal domain variant are consistent with our observation of decreasing domain regularity with increasing x. It implies a hetero-phase region over a relatively large phase field, where the characteristic length-scale of the DO_3 phase depends on Ga-content and thermal history.

In summary, the domain structure of furnace-cooled and post-annealed Fe-x at.% Ga crystals have been investigated by magnetic force microscopy for $12<x<25$. Our results indicate the importance of quenched disorder on a domain hierarchy. With increasing x, we have observed a decrease in (i) the typical size of the magnetic domains within macro-domain platelets, and a disappearance of the platelets in the DO_3 phase field; (ii) the degree of domain regularity; and (iii) the degree of [100] preferred orientation. Our results indicate enhanced magnetostriction for crystals with miniaturized domains that retain good [100] preferred orientation. In addition, post annealing with slow cooling rate tends to favor the separation of DO_3 phase and thus equivalently shift the Ga concentration to a high value. This is the reason that the maximum magnetostriction shifts in the phase field with changes in thermal history.

5.4 Magnetic domain rotation in Fe-x at.% Ga

In this section, we use MFM to observe the domain rotation upon applying the magnetic field normal and parallel to the surface of a sample. The domain structures of Fe-x at.%Ga alloys in the A2+DO_3 and DO_3 phase range were compared. These results indicate the increase of density and degree of domain fluctuations with increasing applied magnetic field, which may be caused by randomly distributed short-range Ga-pairs, serving as magnetic and magnetoelastic defects.

Fig.5-13 shows the MFM images of Fe-19.5 at.%Ga upon applying a step-increased magnetic field normal to the surface - Part (a) shows an image of $40\times40\ \mu m^2$, and Part (b) shows a high resolution image of $10\times10\ \mu m^2$. With increasing magnetic field, two processes can be seen controlling the magnetic rotation, which are (i) the shrinkage of domains; and (ii) the increasing number of domain fluctuation, as emphasized by white circles. The domain width changes from ~300nm to ~200nm upon applying H=400 Oe. The shrinkage of domain width normal to the applied field direction can be explained by a classical closure-type domain structure, as shown on the bottom of Fig.5-13(b). Such domains are generally observed in cubic ferromagnetic crystals with $K_1>0$. Upon applying the magnetic field, the elongation of closure domain will be confined by the two main domains, thus results in an increase of the stress and magnetoelastic energy.

Fig.5-14 shows the magnetic domain rotation process upon applying the magnetic field parallel to the sample surface: left column, image size $40\times40\ \mu m^2$; right column, high resolution images of $10\times10\ \mu m^2$. Again, the number of magnetic domain fluctuations was seen to increase with the increase of magnetic field. Since the

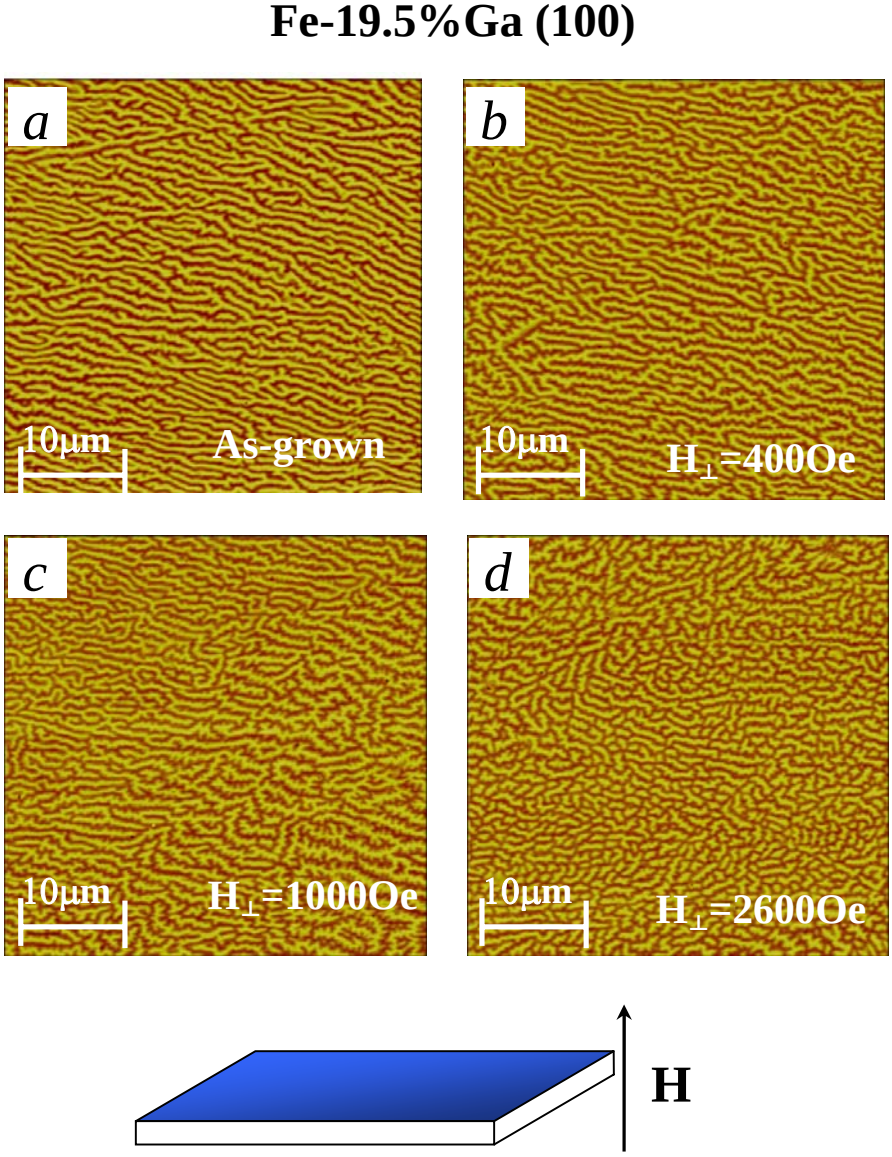

Fig.5-13(a). Magnetic domain configuration of Fe-19.5 at.% Ga crystal during magnetization rotation under magnetic field normal to the (001) surface. Image size 40×40 μm^2.

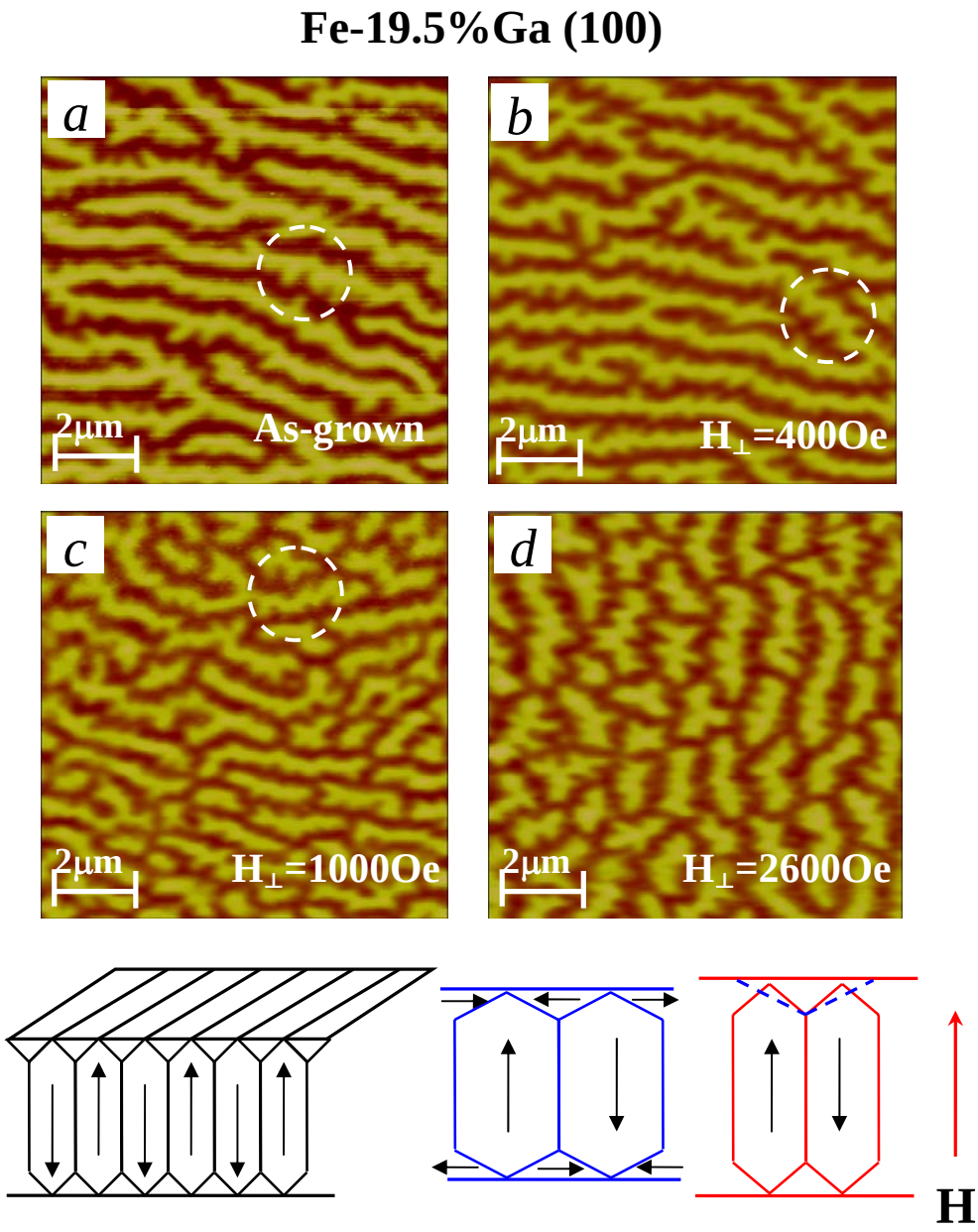

Fig.5-13(b). Magnetic domain configuration of Fe-19.5 at.% Ga crystal during magnetization rotation under magnetic field normal to the (001) surface. Image size 10×10 μm^2. Bottom- the closure-type domain before and after applying magnetic field.

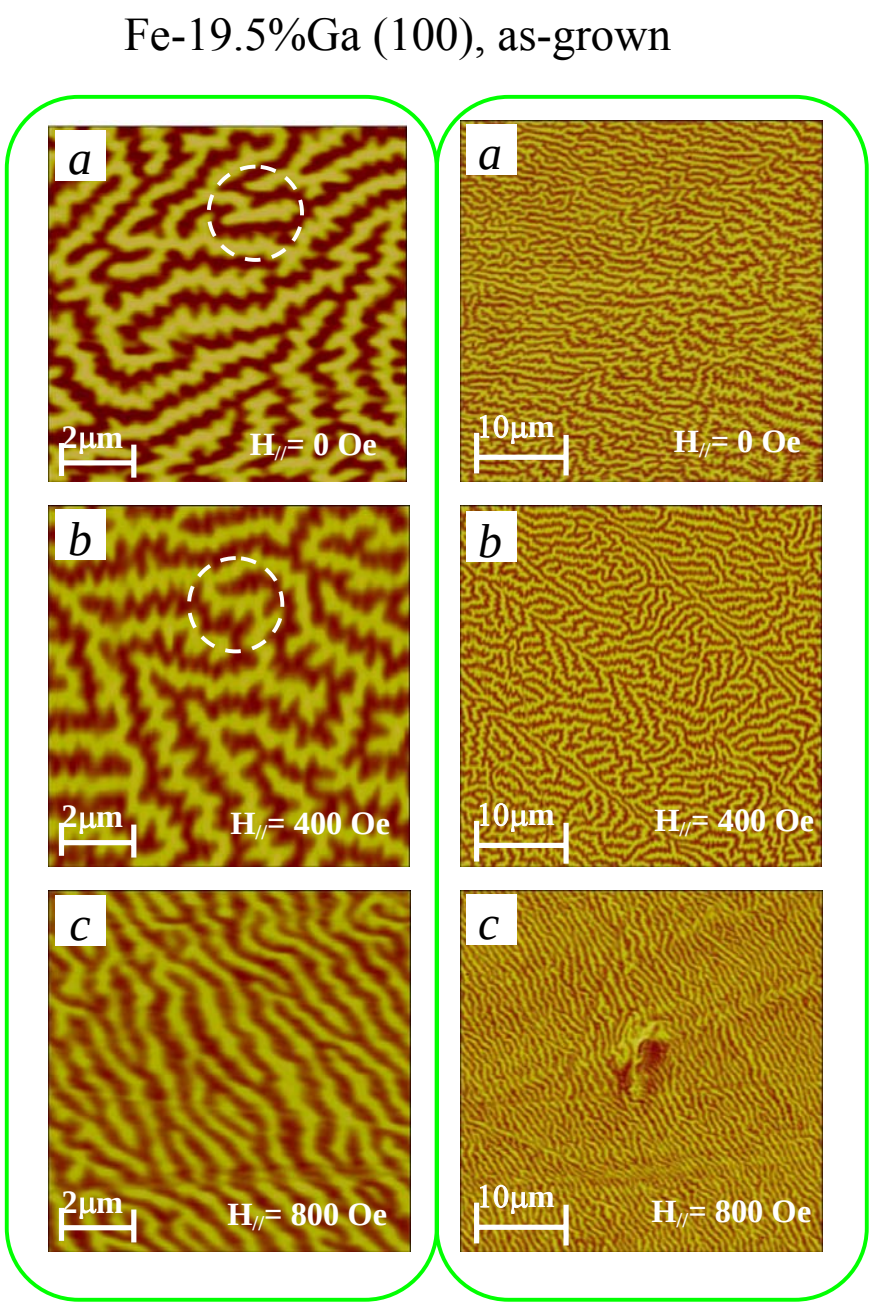

Fig.5-14. Magnetic domain configuration of Fe-19.5 at.% Ga crystal during magnetization rotation under magnetic field parallel to the (001) surface. Left column: Image size 10×10 μm^2; right column: Image size 40×40 μm^2.

demagnetization effect can be neglected in this case, only a low magnetic field is needed to fully rotate the magnetic domains.

Finally, we performed MFM studies on high Ga concentration of Fe-25 at.% Ga, where long-range ordering of DO3 structure is fully established. Fig.5-15 shows the magnetic domain configuration before applying field, Part (a); upon applying step-increased fields of H=~400 and 800 Oe normal to the surface, Part (b) and (c); and after removal of magnetic field, Part (d). Regular dot-like domains were seen with typical size of ~200 nm, and no domain fluctuation was observed upon applying magnetic field. The domains return to their origin state after removing field.

Domain fluctuation can be caused by defects, a secondary phase, a nonmagnetic phase, and etc. In the present case of single crystals, one apparent source of magnetic fluctuation is surface defects. However, the number of these defects should be independent of external magnetic field. Thus, there must be some other source(s) relating to magnetic domain fluctuation. Previous studies of NiFeGa domain structures by Lorentz microcopy have shown two distinct modulations of magnetic flux lines during cooling from parent cubic phase: (i) modulation of the magnetic flux that subdivides the original micrometer-sized domains into the scale of 100 nm; and (ii) local fluctuation (of the order of 10 nm) that may be responsible for the speckles-like features,[121-122] as illustrated in Fig.5-16. These modulations were explained by the precursors of phase transition, as mentioned in Section 5.1: such features are eliminated when tetragonal martensite finally forms. Accordinlgy, one could conjecture that another source of domain fluctuation may be short-range Ga-pairs clusters, i.e. a random-field state.

Although Fe-20 at.% Ga crystal has an anisotropy constant K_1 close to zero, locally, clusters may have a much larger anisotropy constant due to a lower-symmetry structure. Such low-symmetry distortions, induced by random fields, could serve as magnetic and magnetoelastic defects, coupling the local magnetic domain with the bulk elastic strain, and contributing to enhanced magnetostriction.

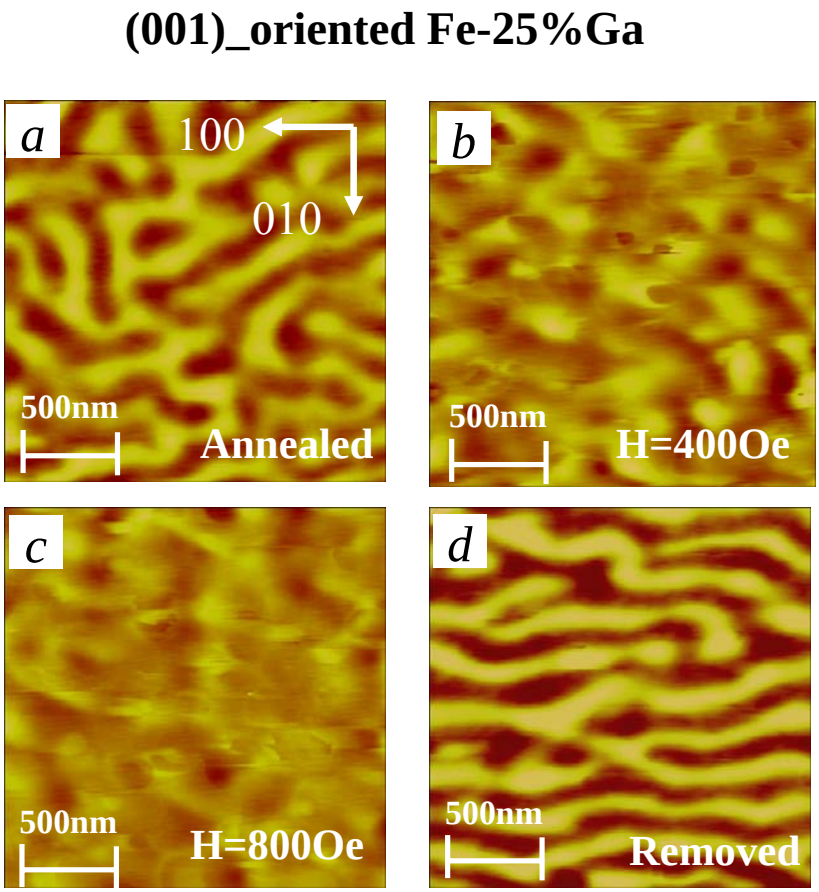

Fig.5-15 Magnetic domain structures of Fe-25 at.% Ga before applying the field, Part (a); upon applying step-increased fields of H=~400 and 800 Oe normal to the surface, Part (b) and (c); and after removal of magnetic field, Part (d).

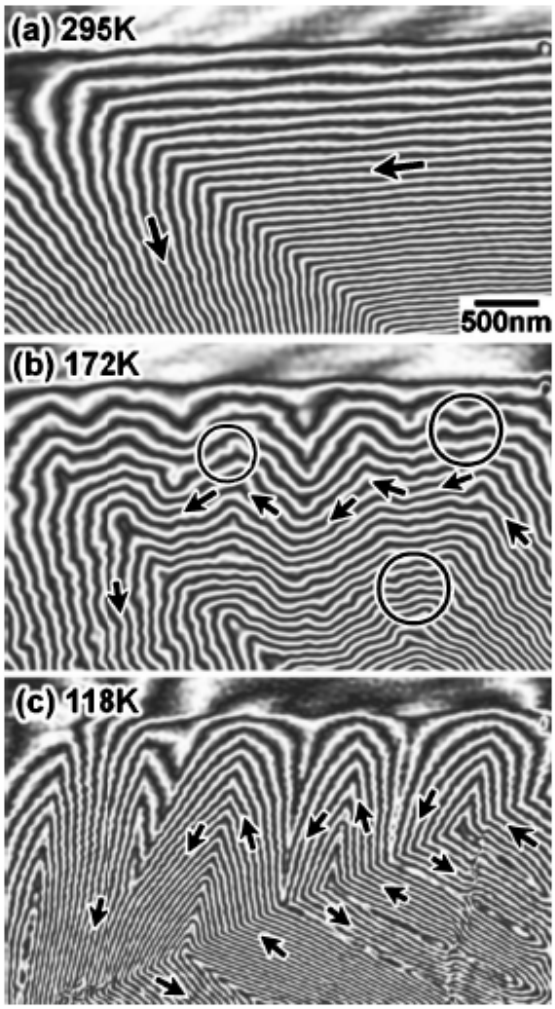

Fig.5-16. Change in the reconstructed phase images with cooling in a $Ni_{51}Fe_{22}Ga_{27}$ alloy heat-treated at 1473 K. The images were obtained for a same area. Black lines represent the lines of magnetic flux projected along the incident electron beam. Arrows indicate the direction of magnetic flux. [Ref.121]

5.5 Summary

The magnetic domain configurations and crystal lattice structures of Fe-x at.%Ga (x=12, 20 and 25) alloys have been studied by neutron scattering and magnetic force microscopy, respectively. My results can be summarized, as follows:

1) Existence of short-range ordering has been observed by neutron scattering. Compared to the sharp 2θ peak of Fe-25 at.% Ga that has a long-range ordered DO_3 structure, a notably broad peak was found in Fe-20 at.% Ga, near the A2/A2+DO_3 phase boundary.
2) The magnetic domains in Fe-12 at.% Ga and Fe-20 at.% Ga have a strong degree of preferred [100] orientation on the (001) plane; however, no domain alignment was found in Fe-25 at.%Ga with DO_3 structure. This clearly indicates a deviation from cubic symmetry.
3) A domain hierarchy was found in both furnace cooled and post-annealed Fe-20 at.% Ga crystals with miniaturized domains affected by thermal history. This is the domain structure predicted by the frustration of the magnetization by randomly distributed nano-clusters, having compositional and structural heterogeneities.
4) Post annealing using a slow cooling rate tends to favor the precipitation of the DO_3 phase, and thus effectively shifts the A2-DO_3 phase boundary to a lower Ga concentration. This is the reason that the maximum magnetostriction shifts in the phase field with changes in thermal history.

5) An increasing degree of domain fluctuations was founding during magnetization rotation, which may be related to short-range Ga-pairing clusters with larger local anisotropy energy, serving as magnetic and magnetoelastic defects.

VI. CONCLUSION AND FUTURE WORK

6.1 Conclusion

In this dissertation, I have performed systematic lattice structure, phase transformation and domain configuration studies of two multiferroic crystals, $Pb(Mg_{1/3}Nb_{2/3})O_3$-$PbTiO_3$ (PMN-PT) and Fe-Ga single crystals, both of which either have large electromechanical or magnetomechanical properties.

It was found that polar nano regions (PNRs) have a significant contribution to the enhanced electromechanical properties of PMN-x%PT crystals by assisting low-symmetry intermediate phase transformation. With increasing PT concentration, PNRs first grow into polar nano domains (PNDs) with rhombohedral (R) phase symmetry; then self assemble into micron-sized domains that have <110> preferred orientation. With incremental changes in the c/a ratio, the micro-domains further assemble into <100> macro plates of T symmetry. For compositions near MPB, a domain hierarchy was also observed on various length scales ranging from nanometer to millimeter. The existence of a domain hierarchy down to the nm scale fulfills the requirement of low domain wall energy, which is necessary for polarization rotation. Thus, upon applying an E-field along the <001> direction(s) in a composition near the MPB, low symmetry phase transitions (monoclinic or orthorhombic) are readily induced, via altering the orientation and distribution of PNDs. Detailed investigations revealed that the phase transition sequence of these intermediate phases was strongly dependent on electrical and thermal histories. A complete *E*-*T* diagram of PMN-30%PT has been established.

With regards to Fe-x at.% Ga alloys, short-range Ga-pairings have been shown to serve as both magnetic and magnetoelastic defects, coupling the local magnetic domain to the average elastic strain of the crystals, resulting in enhanced magnetostriction. Evidence of such inhomogeneities has been found by neutron scattering, as evidenced by a 2θ peak broadening near the A2-DO_3 phase boundary. Secondly, MFM images revealed magnetic domains on the nano meter scale, i.e. short-range Ga-pairing clusters resulting in magnetic inhomogeneities. Post annealing using a slow cooling rate favors the precipitation of the DO_3 phase, and thus effectively shifts the A2-DO_3 phase boundary to a lower Ga concentration. Accordingly, the maximum magnetostriction shifts in the phase field with changes in thermal history. Furthermore, an increasing degree of domain fluctuations was found during magnetization rotation, which may be related to a large local anisotropy constant of low-symmetry Ga-pairs clusters.

6.2 Recommendations on future work

6.2.1 What is the stable phase of poled PZN-8%PT at a low temperature?

PZN-8%PT has a C→T→M_C phase transition sequence in the FC condition. An irreversible M_A→M_C transition can be seen during increasing field at constant temperature. So M_C is the dominant phase. This is different from that of PMN-30%PT, where a reversible M_A→M_C transition was found. Since PMN-30%PT and PZN-8%PT have almost the same location in their respective phase diagrams, it would be quite interesting to see whether a reversible M_A→M_C transition occurs at lower temperatures for PZN-8%PT during field cooling.

According to adaptive phase theory, M_A domains consist of a state of miniaturized R domains; while M_C consist of miniaturized T domains. In ZFC condition, a T→R phase transition occurs; while in the FC condition, a reversible M_C→M_A transition is expected, since poling tends to enlarge the M_C and T phase range, but not fully prevent the transition to occur. Conversely, if the M_C phase is stable until very low temperatures, it may indicate that a true T→M_C transition occurs at the atomic level: this means that once the MPB is enlarged by the E-field, it would be stable on cooling to very low temperatures, even after removal of the E-field.

A systematic neutron scattering study of field cooling down to 300 K plus zero-field cooling down to 15K would be helpful to answer these questions. Mesh scans in (H0L) and (HHL) zones should be obtained for comparison.

6.2.2 Can "PNRs" be created by strain engineering?

The existence of PNRs has been explained by compositional, structural or thermal fluctuations. However, quite different from common defects or inhomogeneities, PNRs can form long-range ordering under the E-field, which causes all those complicated domain structures, and contributes to enhanced electromechanical properties. It is well known that PNRs do not exist in normal ferroelectric materials. However, a good question to ask is whether is is possible to create PNRs by domain/strain engineering.

Thermodynamic calculations have predicted a $T \rightarrow M_A \rightarrow R$ phase transition when applying a sufficient $E_{//<111>}$ on a normal ferroelectric material. However, up to now, the intermediate low-symmetry phases have not been reported under such conditions. As mentioned above, polarization rotation requires very small domain wall energy: for normal ferroelectrics, this condition is difficult to satisfy.

However, enhancement of both T_C and remanent polarization has been reported in film-on-substrate systems for normal ferroelectrics.[126-128] It is believed that the 2D clamping from the substrate may result in a change of phase sequence and the appearance of phases forbidden in bulk crystals. Pertsev et al. have suggested a strain-temperature phase diagram,[129] where low-symmetry M or O phase can exist between paraelectric C and ferroelectric T phases under a critical strain level and over a certain temperature range. This is so-called "strain engineering". However, the suggested phase diagrams are yet to be manifested by structural observation.

Accordingly, it is quite interesting to perform both elastic and inelastic scattering of normal ferroelectric films ($BaTiO_3$ or $PbTiO_3$) in the suggested intermediate phase range. Such studies may provide important insights to answer (i) if enhanced polarization comes

from low-symmetry phases, (ii) if strain engineering can create short-range ordering above the Curie temperature of bulk crystal; and (iii) if there is any similarity between domain engineering and strain engineering.

6.2.3 Neutron scattering of Fe-Ga crystals under magnetic fields

For magnetic shape memory alloys, growth of c-axis elastic domains occurs upon application of magnetic field, which contributes to large elastic strain in addition to magnetostrictive strain. My results have indicated that there are different Ga-pairs along a- or c-axis with a lower symmetry than cubic. Competition of Ga-pairs along different crystallographic orientations is at least possible in two neighboring modified-DO_3 cells with 90^o angle. However, it is not known whether the size and orientation of Ga-pairs change during cooling down (scalar) or upon applying magnetic fields (vector). In other words, it is very interesting to see if there is field-forced ordering in Fe-Ga alloys.

Diffuse neutron scattering is a powerful method that can resolve such nanoscale inhomogeneities. I presume that comparison of the diffuse scattering patterns in different zones before and after applying magnetic fields may help to resolve these questions. Compositions near A2 and DO_3 phase boundary should be given special attention.

6.2.4 Magnetic domain structures of Fe-Ga alloys under stress

It is well known that applying compressive stress can pre-align magnetic domains, and thus increase magnetostriction during domain rotation. However, previous studies of magnetostriction as a function of the magnetization squared for three compressive stress

levels have shown a nonlinear deviation from theory predictions. Both the domain pre-alignment process under stress and domain rotation process under magnetic fields remain unresolved issues. It is generally believed that (i) pre-stress can assist the alignment of ferroelastic domains; and (ii) as the magnitude of compressive stress is increased, attainment of equivalent magnetostriction requires larger magnetic field. Both of these results will facilitate observation of domain rotation process by MFM method. Accordingly, it might be fruitful to perform MFM studies upon (i) increasing compressive stress; and (ii) applying step-increased magnetic fields perpendicular to the direction along which stress is applied.

Reference

1. Shigeyuki Sõmiya, Advanced Ceramics III, (Elesvier Applied Science, London and New York), p71
2. V. K. Wadhawan, *Introduction to Ferroic Materials*, Gordon & Breach, UK, 2000.
3. E. K. H. Salje, *Phase transitions in ferroelastic and co-elastic crystals : an introduction for mineralogists, material scientists, and physicists* (Cambridge University Press, Cambridge, 1990), p.147
4. A. J. Freeman and H. Schmid, *Magnetoelectric Interaction Phenomena in Crystals (*Gordon and Breach, London, 1975).
5. Ferroelectrics and related materials, Lines and Glass, Oxford (1977)
6. Aizu, K., J. phys. Soc. Jpn. 19, 918; 20, 959. Phys. Rev. 140, 590; 146, 423
7. H. F. Kay and P. Vousden, Philos. Mag. 40, 1019 (1949)
8. G. Skanavi and E. Matveeva, Sov. Phys. Rev. B, 50, 13168 (1957)
9. G. Smolenskii and A. Agranovskaya, Sov. Phys. Sol. State, 1, 1429 (1960)
10. V. Bokov and I. Myl'nikova, Sov. Phys. Sol. State, 3 613 (1961)
11. L. E. Cross, Ferroelectrics, 76, 241 (1987)
12. D. Viehland, s. Jang, L. cross and M. Wuttig, J. Appl. Phys. 68, 2916 (1990)
13. D. Viehland, J. Li, S. Jang, L. cross and M. Wuttig, Phys. Rev. B, 43, 8316 (1991)
14. G. Burns and F. Docal, Phys. Rev. B, 28, 2527 (1983)
15. W. Cochran, Phys. Rev. Lett. 3, 412 (1959); Adv. Phys. 9, 387 (1960); Adv. Phys. 10, 401, 1691; W. Cochran and A. Zia, Phys. Stat. Sol. 25, 273 (1968)
16. P. Anderson, G. Skanavi (Akad. Nauk. SSSR. Moscow), 290, 1959
17. G. Shirane, J. D. Axe, J. Harada, and J. P. Remeika, Phys. Rev. B 2, 155 (1970).

18. A. Naberezhnov, S. Vakhrushev, B. Dorner, and H. Moudden, Eur. Phys. J. B 11, 13 (1999).
19. P. M. Gehring, S.-E. Park, and G. Shirane, PRL 84, 5216 (2000)
20. D. Viehland, M-C. Kim, Z. Xu, and J, Li, Appl. Phys. Lett. 67 (1995), 2471
21. B. Jaffe, W. Cook and H. Jaffe, "Piezoelectric Ceramics", Academic Press, London (1971)
22. B. Jaffe, R. Rath and S. Marzullo, J. Appl. Phys. 25, 809 (1954)
23. T. Weston, A. Webster and V. McNamara, J. Can. Ceram. Soc., 36, 15 (1967)
24. S-E. Park and T. Shrout, J. Appl. Phys. 82, 1804 (1997)
25. Y. Guo, H. Luo, D. Ling, H. Xu, T. He and Z. Yin, J. Phys.: Condens. Matter 15, L77 (2003)
26. B. Noheda, D. E. Cox, G. Shirane, J. A. Gonzalo, L. E. Cross and S-E. Park, Appl. Phys. Letts., 74, 2059 (1999)
27. H. Fu and R. Cohen, Nature (London) 403, 281 (2000).
28. D. Vanderbilt and M. Cohen, Phys. Rev. B 63, 094108 (2001).
29. L. Bellaiche, A. García and D. Vanderbilt, Phys. Rev. Lett. 84, 5427–5430 (2000)
30. L. Bellaiche, A. García and D. Vanderbilt, Phys. Rev. B 64, 060103 (2001)
31. R. Guo, L.E. Cross, S-E. Park, B. Noheda, D.E. Cox, and G. Shirane, Phys. Rev. Lett. 84, 5423 (2000).
32. D. E. Cox, B. Noheda, G. Shirane, Y. Uesu, K. Fujishiro and Y. Yamada, Appl. Phys. Lett., 79, 400 (2001).
33. B. Noheda, D. E. Cox, G. Shirane, S-E. Park, L. E. Cross, and Z. Zhong, Phy. Rev. Lett. 86, 3891 (2001).

34. Z. Ye, B. Noheda, M. Dong, D. Cox, and G. Shirane, Phys. Rev. B 64, 184114 (2001).
35. J. M. Kiat, Y. Uesu, B. Dkhil, M. Matsuda, C. Malibert and G. Calvarin, Phys. Rev. B 65, 064106 (2002).
36. B. Noheda, D. E. Cox, Shirane, J. Gao and Z. Ye, Phys. Rev. B 66, 054104 (2002).
37. D. La-Orauttapong, B. Noheda, Z.-G Ye, P. M. Gehring, J. Toulouse, D. E. Cox and G. Shirane, Phys. Rev. B 65, 144101 (2002)
38. M. Wechsler, D. Lieberman and T. Read, Trans. Metall. Soc. AIME 197, 1503 (1953)
39. L. E. Tanner, Philos. Mag. 14, 111 (1966).
40. S. Shapiro, J. Larese, Y. Noda, S. Moss, and L. E. Tanner, Phys. Rev. Lett. 57, 3199 (1986).
41. S. Kartha, T. Castan, J. A. Krumhansl, and J. P. Sethna, Phys. Rev. Lett. 67, 3630 (1991).
42. A. G. Khachaturyan, S. M. Shapiro, and S. Semenovskaya, Phys. Rev. B 43, 10832 (1991).
43. D. Viehland, J. Appl. Phys. 88, 4794 (2000).
44. Y. M. Jin, Y. Wang, A. G. Khachaturyan, J. Li and D. Viehland, J. Appl. Phys. 94, 3629 (2003).
45. E. R. Leite, A. M. Scotch, A. Khan, T. Li, H. M. Chan, M. P. Harmer, S. F. Liu and S-E. Park, J. Am. Ceram. Soc., 85, 3018 (2002).
46. Stock, Ellis, Swainson, G. Xu, Hiraka, Z. Zhong, H. Luo, D. Viehland, Birgenaue and G. Shirane, submitted to Phys. Rev. B.
47. G. Engdahl, *Handbook of Giant Magnetostrictive Materials* (Academic, San Diego, 2000)

48. É. du Trémolet de Lacheisserie, *Magnetostriction theory and applications of magnetoelasticity*, (CRC Press), 1993
49. E. Tatsumoto and T. Okamoto, J. Physs Soc. Japan, 14, 1588 (1959).
50. R. C. Hall, J. Appl. Phys.30, 816 (1959); 31, 1037 (1960).
51. H. Leamy, E.D. Gibson, and F.X. Kayser, Acta Metallurgica, 1967. 15: p. 1827.
52. A. E. Clark, M. Wun-Fogle, J. B. Restorff, T. A. Lograsso, A. R. Ross, and D. L. Schlagel, Proceedings of Actuator 2000 Conference, Berlin, German
53. J. R. Cullen, A. E. Clark, M. Wun-Fogle, J. B. Restorff, T. A. Lograsso, J. Magn. Magn. Mater. 226, 948 (2001)
54. A. E. Clark, K. B. Hathaway, M. Wun-Fogle, J. B. Restorff, T. A. Lograsso and V. M. Keppens, G. Petculescu and R. A. Taylor, J. Appl. Phys. 93, 8621 (2003)
55. Z. H. Liu, G. D. Liu, M. Zhang, G. H. Wu, F. B. Meng, H. Y. Liu, Q. Yan, J. P. Qu and Y. X. Li, Appl. Phys. Lett. 85, 1751 (2004)
56. G. D. Liu, L. B. Liu, M. Zhang, J. L. Chen, J. Q. Li, G. H. Wu, Y. X. Li, J. P. Qu and T. S. Chin, Appl. Phys. Lett. 84, 2124 (2004)
57. O. Ikeda, R. Kainuma, I. Ohnuma, K. Fukamichi and K. Ishida, J. Alloys Comp. 347, 198 (2002)
58. M. Wuttig, L. Dai and J. Cullen, Appl. Phys. Lett. 80, 1135 (2002)
59. T. Lograsso, A. Ross, D. Schlagel, A.E. Clark, and M. Wun-Fogle, J. Alloys and Compounds 350, 95 (2003).
60. R. Wu, J. Appl. Phys. 91, 7358 (2002).
61. R. D. Shull, H. Okamoto, P. A. Beck, Solid State Commun. 20, 863 (1976)
62. W. Zhu and P. Han, Appl. Phys. Lett. 75, 3868 (1999).

63. W. Tan, Z. Xu, J. Shang, and P. Han, Appl. Phys. Lett. 76, 3732 (2000).

64. G. Xu, D. Viehland, J. Li, P. Gehring and G. Shirane, Phys. Rev. B 68, 212410 (2003)

65. Online materials, URL: http:// www.physics.uc.edu/ ~jph/emma/tas.html

66. Harnagea, PhD Dissertation, Martin-Luther University, Halle-Wittenberg, Germany (2001).

67. Dimension^{TM} 3100 Scanning Probe Microscope, Manual by Veeco

68. U. Hartmann, Phys. Lett. A, 137, 475 (1989)

69. C. D. Wright and E. W. Hill, Appl. Phys. Letts. 67, 433 (1995)

70. S. McVitie, R. Ferrier, J. Scott, G. S. White and A. Gallagher, J. Appl. Phys. 89, 3656 (2001)

71. A. K. Singh and D. Pandey, Phys. Rev. B 67, 064102 (2003).

72. D. Viehland and J.F. Li, J. Appl. Phys. 92, 7690 (2002).

73. Ragini, R. Ranjan, S. K. Mishra, and D. Pandey, J. Appl. Phys. 92, 3266 (2002).

74. P. M. Gehring, W. Chen, Z. –G. Ye and G. Shirane, Cond-Mat./ 0304289.

75. A. Singh and D. Pandey, Phys. Rev. B 68, 172103 (2003).

76. K. Ohwada, K. Hirota, P. Rehrig, Y. Fujii, and G. Shirane, Phys. Rev. B 67, 094111 (2003).

77. C-S Tu, C. –L. Tsai, V. H. Schimidt, H. Luo and Z. Yin, J. Appl. Phys. 89, 7908 (2001)

78. G. Xu, H. Luo, H. Xu and Z. Yin, Phys. Rev. B 64, 020102 (2001)

79. Z.-G. Ye and M. Dong, J. Appl. Phys. 87, 2312 (2000)

80. C. Tu, I. Shih, V. Schmidt, and R. Chien, Appl. Phys. Let. 83, 1833 (2003).

81. C. Randall, D. Barber, and R. Whatmore, J. Microsc. 45, 275 (1987).

82. D. Viehland, Myung-Chul Kim, Z. Xu, and Jie-Fang Li, Appl. Phys. Let. 67, 2471-2473 (1995).
83. Z. Xu, M.C. Kim, Jie-Fang Li, and Dwight Viehland, Phil. Mag. A 74, 395-406 (1996).
84. M. Abplanalp, L.M. Eng, and P. Gunter, App. Phys. A 66, S231 (1998).
85. M. Abplanalp, D. Barosova, J. Erhart, J. Fousek, P. Gunter, J. Nosek and M. Sulc, J. Appl. Phys. 91, 3797 (2002)
86. K. Bdikin, V. V. Shvartsman and A. L. Kholkin, Appl. Phys. Letts. 83, 4232 (2003)
87. F. Bai, N. Wang, J. Li, D. Viehland, G. Xu, G. Shirane and P. Gehring, J. Appl. Phys. 96, 1620 (2004)
88. J. Han and W. Cao, Phys. Rev. B, 134102 (2003)
89. G. Smolenskii, J. Phys. Soc. Jpn. 28, 26 (1970).
90. M. Glazer, presented at 10th European Meeting on Ferroelectricity, Cambridge, United Kingdom (August 2003).
91. F. Bai, J. Li and D. Viehland, Appl. Phys. Lett. 85, 2313 (2004).
92. F. Bai, J. Li, and D. Viehland, J. Appl. Phys., 97, 054103 (2005).
93. Syutkina, and E.S. Jakovleva, Phys. Status Solids 21, 465 (1967).
94. M.S. Wechsler, D.S. Lieberman, and T. A. Read, Trans. Metall. Soc., AIME 197, 1503 (1953).
95. J.C. Bowles, and J.K. Mackenzie, Acta Metall. 2, 129 (1954).
96. A.G. Khachaturyan, and G.A. Shatalov, Zh. Eksp. Teor. Fiz. 56, 1037 (1969) (Sov. Phys. JETP 29, 557 (1969)).
97. A.G. Khachaturyan, The Theory of Structural Transformations in Solids, Wiley,

1983, New York.

98. A.L. Roytburd, Fiz.Tverd.Tela 10, 3619 (1968) (Sov.Phys. Solid State 10, 2870 (1969))

99. D. Viehland and Y.-H. chen, J. Appl. Phys. 88, 6696 (2000).

100. D. Viehland and J. Powers, J. Appl. Phys. 89, 1820-1825 (2001).

101. D. Viehland, J. Powers, and J.F. Li, J. Appl. Phys. 90, 2479-2843 (2001).

102. W.J. Merz, Physical Review, 95, 690-698 (1954).

103. M.E. Drougard, J. Appl. Phys. 31, 352-355 (1960).

104. R.C. Miller and G. Weinreich, Phys. Rev. 117, 1460-1466 (1960).

105. V. Shur, E. Rumyantsev, and S. Makarov, J. Appl. Phys. 84, 445-451 (1998).

106. Y. Ishibashi and Y. Takagi, J. Phys. Soc. Japan 31, 506-511 (1971).

107. A. Levstik, M. Kosec, V. Bobnar, C. Filipic, and J. Holc, Jap. J. Appl. Phys. 36, Pt. 1, No. 5A, 2744-2746 (1997).

108. Y. Ishibashi, Integrated Ferroelectrics 2, 41 (1992).

109. T. Song, S. Aggarwal, Y. Gallais, B. Nagaraj, R. Ramesh, and J. Evans, Appl. Phys. Lett. 73, 3366-3368 (1998).

110. J. Dalton, Phys. Rev. 133A, 1034 (1964).

111. J.F. Scott, L. Kammerdiner, M. Parris, S. Traynor, V. Ottenbacher, A. Shawabkeh, and W. Oliver, J. Appl. Phys. 64, 787 (1988).

112. J.F. Scott, “Ferroelectric Memories”, Springer, Berlin (2000).

113. D. Viehland and J.F. Li, J. Appl. Phys. 90, 2995 (2001)

114. C. Jullian, J.F. Li, and D. Viehland, J. Appl. Phys. 95, 5671 (2004)

115. F. Bai, J. Li, and D. Viehland, Appl. Phys. Lett. 85, 4457 (2004)

116.Y. Imry and S. Ma, Phys. Rev. Lett. 35, 1399 (1975).

117.J. Natterman and J. Villain, Phase Transitions 11, 5 (1988).

118.D. Viehland, J. F. Li, T. A. Lograsso and M. Wuttig, Appl. Phys. Lett. 81, 3185 (2002)

119.S. Rafique, J. R. Cullen, M. Wuttig, and J. Cui, J. Apply. Phys. 95, 6939 (2004)

120.R. Tickle and R. D. James, J. Magn. Magn. Mater. 195, 627 (1999).

121.Y. Murakami, D. Shindo, K. Oikawas, R. Kainuma and K. Ishida, Appl. Phys. lett. 82, 3695 (2003)

122.Y. Murakami, D. Shindo, K. Oikawas, R. Kainuma and K. Ishida, Appl. Phys. lett. 85, 6170 (2004)

123.A. Zheludev, S. M. Shapiro, P. Wochner and L. E. Tanner, Phys. Rev. B, 54, 15045 (1996)

124.S. Guruswamy, N. Srisukhumbowornchai, A. E. Clark, J. B. Restorff, and M. Wun-Fogle, Sc. Mater. 43, 239 (2000)

125.Y. Imry and S. Ma, Phys. Rev. Lett. 35, 1399 (1975).

126.F. Bai, H. Zheng, J. Zhai1, J. Li, R. Ramesh, and D. Viehland, Appl. Phys. Letts. 85, 4109 (2004)

127.J. H. Haeni, P. Irvin, W. Chang, R. Uecker, P. Reiche, Y. L. Li,S. Choudhury, W. Tian, M. E. Hawley, B. Craigo, A. K. Tagantsev, X. Q. Pan, S. K. Streiffer, L. Q. Chen, S. W. Kirchoefer, J. Levy and D. G. Schlom, Nature, 430, 758 (2004)

128.K. J. Choi, M. Biegalski, Y. L. Li, A. Sharan, J. Schubert, R. Uecker, P. Reiche, Y. B. Chen, X. Q. Pan, V. Copalan, L.-Q. Chen, D. G. Schlom and C. B. Eom, Science, 306, 1005 (2004)

129. N. A. Pertsev, A. G. Zembilgotov, A. K. Tagantsev, Phys. Rev. Lett. 80, 1988 (1998).

130. R. A. Kellogg, A. B. Flatau, A. E. Clark, M. Wun-Fogle and T. A. Lograsso, J. Appl. Phys. 91, 7821 (2002)

VITA

Feiming Bai was born in Nei Mengu, People's Repulic of China. He graduated from Tsinghua University, Beijing, with a B.E. degree in Materials Science and Engineering in 1999 and a M.S. degree in Materials Science (metallurgy) in 2002. He entered the graduate college of Virginia Tech in the same year, focusing on the preparation and structural characterization and integration of smart materials and structures. He is a member of the American Ceramics Society, the Materials Research Society and the American Physics Society. He has authored and co-authored nearly thirty papers in the literature.